UNIVERSITE SULTAN MOULAY SLIMANE
Faculté des Sciences et Techniques
Béni-Mellal

N° d'ordre : 489/23

Centre d'Études Doctorales : Sciences et Techniques

Formation Doctorale : Mathématiques et Physiques Appliquées

THÈSE

Présentée par

YOUSSEF TIZAKAST

Pour l'obtention du grade de

DOCTEUR

Discipline : Physique

Spécialité : Mécanique - Energétique

Numerical and analytical study of double-diffusive mixed convection in lid-driven rectangular cavities filled with non-Newtonian fluids

Soutenue le Samedi 25 Février 2023 à 10h devant la commission d'examen :

Pr. Jamaa BENGOURRAM	Professeur, Faculté des Sciences et Techniques, Université Sultan Moulay Slimane, Béni Mellal, Maroc	Président
Pr. El Alami SEMMA	Professeur, Faculté des Sciences et Techniques, Université Hassan 1er, Settat, Maroc	Rapporteur
Pr. Ahmed BAHLAOUI	Professeur, Faculté Polydisciplinaire, Université Sultan Moulay Slimane, Béni Mellal, Maroc	Rapporteur
Pr. Hanaa OUAOMAR	Professeur Habilité, Faculté des Sciences et Techniques, Université Sultan Moulay Slimane, Béni Mellal, Maroc	Rapporteur
Pr. Mohamed LAMSAADI	Professeur, Faculté Polydisciplinaire, Université Sultan Moulay Slimane, Béni Mellal, Maroc	Examinateur
Pr. Mourad KADDIRI	Professeur, Faculté des Sciences et Techniques, Université Sultan Moulay Slimane, Béni Mellal, Maroc	Directeur de Thèse

Dedication

بسم الله الرحمن الرحيم

الحمد لله الذي بنعمته تتم الصالحات

I have come this far, so it is time to say thank you. Well, first things first, I thank God for his countless blessings that allowed me to overcome many obstacles and reach this point. I dedicate my thesis work to five beloved people who means the world to me. A special feeling of gratitude to my loving parents who have been a constant source of support and encouragement during the whole journey, their good examples have taught me to work hard for the things that I aspire to achieve. My brother and my sisters have never left my side and are very special. I am truly thankful for having you all in my life, thank you.

Acknowledgement

I would like to express my deepest appreciation to my teacher and thesis supervisor Pr. **Mourad Kaddiri** for his guidance and invaluable feedback throughout this project. I'm extremely thankful for having a supervisor who cared so much about my work, and who responded to my questions and queries so promptly.

I am also thankful to Pr. **Mohamed Lamsaadi** for his valuable suggestions.

Publications and communications

- Full name of the thesis author: Youssef Tizakast
- Title of the thesis: Numerical and Analytical study of double-diffusive mixed convection in lid-driven rectangular cavities filled with non-Newtonian fluids.
- Full name of the thesis director: Pr. Mourad Kaddiri.
- Laboratory: Industrial Engineering and Surface Engineering Laboratory (LGIIS), FST Beni Mellal.
- Date for beginning work on the thesis: October 2017.

Publications

[1]. Y. Tizakast, M. Kaddiri, M. Lamsaadi, T. Makayssi, and H. El Harfi. Effect of Lewis number on mixed double-diffusive convection in shallow rectangular cavities with double-lid-driven boundaries filled with non-Newtonian power-law fluids. AIP Conference Proceedings 2345, 020030 (2021).

[2]. Y. Tizakast, M. Kaddiri, M. Lamsaadi, T. Makayssi, and H. El Harfi. Effect of thermal Rayleigh number on mixed convection heat and mass transfer correlations in shallow rectangular cavities with double-lid-driven boundaries filled with non-Newtonian power-law fluids. AIP Conference Proceedings 2345, 020028 (2021).

[3]. Y. Tizakast, M. Kaddiri, M. Lamsaadi. Thermosolutal mixed convection in shallow rectangular cavity with imposed uniform heat and mass fluxes and filled with Newtonian power-law fluid. International Journal of Heat and Technology, Volume 39 (3), pp. 669-680 (2021).

[4]. Y. Tizakast, M. Kaddiri, M. Lamsaadi. Double-diffusive mixed convection in rectangular cavities filled with non-Newtonian fluids, International Journal of Mechanical Sciences, Volume 208, 106667 (2021).

[5]. Y. Tizakast, M. Kaddiri, M. Lamsaadi. Rayleigh-Bénard double-diffusive mixed convection in two-dimensional rectangular cavities filled with non-Newtonian fluids. International Journal of Mechanical Sciences, Volume 227, 107448 (2022).

[6]. H. El Harfi, M. Kaddiri, M. Lamsaadi, Y. Tizakast. Effect of a magnetic field on mixed convection in a rectangular cavity filled with ferrofluid. International Journal of Heat and Technology, Volume 39 (4), pp. 1075-1086 (2021).

[7]. Y. Tizakast, M. Kaddiri, M. Lamsaadi. Double-Diffusive Mixed Convection in a Shallow Rectangular Cavity with Double Lid-Driven Boundaries Filled with Newtonian Fluid. (Accepted for publication in AIP Conference Proceedings - 2022).

[8]. Y. Tizakast, M. Kaddiri, M. Lamsaadi. Buoyancy Ratio Effect on Double-Diffusive Mixed Convection in a Double Lid-Driven Rectangular Cavity Filled with Newtonian fluid. (Accepted for publication in AIP Conference Proceedings - 2022).

[9]. R. Nouri, M. Kaddiri, Y. Tizakast, H. Daghab. Numerical Study of Free Convection in Square Cavities Filled with Non-Newtonian Fluids and Subjected to Partial Cross Thermal Gradients. (Accepted for publication in AIP Conference Proceedings - 2022).

[10]. Y. Tizakast, M. Kaddiri, M. Lamsaadi. Shear and Buoyancy-Driven Laminar Double-Diffusive Mixed Convection in a Single Lid-Driven Rectangular Cavity. (Submitted for publication - 2022).

[11]. Y. Tizakast, M. Kaddiri, M. Lamsaadi. Double-Diffusive Natural, Mixed, and Forced Convection Characterization in a Single Lid-Driven Rectangular Cavity: Effect of Heat and Mass Diffusion Rates Difference. (Submitted for publication - 2022).

[12]. Y. Tizakast, M. Kaddiri, M. Lamsaadi. Double-Diffusive Mixed Convection inside a Rectangular Cavity driven by Opposing Buoyancy and Shear Effects. (Submitted for publication - 2022).

[13]. T. Makayssi, M. Lamsaadi M. Kaddiri, Y. Tizakast. Effect of an ascendant magnetic field on Rayleigh-Bénard convection for non-Newtonian power-law fluids in a horizontal rectangular cavity submitted to vertical temperature gradient. (Submitted to journal - 2022).

Communications

[1]. Y. Tizakast, M. Kaddiri, M. Lamsaadi, T. Makayssi, H. El Harfi. Mixed convection heat and mass transfer in square cavities with Single and double lid-driven boundaries. Workshop AMT'2019 (July 9, 2019). Casablanca, Morocco.

[2]. Y. Tizakast, M. Kaddiri, M. Lamsaadi, T. Makayssi, H. El Harfi. Effect of thermal Rayleigh number on mixed convection heat and mass transfer correlations in shallow rectangular cavities with double-lid-driven boundaries filled with non-Newtonian power-law fluids. 6th Edition of the International Congress on Thermal Sciences AMT 2020 (December 1st and 2nd, 2020). Khouribga, Morocco.

[3]. Y. Tizakast, M. Kaddiri, M. Lamsaadi, T. Makayssi, and H. El Harfi. Effect of Lewis number on mixed double-diffusive convection in shallow rectangular cavities with double-lid-driven boundaries filled with non-Newtonian power-law fluids. 6th Edition of the International Congress on Thermal Sciences AMT 2020 (December 1st and 2nd, 2020). Khouribga, Morocco.

[4]. Y. Tizakast, M. Kaddiri, M. Lamsaadi. Effect of Buoyancy Ratio on Mixed Convection Heat and Mass Transfer Correlations in Shallow Rectangular Cavities with Double Lid-Driven Boundaries Filled with Non-Newtonian Power-Law Fluids. 6th International Conference on Advances in Mechanical Engineering ICAME 2021 (October 20-22, 2021). Istanbul, Turkey.

[5]. R. Nouri, M. Kaddiri, H. Daghab, Y. Tizakast. Natural convection of non-Newtonian fluids in power law in a square cavity with a crossed temperature gradient. 1st International Conference on Applied Engineering and Natural Sciences ICAENS 2021 (November 1-3, 2021). Konya, Turkey.

[6]. Y. Tizakast, M. Kaddiri, M. Lamsaadi. Double-Diffusive Mixed Convection in a Shallow Rectangular Cavity with Double Lid-Driven Boundaries Filled with Newtonian Fluid. 7th Edition of the International Congress on Thermal Sciences AMT 2022 (March 22 and 23, 2022). Ouarzazate, Morocco.

[7]. Y. Tizakast, M. Kaddiri, M. Lamsaadi. Buoyancy Ratio Effect on Double-Diffusive Mixed Convection in a Double Lid-Driven Rectangular Cavity Filled with Newtonian fluid. 7th Edition of the International Congress on Thermal Sciences AMT 2022 (March 22 and 23, 2022). Ouarzazate, Morocco.

[8]. R. Nouri, M. Kaddiri, Y. Tizakast, H. Daghab. Numerical Study of Free Convection in Square Cavities Filled with Non-Newtonian Fluids and Subjected

to Partial Cross Thermal Gradients. 7th Edition of the International Congress on Thermal Sciences AMT 2022 (March 22 and 23, 2022). Ouarzazate, Morocco.

[9]. Y. Tizakast, M. Kaddiri, M. Lamsaadi. Double-Diffusive Mixed Convection in a Shallow Rectangular Cavity with Single Lid-Driven Boundary Filled with Newtonian Fluid. 15th Congress of Mechanics CMM 2022 (May 24-27, 2022). Casablanca, Morocco.

[10]. Y. Tizakast, M. Kaddiri, M. Lamsaadi. Double-Diffusive Mixed Convection in a Shallow Rectangular Cavity with Double Lid-Driven Boundaries Filled with Newtonian Fluid: Opposing Flow. 15th Congress of Mechanics CMM 2022 (May 24-27, 2022). Casablanca, Morocco.

[11]. Y. Tizakast, M. Kaddiri, M. Lamsaadi. Characteristics of Double-Diffusive Mixed Convection Opposing Mechanism Inside Double Lid-Driven Cavity Submitted to Heat and mass Fluxes. International Symposium on Artificial Intelligence and the Security of New Telecommunications Systems CIA2ST 2022 (June 2-3, 2022). Beni Mellal, Morocco.

[12]. Y. Tizakast, M. Kaddiri, M. Lamsaadi. Effect of Buoyancy Ratio on Natural, Mixed, and Forced Convection Fluid Flow and Heat and Mass Transport in a Single Lid-Driven Rectangular Cavity. International Symposium on Artificial Intelligence and the Security of New Telecommunications Systems CIA2ST 2022 (June 2-3, 2022). Beni Mellal, Morocco.

[13]. Y. Tizakast, M. Kaddiri, M. Lamsaadi. Analytical and Numerical Study of Natural, Mixed, and Forced Convective Heat and Mass Transfer in a Lid-Driven Rectangular Cavity Filled with Newtonian Fluid: Effect of Lewis Number. 2nd International Conference on Renewable Energy Applications and Materials ICREAM 2022 (June 22-24, 2022). Casablanca, Morocco.

[14]. Y. Tizakast, M. Kaddiri, M. Lamsaadi. Double-Diffusive Natural, Mixed, and Forced Convection Characterization in a Single Lid-Driven Rectangular Cavity: Effect of Heat and Mass Diffusion Rates Difference. 19th edition of International Thermal Days International Thermal Days JITH 2022 (November 15-17, 2022). Tangier, Morocco.

[15]. Y. Tizakast, M. Kaddiri, M. Lamsaadi. Double-Diffusive Mixed Convection inside a Rectangular Cavity driven by Opposing Buoyancy and Shear Effects. 19th edition of International Thermal Days JITH 2022 (November 15-17, 2022). Tangier, Morocco.

Abstract

The present thesis work investigates numerically and analytically double-diffusive mixed convection in closed rectangular cavities filled with non-Newtonian fluids and subjected to uniform heat and mass fluxes. The well-known finite difference and finite volume methods are used for their advantages to numerically solve the two-dimensional governing equations, while the analytical solution is developed based on the parallel flow assumption valid in the case of a shallow cavity. For shallow enclosures (aspect ratio $A >> 1$) and providing that Prandtl number $Pr \geq 10$, the problem is found to be mainly governed by: Péclet number Pe, thermal Rayleigh number Ra_T, Lewis number Le, buoyancy ratio N, and power-law behavior index n. Both solutions show a good agreement for inclusive ranges of governing parameters; thus, validating the analytical approach and the numerical codes.

To gain further insight into convection phenomena, the dominance regions of convective regimes, namely natural, mixed, and forced convection are defined, where the ratio $\frac{Ra_T}{Pe^\gamma}$, strongly correlated to index n, accurately delineates the three regimes. As a result, the effects of governing parameters are amply discussed in each governing regime in terms of the stream function, the average Nusselt number, the average Sherwood number, streamlines, isotherms, and iso-concentrations along with velocity, temperature, and concentration profiles.

Péclet and Lewis numbers are found to enhance forced regime input in overall convection, while thermal Rayleigh number and buoyancy ratio strengthens natural convective regime. Finally, the rheological behavior of non-Newtonian fluids leads to some unforeseen effects on flow characteristics directly related to the dominant convective regime and the direction of imposed heat and mass fluxes.

Keywords: Double-diffusive mixed convection, Heat and Mass transfer, Non-Newtonian fluids, Lid-driven cavities, Parallel flow, Finite difference and finite volume methods.

Résumé

Le présent travail de thèse étudie numériquement et analytiquement la convection mixte doublement diffusive dans des cavités rectangulaires confinant des fluides non-Newtoniens et soumises à des flux de chaleur et de masse uniformes. Les méthodes des différences finies et des volumes finis sont utilisées pour leurs avantages pour résoudre numériquement les équations gouvernantes, tandis que la solution analytique est développée sur la base de l'hypothèse d'écoulement parallèle valable dans le cas d'une cavité avec un rapport de forme assez large. Pour les cavités avec un rapport de forme $A >> 1$ et à condition que le nombre de Prandtl $Pr \geq 10$, le problème se trouve être régi principalement par : nombre de Péclet Pe, nombre de Rayleigh thermique Ra_T, nombre de Lewis Le, rapport des forces de volume N, et l'indice de comportement n. Les deux solutions montrent un bon accord pour des plages inclusives des paramètres directeurs ce qui valide l'approche analytique et les codes numériques.

Pour mieux comprendre les phénomènes de convection, les régions de dominance des régimes convectif, à savoir la convection naturelle, mixte, et forcée, sont définies, où le rapport $\frac{Ra_T}{Pe^{\gamma}}$, qui dépend fortement de l'indice n, délimite avec précision les trois régimes. En conséquence, les effets des paramètres directeurs sont amplement discutés dans chaque régime en termes de la fonction de courant, le nombre moyen de Nusselt, le nombre moyen de Sherwood, les lignes de courant, les isothermes, et les isoconcentrations ainsi que les profils de vitesse, de température, et de concentration.

Les nombres de Péclet et de Lewis améliorent la contribution du régime forcé dans la convection, tandis que le nombre de Rayleigh thermique et le rapport des forces de volume renforcent le régime de convection naturelle. Enfin, le comportement rhéologique des fluides non-Newtoniens conduit à des effets imprévus sur les caractéristiques d'écoulement directement liés au régime convectif dominant et à la direction des flux de chaleur et de masse imposés.

Mots-clés : Convection mixte doublement-diffusive, Transfert de chaleur et de masse, Fluides non-Newtoniens, Cavités avec parois entrainées, Écoulement parallèle, Méthodes des différences finies et des volumes finis.

ملخص

يتطرق البحث الذي بين أيدينا لدراسة الحمل المختلط (حمل طبيعي وحمل قسري في ان واحد) مزدوج الانتشار عدديًا وتحليليًا في تجاويف مستطيلة مغلقة مملوءة بالسوائل غير النيوتونية ومعرضة لفيض حراري وكتلي منتظم. لحل المعادلات الحاكمة ثنائية الأبعاد عدديًا قمنا باستخدام طريقتين واسعتي الانتشار وهما تقنية الفروقات المحدودة وتقنية الحجم المحدود، بينما يتم تطوير الحل التحليلي بناءً على فرضية الجريان المتوازي الصالحة في حالة التجاويف ذات نسبة عرض إلى الارتفاع A كبيرة بما فيه الكفاية. بالنسبة للتجاويف ذات $A >> 1$ ورقم براندتل $Pr \geq 10$، وجدنا ان المتغيرات التي تتحكم بشكل أساسي في جريان المائع وانتقال الحرارة والكتلة هي: رقم بيكليه Pe، رقم رايليه الحراري Ra_T، رقم لويس Le، نسبة قوى الطفو N، ومؤشر سلوك التدفق n. يُظهر كلا الحلين، العددي والتحليلي، اتفاقًا جيدًا ضمن نطاقات شاملة لقيم المتغيرات المتحكمة، الشيء الذي يمكن من التحقق من صحة النهج التحليلي والبرامج المعلوماتية المستخدمة في الحل العددي.

لفهم اوضح لظواهر الحمل، يتم تحديد مناطق الهيمنة للأنظمة الثلاث: الحمل الطبيعي، المختلط، والقسري، حيث النسبة $\frac{Ra_T}{Pe^{\gamma}}$ ، التي ترتبط ارتباطًا وثيقًا بالمؤشر n ، تؤطر بدقة الأنظمة الثلاثة. نتيجة لذلك، تمت مناقشة تأثيرات المتغيرات المتحكمة بإسهاب في كل من الأنظمة الثلاثة باستعمال دالة السريان، متوسط رقم نسلت، متوسط رقم شيروود، خطوط الجريان، خطوط الحرارة المتساوية، خطوط التركيز المتساوي بالإضافة إلى منحنيات توزيع السرعة، توزيع الحرارة، وتوزيع التركيز.

تظهر النتائج ان رقم بيكليه ورقم لويس يقومان بتعزيز دور الحمل القسري في جريان المائع وانتقال الحرارة والكتلة بينما رقم رايليه الحراري ونسبة قوى الطفو يعززان دور الحمل الطبيعي. أخيرًا، يؤدي السلوك الريولوجي للسوائل غير النيوتونية الى بعض النتائج غير المتوقعة على خصائص التدفق والمرتبطة مباشرة بنظام الحمل المهيمن واتجاه الفيض الحراري والكتلي المطبق.

كلمات مفتاحية : الحمل المختلط مزدوج الانتشار، انتقال الحرارة والكتلة، السوائل غير النيوتونية، التجاويف ذات السطح المتحرك، الجريان المتوازي، تقنية الفروقات المحدودة وتقنية الحجم المحدود.

Nomenclature

A	aspect ratio of the cavity, Eq. (3.26)
C_T	dimensionless temperature gradient in the x-direction
C_S	dimensionless concentration gradient in the x-direction
D	mass diffusivity $(m^2 \ / \ s)$
g	gravitational acceleration $(m^2 \ / \ s)$
Gr	Grashof number
H'	height of the enclosure (m)
j'	constant mass flux per unit area $(kg/m^2 \ s)$
k	consistency index for a power-law fluid $(Pa.s^n)$
Le	Lewis number, Eq. (3.26)
L'	length of the rectangular enclosure (m)
N	buoyancy ratio, Eq. (3.26)
n	flow behavior index for a power-law fluid
Nu_h	local horizontal Nusselt number, Eqs. (3.27), (3.29), and (3.101)
$\overline{Nu_h}$	mean horizontal Nusselt number, Eqs. (3.31) and (3.101)
Nu_v	local vertical Nusselt number, Eqs. (3.33) and (3.102)
$\overline{Nu_v}$	mean vertical Nusselt number, Eqs. (3.35) and (3.102)
Pe	Péclet number, Eq. (3.26)
Pr	generalized Prandtl number, Eq. (3.26)
q'	constant heat flux per unit area (W/m^2)
Ra_T	generalized thermal Rayleigh number, Eq. (3.26)
Re	Reynolds number
S	dimensionless concentration $[= (S' - S'_0) \ / \ \Delta S^*]$
S'_0	reference concentration (kg/m^3)
Sh_h	local horizontal Sherwood number, Eqs. (3.28), (3.30), and (3.101)
$\overline{Sh_h}$	mean horizontal Sherwood number, Eqs. (3.32) and (3.101)
Sh_v	local vertical Sherwood number, Eqs. (3.34) and (3.102)
$\overline{Sh_v}$	mean vertical Sherwood number, Eqs. (3.36) and (3.102)
T	dimensionless temperature $[= (T' - T'_0)/\Delta T^*]$

T'_0	reference temperature (K)
ΔS^*	characteristic concentration $[= j'H'/D]$ (kg/m^3)
ΔT^*	characteristic temperature $[q'H'/\lambda]$ (K)
(u, v)	dimensionless horizontal and vertical velocities $[(u', v')/(\alpha/H')]$
(x, y)	dimensionless horizontal and vertical coordinates $[= (x', y')/H']$

Greek symbols

α	fluid thermal diffusivity (m^2/s)
β_T	fluid thermal expansion coefficient $(1/K)$
β_S	fluid solutal expansion coefficient (m^3/kg)
$\bar{\bar{\dot{\gamma}}}$	rate of deformation tensor (s^{-1})
λ	fluid thermal conductivity $(W/m\ K)$
μ	Newtonian fluid dynamic viscosity $(Pa.s)$
μ_a	fluid dimensionless apparent viscosity, Eq. (3.25)
$\bar{\bar{\sigma}}$	stress tensor (Pa)
$\bar{\bar{\tau}}$	viscous stress tensor (Pa)
ρ	fluid density (kg/m^3)
Ω	dimensionless vorticity $[=\Omega'/(\alpha/H'^2)]$
ψ	dimensionless stream function $[= \psi' / \alpha]$

Superscript

$'$	dimensional variable

Subscript

c	value in center of the cavity $(x = A/2,\ y = 1/2)$
cr	critical value

Table of Contents

Introduction 1

CHAPTER 1 Literature Review 4

1.1 Introduction 4

1.2 Double-diffusive natural convection 4

1.2.1 Definition and significance 4

1.2.2 Published works 5

1.3 Non-Newtonian fluids 8

1.4 Mixed convection 9

1.4.1 Definition and importance 9

1.4.2 Published works 10

1.5 Horizontal channels 14

1.5.1 Real world applications 14

1.5.2 Published works 15

1.6 Conclusion 16

CHAPTER 2 Theoretical Framework: Rheological Model 17

2.1 Introduction 17

2.2 Rheology model 17

2.3 Constitutive equation 18

2.3.1 Newtonian fluids 19

2.3.2 Time independent non-Newtonian fluids 20

2.3.3 Power-law model 22

2.4 Conclusion 23

CHAPTER 3 Methodology 24

3.1 Introduction 24

3.2 Mathematical formulation 24

3.2.1 General governing equations 24

3.2.2 Physical configuration 25
3.2.3 Boundary conditions 26
3.2.4 Simplifying assumptions 27
3.2.5 Nondimensionalization 29
3.2.6 Heat and mass transfer 32
3.3 Numerical approach 33
3.3.1 Finite Difference Method 34
3.3.2 Finite Volume Method 36
3.4 Analytical approach 38
3.4.1 Approximate governing equations 39
3.4.2 Integration of approximate governing equations for double lid-driven cavities 39
3.4.3 Heat and mass transfer 46
3.4.4 Pure forced and pure natural convection 46
3.4.5 Single lid-driven cavities 47
CHAPTER 4 Double-Diffusive Mixed Convection in a Single Lid-Driven Cavity Filled with Newtonian Fluid 50
4.1 Introduction 50
4.2 Effect of Prandtl number 50
4.3 Numerical code validation 51
4.4 Mesh size choice 51
4.5 Value of A satisfying the large aspect ratio approximation 52
4.6 Mixed convection parameter 54
4.7 Dynamical, thermal, and solutal structures 56
4.8 Effect of Péclet number 58
4.9 Effect of thermal Rayleigh number 60
4.10 Effect of Lewis number 62

4.11 Effect of buoyancy ratio 64
4.12 Horizontal velocity, Temperature, and Concentration 64
4.13 Conclusions 67
CHAPTER 5 Double-Diffusive Mixed Convection in Double Lid- Driven Rectangular Cavities Filled with Non-Newtonian Fluids 69
5.1 Introduction 69
5.2 Numerical code validation 70
5.3 Mesh size choice 70
5.4 Value of $\boldsymbol{A}$ satisfying the large aspect ratio approximation 72
5.5 Mixed convection parameter 72
5.6 Dynamical, thermal, and solutal structures 75
5.7 Effect of Péclet number 77
5.8 Effect of thermal Rayleigh number 80
5.9 Effect of Lewis number 83
5.10 Effect of buoyancy ratio 85
5.11 Horizontal velocity, temperature, and concentration 86
5.12 Effect of power-law behavior index 88
5.13 Conclusions 89
CHAPTER 6 Rayleigh-Bénard Double-Diffusive Mixed Convection in Double Lid-Driven Rectangular Cavities Filled with Non-Newtonian Fluids 91
6.1 Introduction 91
6.2 Value of $\boldsymbol{A}$ satisfying the large aspect ratio approximation 91
6.3 Mixed convection parameter 92
6.4 Dynamical, thermal, and solutal structures 95
6.5 Effect of Péclet number 98
6.6 Effect of thermal Rayleigh number 102
6.7 Effect of Lewis number 105

6.8 Effect of buoyancy ratio 108
6.9 Horizontal velocity, temperature, and concentration..... 110
6.10 Effect of power-law behavior index 113
6.11 Critical Péclet number 114
6.12 Conclusions 115
General Conclusions 118
References 122

List of Figures

Figure 2.1. Viscosity-shear rate plot for pseudoplastic fluids at different temperatures. 21

Figure 3.1. Physical model of the investigated configuration along with coordinate system and associated boundary conditions. The cavity is subjected to uniform density of heat and mass fluxes, q' and j', respectively, with horizontal boundaries are considered either motionless or slide with uniform velocity u_0'. 26

Figure 3.2. Two-dimensional control volume for finite volume method.....37

Figure 4.1. Geometry of the investigated configuration along with coordinate system and associated boundary conditions. The vertical walls are submitted to uniform density of heat and mass fluxes, q' and j', respectively, while the horizontal ones are insulated and impermeable. The top wall slides continuously from left to right with a constant velocity u_0', while the remaining boundaries are motionless. 51

Figure 4.2. Evolution of numerical average horizontal Nusselt number ($\overline{Nu_h}$) with the cavity aspect ratio $A = \frac{L'}{H'}$ for $Ra_T = 10^5, Le = 5, N$=1, and different Pe values in a single lid-driven enclosure. 53

Figure 4.3. Natural, forced, and mixed convection dominance regions for $Le = 1$ and $N = 1$ inside a single lid-driven rectangular cavity. 55

Figure 4.4. Streamlines (top), isotherms (middle), and iso-concentrations (bottom) for $A = 24, Ra_T = 10^5, Le = 5$ and $N = 1$ while varying Péclet number to account for the different convective regimes (natural, mixed, and forced convection) inside a single lid-driven cavity. (Scale not respected). 57

Figure 4.5. Streamlines (top), isotherms (middle), and iso-concentrations (bottom) for pure natural convection at $A = 25,\ Ra_T = 10^5, Le = 5,$ and $N = 1$ inside a single lid-driven cavity. (Scale not respected). 57

Figure 4.6. Streamlines (top), isotherms (middle), and iso-concentrations (bottom) for pure forced convection ($Ra_T = 0$) at $A = 24, Le = 5, N = 1$ and different Pe values inside a single lid-driven cavity. (Scale not respected).....58

Figure 4.7. Evolutions of the stream function at the center of the cavity ($x = A/2,\ y = 1/2$) (top), horizontal Nusselt number (middle), and horizontal Sherwood number (bottom) with Péclet number (Pe) for $Le = 5, N = 1$, and different values of Ra_T inside a single lid-driven cavity. 59

Figure 4.8. Evolutions of the stream function at the center of the cavity ($x = A/2,\ y = 1/2$) (top), horizontal Nusselt number (middle), and horizontal Sherwood number (bottom) with thermal Rayleigh number (Ra_T) for $Le = 5, N = 1$, and different values of Pe inside a single lid-driven cavity.....61

Figure 4.9. Evolutions of the stream function at the center of the cavity ($x = A/2,\ y = 1/2$) (top), horizontal Nusselt number (middle), and horizontal Sherwood number (bottom) with Lewis number (Le) for $Ra_T = 10^5, N = 1$, and different values of Pe inside a single lid-driven cavity. 63

Figure 4.10. Evolutions of the stream function at the center of the cavity ($x = A/2,\ y = 1/2$) (top), horizontal Nusselt number (middle), and horizontal Sherwood number (bottom) with buoyancy ratio (N) for $Ra_T = 10^5, Le = 5$, and different values of Pe inside a single lid-driven cavity. 65

Figure 4.11. Horizontal velocity u (top), temperature T (middle), and concentration S (bottom) profiles at mid-length of the cavity ($x = A/2$) along the vertical coordinate y for $Pe = 25, Le = 5, N = 1$, and various values of Ra_T inside a single lid-driven cavity. $Ra_{T(cr)}$ signals the onset of buoyancy-driven flow. 66

Figure 5.1. Geometry of the investigated configuration along with coordinate system and associated boundary conditions. Uniform density of heat and mass fluxes q' and j', respectively, are applied to motionless vertical walls, while the horizontal ones are insulated, impermeable, and move in opposite directions with the same uniform velocity u_0'.....69

Figure 5.2. Variation of numerical horizontal Nusselt number ($\overline{\mathrm{Nu_h}}$) with the cavity aspect ratio ($A = L'/H'$) while varying Péclet number Pe to account for the different convective regimes (natural, mixed, and forced convection) for: (a) pseudoplastic fluid $n = 0.6$, (b) Newtonian fluid $n = 1.0$, and (c) dilatant fluid $n = 1.4$ at $Ra_T = 10^5, Le = 10,$ and $N = 1$ inside double lid-driven cavities. 73

Figure 5.3. The dominance regions of the three convective regimes: natural, forced, and mixed convection for different values of n at $Le = 1$ and $N = 1$ inside double lid-driven rectangular cavities. 75

Figure 5.4. Streamlines (top), isotherms (middle), and iso-concentrations (bottom) for pseudoplastic fluid $n = 0.6$ at $A = 24, Ra_T = 10^5$, $Le = 10$ and $N = 1$ while varying Péclet number Pe inside double lid-driven rectangular cavity. (Scale not respected).76

Figure 5.5. Streamlines (top), isotherms (middle), and iso-concentrations (bottom) for Newtonian fluid $n = 1.0$ at $A = 24, Ra_T = 10^5$, $Le = 10$ and $N = 1$ while varying Péclet number Pe inside double lid-driven rectangular cavity. (Scale not respected).77
Figure 5.6. Streamlines (top), isotherms (middle), and iso-concentrations (bottom) for dilatant fluid $n = 1.4$ at $A = 24, Ra_T = 10^5, Le = 10$ and $N = 1$ while varying Péclet number Pe inside double lid-driven rectangular cavity. (Scale not respected). 78
Figure 5.7. Streamlines (top), isotherms (middle), and iso-concentrations (bottom) for pure natural convection at $Ra_T = 10^5, Le = 10,$ and $N = 1$. The results are presented for different fluid behaviors: pseudoplastic $(n = 0.6)$, Newtonian $(n = 1.0)$, and dilatant $(n = 1.4)$ inside double lid-driven rectangular cavity. (Scale not respected). 79
Figure 5.8. Streamlines (top), isotherms (middle), and iso-concentrations (bottom) for pure forced convection $(Ra_T = 0)$ at $Pe = 100, Le = 10,$ and $N = 1$. The results are presented for different fluid behaviors: pseudoplastic $(n = 0.6)$, Newtonian $(n = 1.0)$, and dilatant $(n = 1.4)$ inside double lid-driven rectangular cavity. (Scale not respected). 80
Figure 5.9. Evolutions of the stream function at the center of the cavity $(x = A/2,\ y = 1/2)$ (left), horizontal Nusselt number (middle), and horizontal Sherwood number (right) with Péclet number (Pe) for $Le = 10, N = 1,$ and different values of Ra_T and n inside double lid-driven cavities. 81
Figure 5.10. Effects of governing parameters on y_0 values (defining the vertical distance between the point with maximum velocity and the sliding wall): (a) effect of Pe $(Ra_T = 10^5, Le = 10, N = 1), (b)$ effect of Ra_T $(Pe = 25, Le = 10, N = 1), (c)$ effect of Le $(Pe = 25, Ra_T = 10^5, N = 1)$, and (d) effect of N $(Pe = 25, Ra_T = 10^5, Le = 10)$ all for different values of n. 82
Figure 5.11. Evolutions of the stream function at the center of the cavity $(x = A/2,\ y = 1/2)$ (left), horizontal Nusselt number (middle), and horizontal Sherwood number (right) with thermal Rayleigh number (Ra_T) for $Le = 10, N = 1,$ and different values of Pe and n inside double lid-driven cavities. 83
Figure 5.12. Evolutions of the stream function at the center of the cavity $(x = A/2,\ y = 1/2)$ (left), horizontal Nusselt number (middle), and horizontal Sherwood number (right) with Lewis number (Le) for $Ra_T = 10^5, N = 1,$ and different values of Pe and n inside double lid-driven cavities. 84

Figure 5.13. Evolutions of the stream function at the center of the cavity ($x = A/2,\ y = 1/2$) (left), horizontal Nusselt number (middle), and horizontal Sherwood number (right) with buoyancy ratio (N) for $Ra_T = 10^5, Le = 10$, and different values of Pe and n inside double lid-driven cavities. 86
Figure 5.14. Horizontal velocity u (left), temperature T (middle), and concentration S (right) profiles at mid-length of the cavity ($x = A/2$) along the vertical coordinate y for $Pe = 25, Le = 10, N = 1$, and various characteristic values of Ra_T and n inside double lid-driven cavities. $Ra_{T(cr)}$ signals the onset of buoyancy-driven flow. 87
Figure 6.1. Physical model of the investigated configuration along with coordinate system and associated boundary conditions. The horizontal walls are subjected to uniform density of heat and mass fluxes, q' and j', respectively, and move in opposite directions with the same uniform velocity u_0', while the vertical boundaries are motionless, insulated, and impermeable. 92
Figure 6.2. Variation of numerical vertical Nusselt number ($\overline{Nu_v}$) with the cavity aspect ratio ($A = L'/H'$) while varying Péclet number Pe to account for the different convective regimes (natural, mixed, and forced convection) for: (a) pseudoplastic fluid $n = 0.6$, (b) Newtonian fluid $n = 1.0$, and (c) dilatant fluid $n = 1.4$ at $Ra_T = 10^4, Le = 10,$ and $N = 1$ inside double lid-driven Rayleigh-Bénard configuration...93
Figure 6.3. Natural, forced, and mixed convection dominance regions with pseudoplastic ($n = 0.6$), Newtonian ($n = 1.0$), and dilatant ($n = 1.4$) working fluids for $Le = 1$ and $N = 1$ inside double lid-driven Rayleigh-Bénard configuration.....94
Figure 6.4. Streamlines (top), isotherms (middle), and iso-concentrations (bottom) while varying Péclet number Pe for a pseudoplastic fluid $n = 0.6$ at $A = 28, Ra_T = 10^4$, $Le = 10$ and $N = 1$ inside double lid-driven Rayleigh-Bénard configuration. (Scale not respected). 96
Figure 6.5. Streamlines (top), isotherms (middle), and iso-concentrations (bottom) while varying Péclet number Pe for a Newtonian fluid $n = 1.0$ at $A = 28$, $Ra_T = 10^4$, $Le = 10$ and $N = 1$ inside double lid-driven Rayleigh-Bénard configuration. (Scale not respected). 97
Figure 6.6. Streamlines (top), isotherms (middle), and iso-concentrations (bottom) while varying Péclet number Pe for a dilatant fluid $n = 1.4$ at $A = 28, Ra_T = 10^4$, $Le = 10$ and $N = 1$ inside double lid-driven Rayleigh-Bénard configuration. (Scale not respected). 98

Figure 6.7. Streamlines (top), isotherms (middle), and iso-concentrations (bottom) for pure natural convection at $A = 28,\ Ra_T = 10^4, Le = 10,$ and $N = 1$. The results are illustrated for the three fluid behaviors: pseudoplastic $(n = 0.6)$, Newtonian $(n = 1.0)$, and dilatant $(n = 1.4)$ inside double lid-driven Rayleigh-Bénard configuration. (Scale not respected). 99
Figure 6.8. Streamlines (top), isotherms (middle), and iso-concentrations (bottom) for pure forced convection $(Ra_T = 0)$ at $A = 28,\ Pe = 150, Le = 10,$ and $N = 1$. The results are illustrated for the three fluid behaviors: pseudoplastic $(n = 0.6)$, Newtonian $(n = 1.0)$, and dilatant $(n = 1.4)$ inside double lid-driven Rayleigh-Bénard configuration. (Scale not respected). 100
Figure 6.9. Variations of the stream function at the center of the cavity $(x = A/2,\ y = 1/2)$ (left), vertical Nusselt number (middle), and vertical Sherwood number (right) with Péclet number Pe for $Le = 10, N = 1$, and various values of Ra_T and n inside double lid-driven Rayleigh-Bénard configuration. 101
Figure 6.10. Effects of governing parameters on y_0 values (defining the vertical distance between the point with maximum velocity and the sliding wall) considering Rayleigh-Bénard configuration: (a) effect of Pe $(Ra_T = 10^4, Le = 10, N = 1), (b)$ effect of Ra_T $(Pe = 25, Le = 10, N = 1), (c)$ effect of Le $(Pe = 25, Ra_T = 10^4, N = 1)$, and (d) effect of N $(Pe = 25, Ra_T = 10^4, Le = 10)$ all for different values of n. 103
Figure 6.11. Variations of the stream function at the center of the cavity $(x = A/2, y = 1/2)$ (left), vertical Nusselt number (middle), and vertical Sherwood number (right) with thermal Rayleigh number Ra_T for $Le = 10, N = 1$, and various values of Pe and n inside double lid-driven Rayleigh-Bénard configuration. 104
Figure 6.12. Variations of the stream function at the center of the cavity $(x = A/2, y = 1/2)$ (left), vertical Nusselt number (middle), and vertical Sherwood number (right) with Lewis number Le for $Ra_T = 10^4, N = 1$, and various values of Pe and n inside double lid-driven Rayleigh-Bénard configuration. 106
Figure 6.13. Variations of the stream function at the center of the cavity $(x = A/2, y = 1/2)$ (left), vertical Nusselt number (middle), and vertical Sherwood number (right) with buoyancy ratio N for $Ra_T = 10^4, Le = 10$, and various values of Pe and n inside double lid-driven Rayleigh-Bénard configuration. 109

Figure 6.14. Horizontal velocity u (left), temperature T (middle), and concentration S (right) profiles at mid-length of the cavity $(x = A/2)$ along the y-axis for $Pe = 25, Le = 10, N = 1$, and different characteristics values of Ra_T and n inside double lid-driven Rayleigh-Bénard configuration. $Ra_{T(cr)}$ signals the onset of buoyancy-driven flow. 111

List of Tables

Table 3.1 – Dimensionless variables. 30

Table 4.1 – Comparison of average Nusselt number with published results in the literature for a lid-driven enclosure with $Gr = 100, Pr = 0.71$, and different values of Re 52

Table 4.2 – Convergence tests using $\overline{Nu_h}$ for $A = 24,\ Ra_T = 10^5, Le = 5, N = 1$, and different values of Pe in a single lid-driven cavity. 52

Table 4.3 – Correlation coefficients η_n and η_f. 56

Table 5.1 – Comparison of relative average Nusselt number ($Nu_r = Nu_{n\#1}/Nu_{n=1}$) for $Pr^* = 100,\ Ra^* = 10^4\ and\ 10^5$ and different values of n. 70

Table 5.2 – Convergence tests for $A = 24, Ra_T = 10^5, Le = 10, N = 1, n = 0.6$, and different values of Pe in a double lid-driven cavity. 71

Table 5.3 – Convergence tests for $A = 24, Ra_T = 10^5, Le = 10, N = 1, n = 1.0$, and different values of Pe in a double lid-driven cavity. 71

Table 5.4 – Convergence tests for $A = 24, Ra_T = 10^5, Le = 10, N = 1, n = 1.4$, and different values of Pe in a double lid-driven cavity. 72

Table 5.5 – Correlation coefficients η_n and η_f for characteristic values of n. 75

Table 5.6 – $Ra_{T(cr)}$ values signaling buoyancy-driven flow onset for $Pe = 25, Le = 10, N = 1$ and different values of n inside double lid-driven cavities. 88

Table 6.1 – Correlation coefficients η_n and η_f for characteristic values of n in Rayleigh-Bénard configuration. 95

Table 6.2 – $Ra_{T(cr)}$ values signaling buoyancy-driven flow onset for $Pe = 25$, $Le = 10, N = 1$, and different values of n inside double lid-driven Rayleigh-Bénard configuration. 112

Table 6.3 – Effect of Ra_T on Pe_{cr} for $Le = 10, N = 1$, and different values of n. 114

Table 6.4 – Effect of Le on Pe_{cr} for $Ra_T = 10^4, N = 1$, and different values of n. 115

Table 6.5 – Effect of N on Pe_{cr} for $Ra_T = 10^4, Le = 10$, and different values of n. 115

Introduction

Convective fluid flows generated when only one component affects the density – for example, temperature gradient – are largely investigated and are very well understood. When the fluid density is determined by the gradients of more than one diffusing property, the intuition gained based on thermal convection (convection is generally categorized by the main effect driving fluid flow) can be misleading as an entire range of new phenomena can emerge. Double-diffusive convection occurs for fluids containing two components diffusing at different rates (the different diffusivity rates of heat and mass). In the early beginnings of the subjects around 1956, there was little indication that in couple decades the described phenomenon, and associated processes, would become a new field of fluid dynamics and play a significant role in oceanography and more recently in astrophysics, geology, and engineering applications. The parallel development in these fields outside the realm of oceanic science allowed to overcome, to some extent, the delay in the advancement of double-diffusive convection compared to many other, less critical, branches of fluid dynamics. This delay can generally be attributed to two mean reasons, the relatively small size of the oceanography community and the lack of practical motivations that usually drive the progress in fluid mechanics as in meteorology, aircraft industry, and ship hydrodynamics. These limitations are now of the past; however, many of double-diffusive convection aspects are still surrounded by confusion and controversy where the need to invest more effort in investigating all the aspects of the problem is essential to adequately understand the physics and consequences of double-diffusion.

In the present thesis work, and while natural and forced mechanisms of convection will be investigated, the focus will be on the more challenging double-diffusive mixed convection. This cross field of natural and forced convection presents more difficulties to deal with compared to pure natural or pure forced convections. Mixed convection fluid flow occurs due to combined buoyancy force (i.e., natural convection) and some external applied forces (i.e., forced convection), resulting in a large range of applications including the cooling of nuclear reactors during emergency shutdowns, heat exchangers, solar energy systems exposed to wind, and electronic components cooling. The optimal design of such systems along with the control of heat and mass transfer processes requires accurate simulation of mixed convective fluid flow and heat

and mass transfer. Therefore, and given the difficulties attached to the field, engineers still have several unanswered questions due to the lack of studies establishing a reliable theoretical background for double-diffusive mixed convection. Furthermore, fluid properties differ from one application to another as they are chosen according to the specific operating requirements of each application. Accordingly, such applications largely require the use of non-Newtonian fluids given their engineered viscosity properties which are essential to fulfill operation requirements. However, the non-linear behavior of non-Newtonian fluids adds to the complexity of the problem at hand, double-diffusive mixed convection, as the governing equations become highly coupled and non-linear explaining the small number of published papers considering this kind of fluids. All these prescribed shortcomings and motivations encourage the present work where the focus will be on: (i) developing an adequate mathematical model for non-Newtonian double-diffusive mixed convection; (ii) establishing rigorous numerical solutions; (iii) exploring the existence of analytical solution; and (iv) on these bases, outlining limits separating natural, forced, and mixed regimes and investigating fluid flow, heat and mass transfer processes, and instabilities that could occur in non-Newtonian double-diffusive mixed convection with different applied dynamical, thermal, and solutal boundary conditions. The separation of convective regimes' dominance regions is key to better understanding the different convection phenomena that emerge in the mixed regime. The boundaries splitting the regimes need to be well-defined, take into account the non-Newtonian rheological behavior, and be practical for scientific and engineering fields as to address the inconsistency encountered in the literature.

Mixed convection is generally divided into aiding flow where natural and forced convection act in the same direction and opposing flow where both natural and forced convection are in opposite directions. In this work, the aiding flow case is presented given the importance of convection intensification while the opposing case, which can be of significance for applications where suppressing fluid flow and heat and mass transfer is beneficial, is well under investigation and is not presented here.

To accomplish the aforementioned research objectives, the present work is split into six chapters. The first chapter is an inclusive literature review to see how our research questions fit within the field of fluid dynamics.

In chapter two, the rheological model adopted to characterize viscous fluids flow is described briefly while introducing non-Newtonian fluids behavior. The choice of an adequate model is of importance for this study, especially being suitable for engineering applications and allowing the establishment of an analytical solution.

In the third chapter, we begin by setting the mathematical model to simulate non-Newtonian double-diffusive mixed convection fluid flows. The governing equations are then written in the dimensionless form and presented in two different formulations to solve the problem:

- The primitive variables form.
- The Stream function-vorticity formulation.

Next, we present the numerical approach for solving the two-dimensional governing equations with two methods, the finite difference method using the stream function-vorticity formulation and the finite volume method using the primitive variables form. Finally, we establish an analytical solution based on the parallel flow approximation.

In chapters four, five, and six, the results of the two approaches, numerical and analytical, are compared for different configurations. Chapter four investigates a single lid-driven rectangular cavity filled with Newtonian fluid and submitted to uniform heat and mass fluxes along the vertical walls. Chapter five considers double lid-driven rectangular cavities filled with non-Newtonian fluids and subjected to uniform horizontal heat and mass fluxes. The sixth chapter investigates Rayleigh-Bénard double-diffusive mixed convection inside double lid-driven rectangular cavities filled with non-Newtonian fluids. For the three separate convective regimes: natural, mixed, and forced convection, the effects of governing parameters on fluid flow and heat and mass transfer are illustrated and amply discussed for each configuration in terms of stream function, average Nusselt number, average Sherwood number, streamlines, isotherms, and iso-concentrations along with velocity, temperature, and concentration profiles.

Finally, a general conclusion summarizing the key findings of the study and sets the perspectives for future works.

CHAPTER 1 Literature Review

1.1 Introduction

As the present thesis investigates double-diffusive mixed convection within rectangular cavities filled with non-Newtonian fluids and subjected to uniform heat and mass fluxes, and in order to see how our research fits within the field of thermo-fluids, an inclusive review of published literature on the topic of convective fluid flow is essential. The importance of the present work for scientific and engineering purposes is also highlighted.

1.2 Double-diffusive natural convection

1.2.1 Definition and significance

Fluid flows driven by buoyancy effect due to combined temperature and concentration gradients are widely-known as thermosolutal convection, while when their associated diffusion rates are different (Lewis number $Le \neq 1$), the flow is referred to as double-diffusive. The significance of double-diffusive flows comes from the need to understand systems with varying density due to both applied temperature and concentration gradients and given that in practice, heat and mass transfer generally occur together as seen in many industrial fields.

Solidification processes is one of the fields where both temperature and species concentration affect the liquid phase as described by Nishimura et al. [1] who discussed the appearance and evolution of double-diffusive convection during the solidification process liquid phase within enclosed cavity. Ghenai et al. [2] studied the effect of the initial concentration of a binary mixture on solidification as increasing it slowed down the process. Crystal growth is Another field where heat and mass transfer during the fluid phase has been proven to play a key role in the resulting crystal morphology and quality [3]. Singh et al. [4] carried out experiments to investigate such influence on the homogeneity of crystals grown using the Bridgman method. They found that crystals grown at larger values of thermal and solutal Rayleigh numbers showed more optical distortion. Zhou and Zebib [5] also numerically inspected crystal growth in a

rectangular enclosure subjected to horizontal temperature and concentration gradients. They showed that the onset of double-diffusive oscillatory convection in the opposing mode (Grashof number $Gr = 10^4$) decreased significantly when compared to the case of pure thermal convection. Furthermore, the applied gradients promoted the onset of oscillations and enhanced heat and mass transfer. Solar energy applications increasingly attract more attention in this renewable energy era, such systems design and thermal efficiency are directly related to heat and mass transport phenomena. Rghif et al. [6] inspected the effect of Soret and Dufour numbers on storage efficiency in a salt gradient solar pond. They reported that increasing Dufour number enhanced heat and mass transfer leading to a gain of storage (5.56%) and reducing heat losses through the pond free surface (8.53%), while the Soret number had less significant role. Saleem et al. [7] numerically investigated natural double-diffusive convection in a trapezoidal solar distiller using the finite volume method. The study showed a significant heat and mass transfer enhancement while increasing Rayleigh number ($10^4 \leq Ra \leq 10^6$), buoyancy ratio ($N = 1, 2,5$ and 10), and free stream Reynolds number ($10^2 \leq Re_\infty \leq 10^5$). Similarly, the design of thermally comfortable closed spaces requires controlling heat and mass transport processes within such spaces. Arellano et al. [8] investigated double-diffusive convection within a ventilated cavity. They found that in order to compile with temperature and contaminant concentrations regulations and attain best performance, mixed convection with Reynolds number $Re = 10^4$ is required. Double-diffusive convection importance manifests in many other applications: food processing [9], oceanography [10], dynamics of lakes [11], storage reservoirs [12], etc.

1.2.2 Published works

Given the applied thermal and solutal boundary conditions, two cases arise:

- Cavities submitted to horizontal temperature and concentration gradients along the vertical walls.
- Cavities where the horizontal walls are differentially-heated and salted and the sufficiently distanced vertical ones are considered adiabatic. This configuration is also known as ‘‘Rayleigh–Bénard’’ convection.

For the sake of simplicity, the first case will be referred to as “double-diffusive convection” and the second case as “Rayleigh–Bénard double-diffusive convection”.

1.2.2.1 Double-diffusive natural convection

Double-diffusive natural convection is by far one of the most studied subjects in thermo-fluids. Ostrach [13] conducted a review of the phenomenon. Arani et al. [14] studied numerically double-diffusive natural convection in a square enclosure with active vertical walls while the horizontal ones are insulated. They showed that the lowest heat and mass transfer occur in the case of pure thermal convection (buoyancy ratio of zero). Furthermore, increasing Rayleigh number or the buoyancy ratio led to the same result of enhancing average Nusselt and Sherwood numbers. Aly et al. [15] investigated the same phenomenon, but this time in a rectangular enclosure. Similar results to [14] were found, where the convection in double diffusive mode was higher compared to the mono-diffusive one for both nanofluid and regular fluid. They also showed that increasing Soret number while decreasing Dufour number increased heat transfer while decreasing mass transfer. Ranganathan and Viskanta [16] investigated analytically and numerically natural convection in a two-dimensional square cavity filled with a binary gas due to combined temperature and concentration gradients. They identified and applied a concentration parameter to binary gases. For buoyancy ratio $N = 1$, the temperature and concentration distributions as well as the heat and mass transfer rates were found to depend strongly on the concentration parameter for values smaller than 1. The velocities at vertical walls were inversely proportional to the said parameter. Trevisan and Bejan [17] also investigated numerically and analytically the same phenomenon of natural convection in a rectangular enclosure with uniform heat and mass fluxes applied along the vertical walls. Esfahani and Bordbar [18] performed a numerical study of laminar thermosolutal convection inside a square cavity filled with nanofluid. The finite volume SIMPLE algorithm was used to solve the dimensionless form of the governing equations. The results showed that for a constant value of Rayleigh number, increasing Lewis number improved mass transfer but reduced heat transfer. Hussain et al. [19] numerically investigated double-diffusive nanofluid flow in a duct with cavity heated from bottom side using the Galerkin finite element method to solve the governing equations. It was observed that while increasing Reynolds number, a circulating cell is formed inside the cavity and convection domination

enhanced. Furthermore, they concluded similar conclusions as the previously mentioned references where increasing buoyancy ratio or Lewis number resulted in stronger convection. Darbhasayanam and Barman [20] numerically investigated double-diffusive convection in a porous layer saturated by a viscous fluid, but the focus this time was on the inception of the convection regime. They reported the effect of Rayleigh number and Lewis number along with gravity variation parameter, Soret parameter, and viscous dissipation on the onset of convection. Liang et al. [21] investigated numerical results of double-diffusive convection in a slim rectangular enclosure with horizontal temperature and concentration gradients. They found that with the buoyancy ratio N increasing from 1 to 2, the flow of transition is a complex series of changes from the periodic to quasi-periodic, chaotic, periodic, and finally to laminar with dominating concentration. Recently, Hu et al. [22] inspected the effects of both cavity inclination and magnetic field on double-diffusive convection. They found that for vertical and inclined enclosures, increasing thermal Rayleigh number and buoyancy ratio resulted in the enhancement of overall heat and moisture transfer rates. As for the magnetic field, they showed that its presence caused the suppressing of the convection currents; hence, reduced heat and moisture transfer.

1.2.2.2 Rayleigh–Bénard double-diffusive natural convection

Despite the importance of double-diffusive convection discussed above, the literature review reveals fewer investigations compared to pure thermal convection (mono-diffusive convection), such observation becomes even more noticeable for Rayleigh-Bénard convection. Zhang et al. [23] numerically studied double-diffusive Rayleigh-Bénard convection in cylindrical cavities for governing parameters: Prandtl number fixed at 13.2, aspect ratio varied from 0.5 to 4, and buoyancy ratio N between -1 to 2. The study showed that both aspect ratio and buoyancy ratio influence the critical Rayleigh number characterizing the convection onset. For aiding buoyancy convection ($N > 0$), the concentration gradient accelerated flow destabilization with the critical Rayleigh number decreasing as N increased. For opposing mode ($N < 0$), the opposite occurred as the gradient promoted the fluid steady-state with the critical Rayleigh number increasing as the absolute value of N increased. Furthermore, the study compared the bifurcation sequences and flow patterns formation between thermally driven case ($N = 0$) and double-diffusive aiding and opposing cases. Rana and Chand

[24] studied double-diffusive convection in an infinite horizontal porous medium layer of couple-stress nanofluid heated and salted from below using Darcy model. The study showed that couple-stress parameter, Soret and Dufour numbers, thermo-nanofluid Lewis number, and thermo-solutal Lewis number stabilized stationary convection, while the system became steadier for equal Soret and Dufour numbers. Li et al. [25] conducted three-dimensional numerical simulations to investigate double-diffusive Rayleigh–Bénard convection in a vertical cylindrical cavity heated from the bottom and cooled at the top. The cavity was filled with a Newtonian binary mixture with initial mass fraction of 10% and Prandtl and Lewis numbers were fixed at 13.2 and 140.2, respectively. The authors reported that the initial condition used to perform simulations strongly affects the flow pattern formation. As for average Nusselt number, it increased with Rayleigh number while the flow pattern had a minor influence. Besides, compared to pure thermal case ($N = 0$), the cooperative buoyancy case ($N > 0$) enhanced flow intensity and heat transfer while the opposing case ($N < 0$) reduced them. Malashetty et al. [26] investigated convection onset in a horizontal rotating porous layer saturated with a couple-stress fluid with imposed temperatures and concentrations on the bottom and top boundaries. The results showed that Lewis number played a stabilizing role in stationary and finite amplitude modes while a destabilizing effect is observed in oscillatory mode. Further, Lewis number was found to reduce heat transfer and enhance mass transfer while increasing solute Rayleigh number strengthened both.

1.3 Non-Newtonian fluids

Non-Newtonian fluids flow is also another area of fluid dynamics suffering a shortage of investigations, despite recognizing that non-Newtonian fluids behavior is essential to fulfill operational requirements and maximize production efficiency in most engineering applications. This lack of dedicated investigations is mostly attributed to the high non-linearity and modeling complexity of such fluids. In food industries, understanding non-Newtonian fluids is critical for handling foods and beverages behavior under processing conditions in order to maintain strict product properties and to ensure the cleanness of equipment such as pipes for efficient food transport. In this context, Krishnan and Aravamudan [27] studied the use of non-Newtonian fluids to sterilize food particles suspended in holding pipe for controlling parameters: power-law index ($n = 0.57, 0.76$ and 0.94), blockage ratio: ratio of particle diameter to pipe

diameter ($BR = 0.02$ and 0.4), and particle Reynolds number ($\mathrm{Re_p} = 0.1, 1,$ and 40). They found that hydrodynamics and heat transfer on the fluid particle surface are greatly influenced by the variations in n value. They also reported that under specific conditions (low $\mathrm{Re_p}$, intermediate n, and high BR), local variations in heat transfer around the particle can lead to non-uniform heating of the particle, which can damage the nutritional values and cause non-uniform sterilization within the same food particle. Cooling problems is another field of interest for non-linear behavior of non-Newtonian fluids. Khani et al. [28] focused on the efficiency of turbines cooling system in order for disks to endure higher temperatures as increasing the gas temperature entering a turbine enhances the thermal efficiency of the engine. The authors considered non-Newtonian fluids with $n = 0, 2, 4$ and 8 and concluded that viscoelastic fluids show the highest heat transfer rate while reducing the drag. Medical research especially related to blood flow is also an active area of investigations given the non-Newtonian proprieties of blood. Sriram et al. [29] inspected the influence of non-Newtonian blood properties on the micro vessels wall shear stress measurements and proposed a two-layer non-Newtonian model to predict blood flow characteristics. Foong et al. [30] focused on biomedical drug engineering. Numerical simulations of blood circulation inside the artery showed a change from non-Newtonian to Newtonian behavior in blood flow properties due to medical treatment through body vessels, which can lead to health problems due to the change in body temperature. Therefore, authors suggested the use of mechanical engineering to design safer drugs for human blood. The same goes for drag reduction problems, where reducing friction and strengthening the lift of a body submerged in a non-Newtonian fluid is a key research question for many engineering fields. Akçay et al [31] studied drag reduction by fluid injection on a moving wall for different non-Newtonian fluids ($n = 0.01, 0.5, 1.0, 1.5,$ and 2). They reported that except for $n = 0.01$ where the reduction was insignificant, the wall mass injection reduced drag for all considered power-law indexes.

1.4 Mixed convection

1.4.1 Definition and importance

Double-diffusive mixed convection occurs due to combined buoyancy force, driven by temperature and concentration gradients, and some external forces applied to the cavity.

Recently, researchers focused mostly on lid-driven cavities system with applied shear force due to the walls' movement. The growing attention arises from the configuration wide range of scientific and engineering applications. In the scientific field, the lid-driven cavity is widely-used for studying fundamental aspects of incompressible flows within confined volumes and serves as a benchmark for validating numerical methods [32, 33]. As for engineering sector, the lid- driven cavity is found in many applications including indoor ventilation, electronic components cooling, solar ponds, nuclear reactors, heat exchangers, contaminant transport, lakes and reservoirs, and crystal growth [34-35].

1.4.2 Published works

1.4.2.1 Mono-diffusive mixed convection

The vast share of conducted Mixed convection studies cover flow and heat transfer considering different combinations of imposed temperature gradient and cavity configurations [36–42]. Munshi et al. [43] examined mixed convection in a square lid-driven cavity with internal elliptic body and constant heat flux on the bottom wall. They concluded that the mixed convection is governed by the dimensionless parameters: Richardson number (Ri), Grashof number (Gr), and Reynolds number (Re). Aydm [44] numerically investigated laminar mixed convection in a square cavity with left wall moving from bottom to top at a constant velocity. The mixed convection parameter Gr/Re^2 was used to delineate the natural, forced, and mixed heat transport regimes. The mixed regime range of Gr/Re^2 for the opposing-buoyancy case was found to be broader than that of the aiding-buoyancy case. Lamarti et al. [45] investigated thermal characteristics of a Newtonian fluid in a square cavity driven by a periodically oscillating lid. The results showed that Reynolds and Grashof numbers have an effect on energy transport and drag force depending on the velocity cycle. Also, the variation of Rayleigh number affected heat transfer on convective structures. Cheng [46] studied numerically mixed convection in a two-dimensional square cavity with adiabatic vertical walls, while the top moving-wall and bottom wall were maintained isothermally with higher temperature on the bottom. The goal was to explore how the heat transfer will be influenced when increasing simultaneously Grashof and Reynolds numbers. Additionally, a validation of the Nusselt number (Nu) correlations from the

literature was given. Gangawane and Manikandan [47] analyzed numerically laminar mixed convection in a square enclosure filled with Newtonian fluid with top wall moving from left to right, while a centered triangular block was maintained either at constant wall temperature or constant heat flux. The dependence of Nusselt number on governing parameters: Reynolds, Prandtl, and Grashof numbers was elaborated and presented for design purposes. Oztop et al. [48] considered laminar mixed convection flow in the presence of uniform magnetic field inside a square enclosure with top lid-driven heated by a corner heater. They found that the dimensions of the heater strongly altered the dominance of the natural convective regime. While the magnetic field governed heat transfer and fluid flow as increasing the Hartmann number (the magnetic parameter) decreased heat transfer, with higher reduction rate for high values of the Grashof number. Nosonov and Sheremet [49] studied mixed convection due to the effect of a local heater in a rectangular cavity. They reported that increasing Richardson number strengthened the convection inside the cavity while deforming the forced flow owing to the rise of buoyancy force magnitude. Bozorg and Siavashi [50] studied mixed convection in a square cavity containing non-Newtonian nanofluid. The results showed that shear-thinning or shear-thickening behavior fluid can noticeably change the effect of forced convection on the heat transfer efficiency. Gangawane and Oztop [51] numerically studied flow and heat transfer characteristics due to combined natural and forced convection inside semi-oval, top lid-driven cavity filled with non-Newtonian fluid. They found that the power-law index has a significant effect on flow characteristics at low Richardson number. Siddiqui et al. [52] conducted numerical simulations of mixed convection thermal transfer within a lid-driven square geometry. They concluded that a larger Grashof number enhances the stability of streamline circulations, whereas the enhancement in Reynolds number produced the opposite effect. Zhou et al. [53] numerically investigated mixed convection in a double lid-driven cubic enclosure. The results showed that Reynolds and Richardson numbers have great effects on both velocity profiles and Nusselt number. Gangawane and Gupta [54] examined thermal characteristics due to combined free and forced convection in a rectangular enclosure with one of the vertical walls moving. They found that the direction of the moving lid affects strongly the heat transfer characteristics. Mukherjee et al. [55] inspected the effect of viscous dissipation on power-law fluids forced convection through microchannels of different geometries. The trading between

fluid rheology and viscous dissipation effect has given rise to significant variation in the net convective transport. Manchanda and Gangawane [56] numerically studied laminar 2-D mixed convection inside a double lid-driven square cavity with a decentered heated triangular block for non- Newtonian power-law fluids. The governing equations were solved using finite volume approach and SIMPLE algorithm. The results showed that for a power-law index $n = 0.2$, mixed convection parameter had a negligible impact on fluid and thermal structures inside the cavity, while for $n \geq 0.6$, streamline profiles were observed to be inclined along the right side given the forced convection effect generated by top and bottom walls.

1.4.2.2 Double-diffusive mixed convection

Most of the published researches on double-diffusive mixed convection investigated square cavities filled with Newtonian fluids. Arani et al. [57] numerically investigated double-diffusive mixed convection of Newtonian nanofluid confined in a single lid-driven square cavity with differentially heated and salted vertical walls using finite volume method. The results showed that decreasing Richardson number Ri enhanced both heat and mass transfer rates, while for the same absolute value of buoyancy ratio, Nusselt and Sherwood numbers in the case of cooperating thermal and mass buoyancy forces were higher compared to the opposing case. For dominating forced convection regime at low Richardson numbers, authors reported that heat-lines structure became similar to that of streamlines, while mass-lines were always similar to streamlines due to important mass transfer rate caused by high Lewis number. As for fluid nature effect, the nanofluid enhanced heat transfer compared to pure fluid. Nithyadevi and Rajarathinam [58] investigated the problem in a double-lid driven cavity filled with nanofluid and subjected to constant temperatures and concentrations at the vertical walls while taking into account Soret and Dufour effects. Similar to [57], introducing nanoparticles to pure fluid enhanced heat and mass transfer which authors attributed to better thermal conductivity of nanofluids; whereas Dufour number strengthened heat transfer and Soret number enhanced mass transfer. Nath and Krishnan [59] numerically studied the same phenomenon within a Newtonian nanofluid filled backward facing channel. While the study also concluded that increasing nanoparticles volume fraction enhances heat transfer rate independently of the buoyancy ratio, conflicting conclusions were made for mass transfer, where introducing nanoparticles slowed down mass

transport due to mass diffusion coefficient decreasing as nanoparticles volume fraction increased. Such effect strengthened for negative buoyancy ratios compared to positive ratios given the retarding role of solutal gradient. Sivasankaran et al. [60] numerically investigated sinusoidal thermal boundary conditions influence on double-diffusive mixed convection characteristics inside a square lid-driven enclosure with vertical walls kept at a constant concentration. The authors found that for all considered values of Ri, both phase deviation and amplitude ratio affected heat and mass transfer. Further, the amplitude of wall temperature enhanced heat transfer while having small effect on mass transfer. Sheremet and Pop [61] investigated the phenomenon in a square cavity with sliding horizontal walls kept at constant temperatures and nanoparticle volume fractions. Two cases for dynamic boundary conditions were considered, where moving walls either slide in the same direction or in opposite directions. The study confirmed the established strong effect of Lewis number Le on strengthening mass transfer while heat transfer slightly enhanced. However, Nusselt number was found to decrease with Le when walls slided in opposite directions while increasing buoyancy ratio noticeably affected temperature and concentration fields for the opposing case only. Ababaei et al. [62] considered a right-angled trapezoidal enclosure partially heated and salted from the bottom and occupied with a Newtonian fluid to numerically investigate entropy generation. They found that for negative buoyancy ratios, heat and mass transfer rates and entropy generation enhanced for top wall sliding to the left compared to sliding to the right, while the opposite occurred for positive buoyancy ratios. Moreover, the three characteristics increased as the heat source approached the cold wall. Al-Amiri et al. [63], Kumar et al. [64], and Hussain et al. [65] also investigated double-diffusive mixed convection numerically in square cavities filled with Newtonian fluids and subjected to different thermal, solutal, and dynamical boundary conditions.

1.4.2.3 Non-Newtonian double-diffusive mixed convection

This attention given to double-diffusive mixed convection falls short when it comes to including the non-linear behavior of non-Newtonian fluids. Yapicia et al. [66] considered steady laminar flow inside a lid-driven cavity to study Reynolds number effect for a viscoelastic fluid with and without inertia effect. They found that Reynolds number affects largely the stress fields at the upper section of the cavity. Kefayati [67] numerically inspected the effect of horizontal magnetic field in a double lid-driven

square enclosure filled with shear thinning fluids using finite difference lattice Boltzmann method for governing parameters: Richardson number, Hartmann number, Lewis number, buoyancy ratio, and power-law index while fixing thermal Grashof number at $Gr_T = 100$. The author reported that for $Ri = 0.0062$ and $Ri = 0.01$, increasing n from 0.2 to 1.0 enhanced heat and mass transfer, while for $Ri = 1$ an opposite trend is observed. As for Hartmann number, increasing it reduced heat and mass transfer rates and significantly weakened the influence of n on transport processes. Hajesfandiari et al. [68] studied two-dimensional flow in a square single lid-driven cavity using couple stress theory to investigate non-Newtonian size-dependent flows while varying size-dependent parameter and Reynolds number. The prescribed additional boundary conditions for couple stress theory significantly influenced flow structure and critical Reynolds number after which a non-stationary flow behavior occurs. Kefayati [69] investigated laminar convection in a single lid-driven square cavity filled with shear thinning fluid and subjected to sinusoidal temperature and concentration boundary conditions along the right wall while keeping the left wall at high temperature and concentration. The study found that while increasing Le enhanced mass transfer, it also changed the effect of n on mass transfer for various Ri values. Nayak et al. [70] numerically investigated mixed convection within square enclosures confining pseudoplastic power-law fluids with partially heated and salted horizontal walls while the vertical ones slide in opposite directions. The results revealed that the position and the length of the active zones greatly affect fluid flow and heat and mass transfer; further, increasing Ri decreased heat and mass transfer. Kefayati [71] reported similar result as increasing Ri reduced heat and mass transfer for different values of governing parameters. This time considering active vertical walls where the left and right walls were kept at high and low temperature and concentration, respectively, while the adiabatic and impermeable horizontal walls slide in the same direction from left to right.

1.5 Horizontal channels

1.5.1 Real world applications

The significance of horizontal channels comes from the wide range of micro and macro engineering applications where such configurations are found including turbines'

components internal cooling, heat exchangers, and electronic components cooling [72, 73]. The progress in circuit integration and the ever-rising miniaturization trend in manufacturing lead to highly sophisticated components requiring highly controlled environment to operate. Consequently, detailed investigation of fluid circulation and heat and mass transfer inside rectangular cavities becomes indispensable to fulfil the operating conditions of the aforementioned systems, especially the strict cooling requirements in order to extend their life cycle while maintaining the highest performance. Enhancing heat and mass transport processes have been the main research focus being the key to efficient compact systems where various intensification methods can be considered: working fluid nature, external forces, and boundary conditions. The present study investigates the effects of all these factors on fluid flow and heat and mass transfer. First, for non-Newtonian fluids, and given what we mentioned above about their importance in engineering fields, investigating the effect of fluids' rheological behavior on heat and mass transfer is key. Second, and while exploiting natural convection is an attractive idea, the driving buoyancy force is responsible for flow instabilities going from steady laminar to turbulent flows. Thus, enhancing natural convection is a restricted solution, where introducing forced convection usually becomes essential to achieve system requirements. The results of the present study can be useful for other applications for a couple of reasons. One is the inclusive range of considered governing parameters ($Pe \leq 10^3, Ra_T \leq 10^7, 10^{-5} \leq Le \leq 10^5$, $10^{-5} \leq N \leq 10^5$, and $0.6 \leq n \leq 1.4$) allowing to cover different convective regimes (natural, mixed, and forced convection). Two, when it comes to enhancing heat and mass transfer, the obtained answers in one field can be applied to other fields giving that the main questions are the same; hence, many components that can be modeled as rectangular cavities can be considered. One of the many examples is the storage units for renewable energy systems, where simulating fluid flow and understanding temperature and concentration distributions are key for optimal design as strengthening heat and mass transport processes cut heat losses and allows gain of storage capacity [6].

1.5.2 Published works

The literature review revealed an even serious lack of investigations when it comes to double-diffusive mixed convection inside rectangular cavities. Bettaibi et al. [74]

numerically studied the phenomenon in a rectangular cavity with top lid-driven using lattice Boltzmann method to compute fluid flow and finite difference method to compute temperature and concentration fields. The authors discussed the accuracy of the proposed model to simulate mixed convection heat and mass transfer in driven cavities. Teamah and El-Maghlany [75] investigated steady laminar mixed convection in a rectangular enclosure due to combined thermal and solutal buoyancy forces. Two cases were considered, where the top wall slides from left to right (assisting flow) or in the opposite direction (opposing flow), while the motionless vertical walls maintained at different constant temperatures and concentrations. As expected, higher heat and mass transfer were reported for assisting flow compared to opposing flow; while for both cases, decreasing Ri enhanced heat and mass transfer rates.

1.6 Conclusion

All things considered, the shortage of works investigating non-Newtonian double-diffusive mixed convection within lid-driven horizontal channels becomes obvious, despite what we mentioned about the significance of each of the four research axes: double-diffusive convection, non-Newtonian fluids, lid-driven cavities, and horizontal channels for both scientific and engineering fields. Furthermore, the literature review shows that double-diffusive mixed convection inside rectangular lid-driven cavities subjected to uniform heat and mass fluxes and filled with non-Newtonian fluids has not been studied thus far.

To address this gap and taking into account the singularity and complexity of imposed boundary conditions and non-Newtonian fluids rheological behavior, the present study can lead to new findings about non-Newtonian fluids flow and heat and mass transport given all the considered driving factors.

CHAPTER 2 Theoretical Framework: Rheological Model

2.1 Introduction

Chemistry Professor Eugene Bingham invented the term rheology while working on some new materials showing strange flow behavior such as paints. Rheology, which can be applied to all materials from gases to solids, refers to flow and deformation of matter theory that characterizes the interrelation between force, deformation, and time. For the case of fluids flow, many working conditions can influence the rheological behavior; specifically: type of loading, degree of loading, duration of loading, temperature, concentration, and magnetic field for magnetorheological fluids (MRF). Fluids differ from solids as they continuously deform under an applied stress, while solids deform and stop giving their elastic response that enable them to resist such stress.

2.2 Rheology model

The main question is how to model the different fluid behaviors. Flow models are mathematical equations that can describe rheological data such as shear stress-shear rate curves ($\sigma - \dot{\gamma}$) in a fitting and concise form with few model parameters. The rheological models can be separated into three groups based on their background:

1. Empirical model: straightforward fitting of the experimental data. Power-law model, discussed later, is an example of empirical models.
2. Theoretical model: deduced from fundamental concepts in statistical mechanics, such as the extension of kinetic theory application to the liquid state, which can help understand the role of structure. An example of theoretical models is the Krieger-Dougherty model for relative viscosity.
3. Structural model: deduced from considering the structure and kinetics of changes in it. Such structure-based analysis, along with experimental data, can be used to characterize the rheological behavior and can offer crucial understanding of a dispersed system structure role. Cross model is an example

of structural models used to describe the flow behavior of polymer dispersions and other shear-thinning fluids.

Many rheological models have been reported in the literature, with varying form and complexity, to model fluids' behaviors. The said models have been also successfully used to derive velocity profiles and flow rates in tube and channel fluid flows, along with the study of heat and mass transfer phenomena.

2.3 Constitutive equation

For viscous fluids, a simple model of a liquid can be obtained by assuming that the stress tensor $\bar{\bar{\sigma}}$ depends exclusively on the current value of the rate of deformation tensor $\dot{\bar{\bar{\gamma}}}$.

$$\bar{\bar{\sigma}} = f\left(\overline{\overline{A_1}}\right);\ \overline{\overline{A_1}} = 2\dot{\bar{\bar{\gamma}}} \tag{2.1}$$

where $\overline{\overline{A_1}}$ is the first Rivlin-Ericksen kinematic tensor.

A proposed constitutive equation needs to fulfil a set of principles before being considered admissible. One of the main principles restricting the form of the constitutive equation is 'material frame-indifference' principle, also called 'principle of objectivity', which states that a valid constitutive equation should be independent of the frame of reference or the motion of the observer. The material frame-indifference imposes that $\bar{\bar{\sigma}}$ be an isotropic tensor function (tensor components remain invariant for all rotated coordinate systems); thus, it can be expressed as follows ([76], p. 233):

$$\bar{\bar{\sigma}}\left(\overline{\overline{A_1}}\right) = \varphi_0\bar{\bar{I}} + \varphi_1\overline{\overline{A_1}} + \varphi_2\overline{\overline{A_1}}^2 \tag{2.2}$$

where the scalar functions $\varphi_0, \varphi_1,$ and φ_2 depend on the principal invariants of $\overline{\overline{A_1}}$ given by:

$$i_1\left(\overline{\overline{A_1}}\right) = tr\left(\overline{\overline{A_1}}\right);\ i_2\left(\overline{\overline{A_1}}\right) = -\frac{1}{2}tr\left(\overline{\overline{A_1}}^2\right);\ i_3\left(\overline{\overline{A_1}}\right) = \frac{1}{3}tr\left(\overline{\overline{A_1}}^3\right) \tag{2.3}$$

The symbol $tr(.)$ designates the trace of the tensor.

For an incompressible fluid, i.e., $i_1\left(\overline{\overline{A_1}}\right) = tr\left(\overline{\overline{A_1}}\right) = 0$. Equation (2.2) can be rewritten as follows:

$$\bar{\bar{\sigma}} = -p\bar{\bar{I}} + \bar{\bar{\tau}} \tag{2.4}$$

with $\bar{\bar{\tau}}$ is the viscous stress tensor:

$$\bar{\bar{\tau}} = \varphi_1 \overline{\overline{A_1}} + \varphi_2 \overline{\overline{A_1}}^2 \tag{2.5}$$

for which φ_1 and φ_2 depend only on the invariants i_2 and i_3:

$$\varphi_1 = \varphi_1(i_2, i_3) \tag{2.6}$$

$$\varphi_2 = \varphi_2(i_2, i_3) \tag{2.7}$$

On the one hand, the constitutive equation (2.4) represents a general viscous model and describes Reiner-Rivlin fluids (RR). On the other hand, a constitutive equation is thermodynamically valid if it satisfies the 'Clausius–Duhem inequality', also called 'dissipation inequality', stating that in a real material, the dissipation should be non-negative. As a result, the dissipation inequality imposes the following condition:

$$\varphi_1 tr\left(\overline{\overline{A_1}}^2\right) + \varphi_2 tr\left(\overline{\overline{A_1}}^3\right) \geq 0 \tag{2.8}$$

The viscous stress tensor expression connecting viscous stresses and strain rates $\left(\bar{\bar{\tau}} = f\left(\bar{\bar{\dot{\gamma}}}\right)\right)$ define a fluid rheological behavior law. Based on such flow behavior, fluids are generally divided into three main groups:

- Newtonian fluids
- Time independent non-Newtonian fluids
- Time dependent non-Newtonian fluids

The present work focuses on the first two groups.

2.3.1 Newtonian fluids

Fluids obeying the Newton's linear law of viscosity (fluids whose viscous stresses at each point are linearly correlated to the strain rate at that point) are called Newtonian fluids. Gases and some of the common liquids such as water, oils, and hydrocarbons display Newtonian flow characteristics, i.e., at constant temperature and pressure. Accordingly, for Newtonian fluids, Eq. (2.5) reduces to:

$$\bar{\bar{\tau}} = \varphi_1 \overline{\overline{A_1}} = 2\varphi_1 \bar{\bar{\dot{\gamma}}} = 2\mu_a' \bar{\bar{\dot{\gamma}}} \tag{2.9}$$

As Eq. (2.9) shows, the Newtonian fluid is a special case of the Reiner-Rivlin fluids with $\varphi_1 = \mu_a'$, the apparent viscosity constant for a Newtonian fluid, and $\varphi_2 = 0$. The scalar function φ_2 is generally discarded as the term containing it generates normal

stresses that doesn't qualitatively agree with experimental observations in the case of simple shearing flows.

For simple shear flows, Eq. (2.9) becomes:

$$\tau = \mu_a' \dot{\gamma} \tag{2.10}$$

with τ and $\dot{\gamma}$ are shear stress and shear rate, respectively.

2.3.2 Time independent non-Newtonian fluids

In a non-Newtonian fluid, the relation between shear stress and shear rate is not linear, where the viscosity is a variable and not a constant scalar. Such fluids are frequently encountered in industrial applications where the fluids viscosity can change by a factor of 10, 100, and in some cases even 1000. Thus, engineers cannot ignore such enormous change, leading to a modification of Newton's law where the viscosity is allowed to vary. Among the non-Newtonian fluids, the time independent non-Newtonian fluids (known also as generalized Newtonian fluids) are the most popular where the viscosity is a function of the shear rate:

$$\bar{\bar{\tau}} = 2\mu_a'(\dot{\gamma})\bar{\bar{\dot{\gamma}}} \tag{2.11}$$

For simple shear flows

$$\tau = \mu_a'(\dot{\gamma})\dot{\gamma} \tag{2.12}$$

The time independent non-Newtonian fluids can be separated into two main categories: fluids exhibiting a yield stress, i.e., a shear stress above a critical value must be applied before flow occurs, and fluids with no yield stress. This last category, considered in the present work, can be further subdivided into shear thinning and shear thickening fluids depending on how the apparent viscosity changes with shear rate.

2.3.2.1 Shear thinning or pseudoplastic fluids

The most frequently encountered time independent non-Newtonian fluid behavior in engineering applications is shear thinning or pseudoplasticity characterized by a decreasing apparent viscosity with increasing shear rate. Most shear thinning polymer melts and solutions displays Newtonian plateaus at very low and very high shear rates, where the viscosity becomes independent of shear rate. The apparent viscosity at the limiting cases of very low and very high shear rates are known as zero shear viscosity

μ_0 and infinite shear viscosity μ_∞, respectively. Accordingly, the apparent viscosity decreases from μ_0 to μ_∞ with increasing shear rate for a shear thinning fluid (Figure 2.1).

2.3.2.2 Shear thickening or dilatant fluids

Dilatant and pseudoplastic fluids are similar in that they display no yield stress; however, dilatant fluids apparent viscosity increases with increasing shear rate, giving rise to the name shear thickening. Among the time independent fluids, this sub-class attracted less attention as their behavior was considered to rarely manifest in chemical and processing industries. However, the case is no longer the same with the growing interest in handling and processing systems with high solids loadings as confirmed by the increasing number of recent scientific articles on the matter. Given the scarcity of rheological data for dilatant fluids owing to what is mentioned above, we cannot say with confidence whether such fluids also display Newtonian plateaus in the limits of very low and very high shear rates.

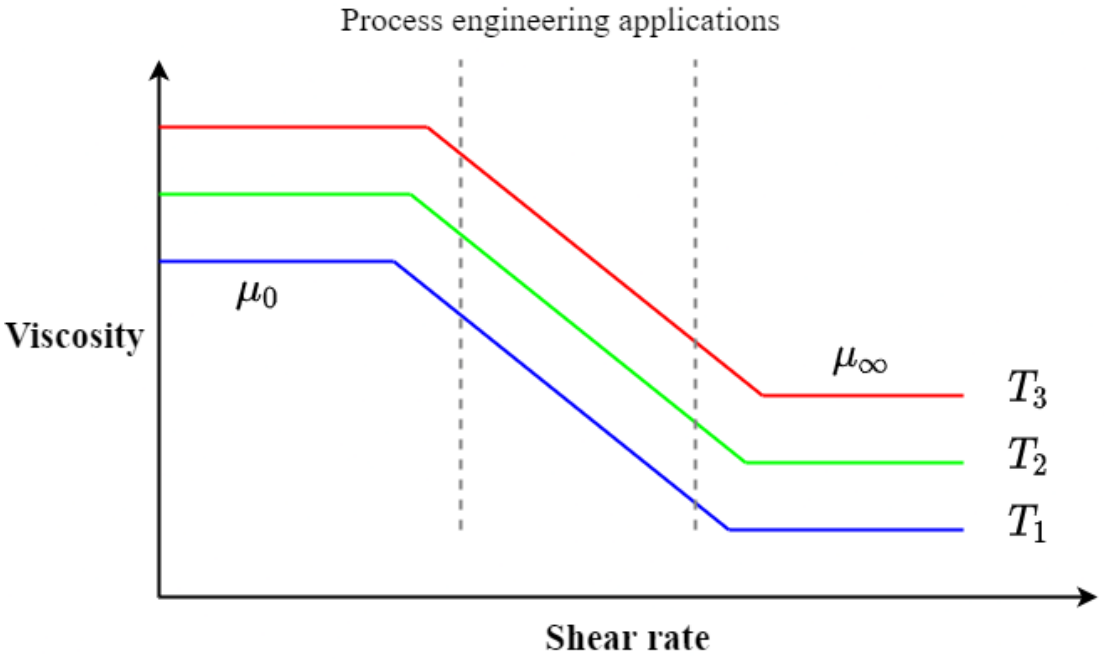

Figure 2.1. Viscosity-shear rate plot for pseudoplastic fluids at different temperatures.

2.3.3 Power-law model

Several models have been proposed by scientists to approximate the rheological data of non-Newtonian fluids through observing, studying, and characterizing their flow behavior. These mathematical models have been extensively and successfully used in fluid dynamics calculations for several decades as mentioned before. The power-law model, also known as Ostwald-de Waele model [77, 78], is one of the most well-known and widely-adopted rheological models especially for engineering purposes. The power-law model can be expressed mathematically as follows:

$$\tau = k(\dot{\gamma})^n \tag{2.13}$$

Thus, the apparent viscosity of the power-law fluid is given by:

$$\mu_a'(\dot{\gamma}) = k(\dot{\gamma})^{n-1} \tag{2.14}$$

where the positive constants k and n are the flow consistency index and behavior index, respectively.

We mentioned before the scarcity of currently available data (mostly limited to simple shear flows) for shear thickening fluids; however, the available information shows that it is possible to approximate shear stress-shear rate data for dilatant fluids by the power-law model with n greater than unity. Accordingly, based on the dimensionless flow behavior index n refelecting the closeness to Newtonian flow:

- $0 < n < 1$: the fluid shows pseudoplastic behavior, where smaller values of n lead to higher degrees of shear thinning.
- $n = 1$: the fluid shows Newtonian behavior.
- $n > 1$: the fluid behavior is said to be dilatant, where higher values of n yield greater thickening.

Many reasons are behind the popularity of the power-law model. One is its simplicity, as it only has two fitting parameters compared to other more complex models that fit non-Newtonian fluids such as Cross model and Carreau-Yasuda model containing four and five fitting constants, respectively. This is due to the fact that for many fluids, the shear stress-shear rate plots on $log - log$ coordinates can be approximated by a straight line for a given range of shear rate. Another advantage is allowing analytical solutions in a wide range of flow geometries, explaining the extensive practice of power-law

model in engineering fields as it allows to test the accuracy of numerical methods, which is the case for the present work. However, the power-law model presents one important limitation, it cannot describe neither the upper nor the lower Newtonian plateau observed experimentally for non-Newtonian fluids at very low and very high shear rates (Figure 2.1), respectively, where the power-law model gives:

$$\mu_0 \equiv \mu(0) = \infty \text{ for } n < 1 \text{ and } = 0 \text{ for } n > 1 \quad (2.15)$$

$$\mu_\infty \equiv \mu(\infty) = 0 \text{ for } n < 1 \text{ and } = \infty \text{ for } n > 1 \quad (2.16)$$

which does not agree with what is always found in experiments with non-Newtonian fluids:

$$\mu_0 \equiv \mu(0) = \text{finite value} > 0;\ \mu_\infty \equiv \mu(\infty) = \text{finite value} > 0 \quad (2.17)$$

Yet, for many flow problems, the regions of very low and very high shear rates are of lesser importance especially for process engineering applications (Figure 2.1) where most fluids' behaviors are accurately captured using the power-law model.

2.4 Conclusion

General Rheological model characterizing, under all flow conditions, viscous fluids flow behavior is described briefly while focusing on the essential. The power-law model is chosen given its many advantages, especially the possibility of establishing an analytical solution, which is one of the main assets of the present study.

CHAPTER 3 Methodology

3.1 Introduction

In this chapter, we first begin by establishing the mathematical model to simulate double-diffusive mixed convection of power-law non-Newtonian fluids. The problem's boundary conditions along with the adopted simplifying assumptions are defined, considering the investigated geometry, and the equations are written in dimensionless form in the Cartesian coordinate system. Two formulations of governing equations are exploited to solve the convection problem: the primitive variables (u, v, p, T, S) form and the stream function-vorticity formulation (ψ, Ω, T, S).

Next, two separate approaches are presented for solving fluid flow and heat and mass transfer. First, a numerical approach to solve the two-dimensional governing equations, where two methods are chosen for their advantages, the finite difference method using the stream function-vorticity formulation and the finite volume method using the primitive variables form. Second, an analytical solution derived based on the parallel flow approximation.

3.2 Mathematical formulation

3.2.1 General governing equations

Equations governing Double-diffusive fluid convection describe conservation of mass (3.1), momentum (3.2), energy (3.3), and concentration (3.4) and can be written as follows:

$$\frac{\partial \rho}{\partial t'} + div\left(\rho \overrightarrow{V'}\right) = 0 \tag{3.1}$$

$$\frac{\partial \left(\rho \overrightarrow{V'}\right)}{\partial t'} + div\left(\rho \overrightarrow{V'} \otimes \overrightarrow{V'} - \bar{\bar{\sigma}}\right) = \rho \vec{f} \tag{3.2}$$

$$\frac{\partial \left(\rho c_p T'\right)}{\partial t'} + div\left(\rho c_p T' \overrightarrow{V'} + \vec{q}\right) = \beta_T T' \frac{\partial p'}{\partial t'} + \bar{\bar{\tau}} : \overrightarrow{\overrightarrow{gradV'}} \tag{3.3}$$

$$\frac{\partial \left(\rho S'\right)}{\partial t'} + div\left(\rho S' \overrightarrow{V'} + \vec{j}\right) = 0 \tag{3.4}$$

with density ρ, specific heat capacity at constant pressure c_p, external forces applied to fluid parcels $\vec{f}$, velocity V',pressure p', temperature T', concentration S' are the main variables. To close the system, we need to establish relations defining stress tensor $\bar{\bar{\sigma}}$, viscous stress tensor $\bar{\bar{\tau}}$, heat flux vector $\vec{q}$, and mass flux vector $\vec{j}$ in terms of the above-mentioned variables. Equation (2.4) defines $\bar{\bar{\sigma}}$ while equations (2.9) and (2.11) express $\bar{\bar{\tau}}$. Heat flux vector is defined using the classical Fourier conduction law relating $\vec{q}$ to temperature gradient $\vec{\nabla}T'$ while the mass flux vector is defined with Fick's first law of diffusion relating $\vec{j}$ to concentration gradient $\vec{\nabla}S'$:

$$\vec{q} = -\lambda\vec{\nabla}T';\ \vec{j} = -D\vec{\nabla}S' \tag{3.5}$$

where the material constants λ and D are the fluid thermal conductivity and mass diffusivity, respectively. The negative signs show that heat and mass fluxes move from regions of higher temperature and concentration to regions of lower temperature and concentration with a magnitude that is proportional to temperature and concentration gradients, respectively.

3.2.2 Physical configuration

Enclosures are finite spaces confined by walls and filled with fluid. In fluid mechanics, a rectangular enclosure is by far one of the most investigated configurations. The characterization of fluid flows in such rectangular domains is a fundamental problem in fluid dynamics given the relevance to numerous important physical applications including but not limited to: cavity flows [79], polymers extrusion [80], and microfluidics [81, 82]. Convection phenomenon in rectangular enclosures, also known as internal convection, manifests in many micro and macro engineering applications ranging from electronic components cooling [72] to thermally comfortable and sustainable buildings design. Internal convection, unlike external convection, is a complex flow phenomenon that usually cannot be modeled using the simple classical boundary layer theory given that the entire fluid within the enclosure engages to the convection.

For these reasons and others discussed before, the present thesis work investigates double-diffusive mixed convection inside lid-driven rectangular cavities, the corresponding physical configuration and associated boundary conditions are given in Figure 3.1. A horizontal rectangular enclosure of length L', along the x-axis, and height

H', along the y-axis, subjected to uniform heat and mass fluxes q' and j', respectively, with horizontal walls are either motionless or slide with a uniform velocity u_0'.

3.2.3 Boundary conditions

For the boundary value problem at hand, the associated boundary conditions can be split into two categories:

3.2.3.1 Dynamical boundary conditions

For the geometry being discussed, the vertical walls present no-slip conditions while for the horizontal boundaries two cases are considered; first, the bottom wall is motionless while the top one slide with a uniform velocity (Single lid-driven boundary, $e = 0$). Second, both horizontal walls slide in opposite directions with constant velocity (Double lid-driven boundaries, $e = 1$). These boundary conditions of Dirichlet type are expressed as follows:

$$\begin{cases} u' = v' = 0 \text{ for } x' = 0 \text{ and } x' = L' \\ u' + eu_0' = v' = 0 \text{ for } y' = 0 \\ u' - u_0' = v' = 0 \text{ for } y' = H' \end{cases} \tag{3.6}$$

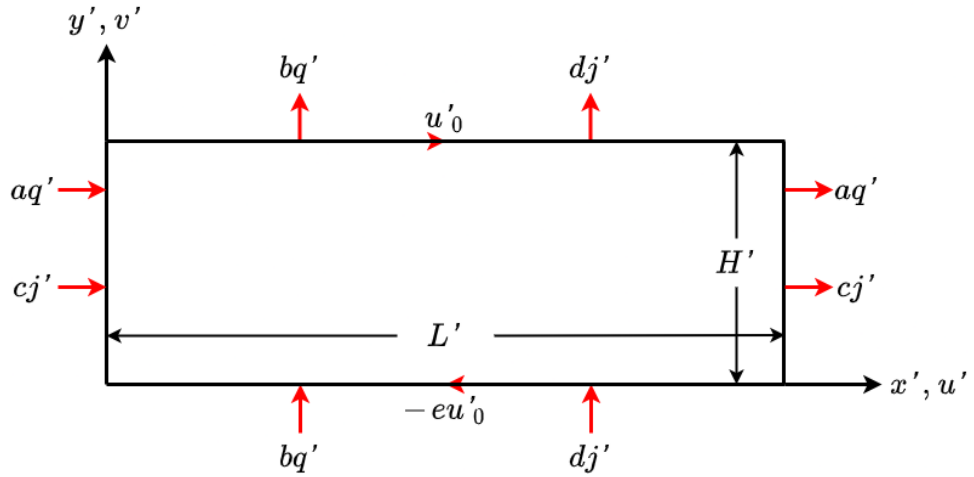

Figure 3.1. Physical model of the investigated configuration along with coordinate system and associated boundary conditions. The cavity is subjected to uniform density of heat and mass fluxes, q' and j', respectively, with horizontal boundaries are considered either motionless or slide with uniform velocity u_0'.

3.2.3.2 Thermal and solutal boundary conditions

The cavity walls are submitted to boundary conditions of Neumann type (uniform density of heat and mass fluxes) which are expressed using Fourier law and Fick's first law:

$$\begin{cases} aq' = -\lambda \frac{\partial T'}{\partial x'} \text{ and } cj' = -D \frac{\partial S'}{\partial x'} \text{ for } x' = 0 \text{ and } x' = L' \\ bq' = -\lambda \frac{\partial T'}{\partial y'} \text{ and } dj' = -D \frac{\partial S'}{\partial y'} \text{ for } y' = 0 \text{ and } y' = H' \end{cases} \quad (3.7)$$

where constants $a, b, c,$ and d define the active boundaries.

Experimentally speaking, Constant heat and mass fluxes conditions are generally considered in heat and mass transfer problems as the input power can be easily controlled and adjusted, while maintaining constant wall temperature and concentration is difficult.

3.2.4 Simplifying assumptions

In order to render the problem modelling and analysis in a more tractable way, certain assumptions are made. The introduced simplifying assumptions need to be appropriate and justified to assure the accuracy and meaningfulness of the obtained results.

- For many applications, it is adequate to consider that vector $\vec{f}$ in Eq. (3.2) is only comprised of gravity $\vec{g}$.
- The flow is laminar due to the low flow speed engendered by the small applied fluxes.
- The fluid is incompressible. For pressures close to atmospheric, liquids are a good approximation of incompressible fluids providing that $\frac{\partial \rho}{\partial p'} \approx 0$. It is therefore appropriate to neglect the term $\beta_T T' \frac{\partial p'}{\partial t'}$ in Eq. (3.3) with $\beta_T = -\left(\frac{1}{\rho}\right)\left(\frac{\partial \rho}{\partial T'}\right)_{p'}$ is fluid thermal expansion coefficient at constant pressure.
- Heat generated due to viscous friction, $\bar{\bar{\tau}} : \overline{\overline{gradV'}}$, described in Eq. (3.3) is negligeable. This remains valid as long as the viscosity of the considered non-Newtonian fluids is relatively low (layers of a low viscosity liquid move easily since there is less friction between them).

- There is no chemical reaction or internal source of heat or mass.
- Thermal radiation heat transfer is negligeable due to walls moderate temperatures [83, p. 27].
- Soret effect, i.e., mass flux generated by a temperature gradient, and Dufour effect, i.e., energy flux created by concentration differences, are negligeable.
- The fluid physical properties are temperature and concentration independent, except for viscosity and density in the gravitational term. For density, the Boussinesq approximation [84] is adopted which essentially consist of the following:
    1. The density is assumed constant, except in the gravitational term of the momentum equation $\left(\rho\vec{f} = \rho\vec{g}\right)$.
    2. In this gravitational term, the effect of pressure on density is neglected compared to that of temperature and concentration.
    3. Density $\rho(T', S')$ is given as a linear function of temperature and concentration in the vicinity of reference values T_0' and S_0' :

$$\rho(T', S') = \rho_0[1 - \beta_T(T' - T_0') - \beta_S(S' - S_0')] \tag{3.8}$$

where, ρ_0 is the reference fluid density at reference temperature and concentration $(T', S') = (T_0', S_0')$, β_T and $\beta_S \left(\beta_s = -\left(\frac{1}{\rho}\right)\left(\frac{\partial\rho}{\partial S'}\right)_{p'}\right)$ are the thermal and solutal expansion coefficients, respectively.

- The cavity third dimension is sufficiently large for the three-dimensional flow to be reduced to a two-dimensional problem, which can provide further insight into the more complex three-dimensional flows [85].

Using the aforementioned assumptions, the governing equations can be written as follows:

$$\frac{\partial u'}{\partial x'} + \frac{\partial v'}{\partial y'} = 0 \tag{3.9}$$

$$\rho_0\left(\frac{\partial u'}{\partial t'} + u'\frac{\partial u'}{\partial x'} + v'\frac{\partial u'}{\partial y'}\right) = -\frac{\partial p'}{\partial x'} + \mu'_a\left(\frac{\partial^2 u'}{\partial x'^2} + \frac{\partial^2 u'}{\partial y'^2}\right) + 2\frac{\partial \mu'_a}{\partial x'}\frac{\partial u'}{\partial x'} + \frac{\partial \mu'_a}{\partial y'}\left(\frac{\partial u'}{\partial y'} + \frac{\partial v'}{\partial x'}\right) \tag{3.10}$$

$$\rho_0\left(\frac{\partial v'}{\partial t'}+u'\frac{\partial v'}{\partial x'}+v'\frac{\partial v'}{\partial y'}\right)=-\frac{\partial p'}{\partial y'}+\mu'_a\left(\frac{\partial^2 v'}{\partial x'^2}+\frac{\partial^2 v'}{\partial y'^2}\right)$$
$$+2\frac{\partial \mu'_a}{\partial y'}\frac{\partial v'}{\partial y'}+\frac{\partial \mu'_a}{\partial x'}\left(\frac{\partial u'}{\partial y'}+\frac{\partial v'}{\partial x'}\right)+\rho_0 g[\beta_T(T'-T'_0)+\beta_S(S'-S'_0)] \quad (3.11)$$

$$\frac{\partial T'}{\partial t'}+u'\frac{\partial T'}{\partial x'}+v'\frac{\partial T'}{\partial y'}=\alpha\left[\frac{\partial^2 T'}{\partial x'^2}+\frac{\partial^2 T'}{\partial y'^2}\right] \quad (3.12)$$

$$\frac{\partial S'}{\partial t'}+u'\frac{\partial S'}{\partial x'}+v'\frac{\partial S'}{\partial y'}=D\left[\frac{\partial^2 S'}{\partial x'^2}+\frac{\partial^2 S'}{\partial y'^2}\right] \quad (3.13)$$

with the rate of deformation tensor $\bar{\bar{\dot{\gamma}}}$ expressed in the Cartesian coordinate system:

$$\bar{\bar{\dot{\gamma}}}=\begin{pmatrix}\frac{\partial u'}{\partial x'} & \frac{1}{2}\left(\frac{\partial u'}{\partial y'}+\frac{\partial v'}{\partial x'}\right) & \frac{1}{2}\left(\frac{\partial w'}{\partial x'}+\frac{\partial u'}{\partial z'}\right)\\ \frac{1}{2}\left(\frac{\partial u'}{\partial y'}+\frac{\partial v'}{\partial x'}\right) & \frac{\partial v'}{\partial y'} & \frac{1}{2}\left(\frac{\partial v'}{\partial z'}+\frac{\partial w'}{\partial y'}\right)\\ \frac{1}{2}\left(\frac{\partial w'}{\partial x'}+\frac{\partial u'}{\partial z'}\right) & \frac{1}{2}\left(\frac{\partial v'}{\partial z'}+\frac{\partial w'}{\partial y'}\right) & \frac{\partial w'}{\partial z'}\end{pmatrix} \quad (3.14)$$

u', v', w' are the velocity components in x', y', z' directions, respectively. Thus, and given the two-dimensional flow assumption, the rate of deformation tensor can be simplified as follows:

$$\bar{\bar{\dot{\gamma}}}=\begin{pmatrix}\frac{\partial u'}{\partial x'} & \frac{1}{2}\left(\frac{\partial u'}{\partial y'}+\frac{\partial v'}{\partial x'}\right) & 0\\ \frac{1}{2}\left(\frac{\partial u'}{\partial y'}+\frac{\partial v'}{\partial x'}\right) & \frac{\partial v'}{\partial y'} & 0\\ 0 & 0 & 0\end{pmatrix} \quad (3.15)$$

Considering Eq. (2.14), the apparent viscosity μ'_a can be expressed as:

$$\mu'_a=k\left[2\left[\left(\frac{\partial u\prime}{\partial x\prime}\right)^2+\left(\frac{\partial v\prime}{\partial y\prime}\right)^2\right]+\left[\frac{\partial u\prime}{\partial y\prime}+\frac{\partial v\prime}{\partial x\prime}\right]^2\right]^{\frac{n-1}{2}} \quad (3.16)$$

while α $\left(\alpha=\frac{\lambda}{\rho c_p}\right)$ is the fluid thermal diffusivity.

3.2.5 Nondimensionalization

Nondimensionalization denotes the process of removing physical dimensions from the problem equations with a suitable change of variables in order to obtain a purely mathematical problem. For the present study, and in order to make dependent and independent variables of the problem dimensionless, the following reference quantities are chosen: H', H'^2/α, $\rho_0(\alpha^2/H'^2)$, α/H', $q'H'/\lambda$, and $j'H'/D$ corresponding to

length, time, pressure, velocity, characteristic temperature, and characteristic concentration, respectively. The dimensionless variables are given in Table 3.1.

By introducing these variables, the dimensionless forms of governing equations (3.9) – (3.13) and associated boundary conditions (3.6) – (3.7) are obtained:

$$\frac{\partial u}{\partial x} + \frac{\partial v}{\partial y} = 0 \tag{3.17}$$

$$\frac{\partial u}{\partial t} + u\frac{\partial u}{\partial x} + v\frac{\partial u}{\partial y} = -\frac{\partial p}{\partial x} + Pr\left[\mu_a\left(\frac{\partial^2 u}{\partial x^2} + \frac{\partial^2 u}{\partial y^2}\right) + 2\frac{\partial \mu_a}{\partial x}\frac{\partial u}{\partial x} + \frac{\partial \mu_a}{\partial y}\left(\frac{\partial u}{\partial y} + \frac{\partial v}{\partial x}\right)\right] \tag{3.18}$$

$$\frac{\partial v}{\partial t} + u\frac{\partial v}{\partial x} + v\frac{\partial v}{\partial y} = -\frac{\partial p}{\partial y} + Pr\left[\mu_a\left(\frac{\partial^2 v}{\partial x^2} + \frac{\partial^2 v}{\partial y^2}\right) + 2\frac{\partial \mu_a}{\partial y}\frac{\partial v}{\partial y} + \frac{\partial \mu_a}{\partial x}\left(\frac{\partial u}{\partial y} + \frac{\partial v}{\partial x}\right)\right] + Ra_T Pr[T + NS] \tag{3.19}$$

$$\frac{\partial T}{\partial t} + u\frac{\partial T}{\partial x} + v\frac{\partial T}{\partial y} = \left[\frac{\partial^2 T}{\partial x^2} + \frac{\partial^2 T}{\partial y^2}\right] \tag{3.20}$$

$$\frac{\partial S}{\partial t} + u\frac{\partial S}{\partial x} + v\frac{\partial S}{\partial y} = \frac{1}{Le}\left[\frac{\partial^2 S}{\partial x^2} + \frac{\partial^2 S}{\partial y^2}\right] \tag{3.21}$$

$$u = v = 0 \; and \; \frac{\partial T}{\partial x} + a = \frac{\partial S}{\partial x} + c = 0 \quad for \; x = 0 \; and \; x = A; \tag{3.22}$$

$$u + ePe = v = 0 \; and \; \frac{\partial T}{\partial y} + b = \frac{\partial S}{\partial y} + d = 0 \; for \; y = 0; \tag{3.23}$$

Table 3.1 – Dimensionless variables.

Coordinate system	$(x, y) = \frac{(x', y')}{H'}$	**Time**	$t = \frac{t'}{H'^2/\alpha}$
Pressure	$p = \frac{p'}{\rho_0(\alpha^2/H'^2)}$	**Velocity**	$(u, v) = \frac{(u', v')}{\alpha/H'}$
Temperature	$T = \frac{(T' - T_0')}{\Delta T^*}$; $\Delta T^* = \frac{q'H'}{\lambda}$	**Concentration**	$S = \frac{(S' - S_0')}{\Delta S^*}$; $\Delta S^* = \frac{j'H'}{D}$

$$u - Pe = \ v = 0 \ and \ \frac{\partial T}{\partial y} + b = \frac{\partial S}{\partial y} + d = 0 \ for \ y = 1 \tag{3.24}$$

where:

$$\mu_a = \left[2\left[\left(\frac{\partial u}{\partial x}\right)^2 + \left(\frac{\partial v}{\partial y}\right)^2\right] + \left[\frac{\partial u}{\partial y} + \frac{\partial v}{\partial x}\right]^2\right]^{\frac{n-1}{2}} \tag{3.25}$$

In the above resulting equations, six dimensionless parameters emerge, namely the cavity aspect ratio A, generalized Prandtl number Pr, Péclet number Pe, thermal Rayleigh number Ra_T, Lewis number Le, and buoyancy ratio N expressed as follows:

$$A = \frac{L'}{H'}; \ \ Pr = \frac{\left(\frac{k}{\rho}\right){H'}^{2-2n}}{\alpha^{2-n}}; \ \ Pe = \frac{u_0' H'}{\alpha}; Ra_T = \frac{g\beta_T {H'}^{2n+2} q'}{\left(\frac{k}{\rho}\right)\alpha^n \lambda};$$

$$Le = \frac{\alpha}{D}; \ \ N = \frac{\beta_S \Delta S^*}{\beta_T \Delta T^*} \tag{3.26}$$

- Prandtl number defines the ratio of momentum diffusivity (kinematic viscosity) to thermal conductivity.
- Péclet number is the ratio of thermal energy transported by fluid motion (heat convection) to thermal energy conducted within the fluid (heat diffusion).
- Thermal Rayleigh number conceptually measures the relative importance between the effects of buoyancy forces, from Archimedes' principle, and their counteracting effects: friction, due to viscosity forces, and heat diffusion which is by conduction. Therefore, it can determine whether buoyancy-driven flow (natural convection) plays an important role in heat and mass transfer.
- Lewis number characterizes fluid flows where heat and mass transfer occur simultaneously and is defined as the ratio of thermal diffusivity to mass diffusivity. Therefore, Lewis number puts thermal and concentration boundary layer thicknesses in correlation.
- Buoyancy ratio describes the relative strengths of solutal and thermal buoyancy forces.

For $n = 1$, Pr and Ra_T find their Newtonian expressions providing that k is replaced by Newtonian viscosity μ.

3.2.6 Heat and mass transfer

Enhancing heat and mass transfer rates has been the key for designing efficient compact systems given that an increase in the transfer rates influences the design and overall efficiency of the system. Dimensionless Nusselt and Sherwood numbers provide a measure of heat and mass transfer, respectively.

3.2.6.1 Heat and mass transfer in the horizontal direction

Nusselt and Sherwood numbers quantifying local heat and mass transfer, respectively, in the horizontal direction are defined as follows:

$$Nu_h(y) = \frac{a\, q'L'}{\lambda \Delta T'_h} = \frac{a}{(\Delta T_h(y)/A)} \tag{3.27}$$

$$Sh_h(y) = \frac{c\, j'L'}{D \Delta S'_h} = \frac{c}{(\Delta S_h(y)/A)} \tag{3.28}$$

where $\Delta T_h(y) = T(0,y) - T(A,y)$ and $\Delta S_h(y) = S(0,y) - S(A,y)$ represent the local dimensionless temperature and concentration difference between the two vertical walls $x = 0$ and $x = A$, respectively.

However, definitions (3.27) and (3.28) have the disadvantage of introducing inaccuracies into the values of Nu_h and Sh_h due to the edge effects where the flow is more complex. Further, the numerical solution will be compared to the analytical one, which will be established after this, valid in the core section of the cavity. As such, and by analogy to (3.27) and (3.28), Nu_h and Sh_h are evaluated far from the vertical walls of the cavity [86] considering two symmetrical vertical sections with respect to the central section at ($x = A/2$):

$$Nu_h(y) = a \lim_{\delta x \to 0} \frac{\delta x}{\delta T} = a \lim_{\delta x \to 0} \frac{1}{\left(\frac{\delta T}{\delta x}\right)} = -\mathrm{a}/(\partial T \,/\, \partial x)_{x=A/2} \tag{3.29}$$

$$Sh_h(y) = c \lim_{\delta x \to 0} \frac{\delta x}{\delta S} = c \lim_{\delta x \to 0} \frac{1}{\left(\frac{\delta S}{\delta x}\right)} = -c/(\partial S \,/\, \partial x)_{x=A/2} \tag{3.30}$$

where, δx is the horizontal distance between the two infinitely close sections considered above.

As for the average horizontal Nusselt number describing the overall horizontal heat transfer and the average horizontal Sherwood number describing the overall horizontal mass transfer, the following equations are used respectively:

$$\overline{Nu_h} = \int_0^1 Nu_h(y)dy \tag{3.31}$$

$$\overline{Sh_h} = \int_0^1 Sh_h(y)dy \tag{3.32}$$

3.2.6.2 Heat and mass transfer in the vertical direction

Nusselt and Sherwood numbers measuring local heat and mass transfer in the vertical direction, respectively, are expressed as follows:

$$Nu_v(x) = \frac{bq'H'}{\lambda \Delta T_v'} = \frac{b}{\Delta T_v(x)} \tag{3.33}$$

$$Sh_v(x) = \frac{dj'H'}{D\Delta S_v'} = \frac{d}{\Delta S_v(x)} \tag{3.34}$$

with $\Delta T_v(x) = T(x,0) - T(x,1)$ and $\Delta S_v(x) = S(x,0) - S(x,1)$ are the local dimensionless temperature and concentration differences between the two horizontal walls $y = 0$ and $y = 1$, respectively. We note that for parallel flows, $Nu_v(x)$ and $Sh_v(x)$ remain unchanged in the central region of the cavity.

By integrating Eqs. (3.33) and (3.34) along the horizontal wall, the average values of Nusselt and Sherwood numbers measuring the overall vertical heat and mass transfer rates, respectively, are obtained:

$$\overline{Nu_v} = \frac{1}{A}\int_0^A Nu_v(x)dx \tag{3.35}$$

$$\overline{Sh_v} = \frac{1}{A}\int_0^A Sh_v(x)dx \tag{3.36}$$

3.3 Numerical approach

Numerical methods have been indisputably the most adopted approaches for modeling and solving convective fluid flows and heat and mass transfer given their ability to handle the complex nonlinear nature of equations governing such flows, which can rarely be handled by other approaches in very particular cases (e.g., analytical approach established in the next section based on the parallel flow approximation). And while an analytical solution of a partial differential equation (PDE) results in the value of φ (e.g., u, v, T, S) as a function of independent variables (x, y, t), a numerical solution provides the value of φ at a discrete number of domain points known as grid points, which can also be referred to, depending on the method at hand, as nodes or cell centroids. A

discretization method is used to convert a governing equation into a set of equations for the discrete values of φ.

The numerical methods used to solve governing PDEs are characterized in terms of accuracy, consistency, stability, and convergence. The accuracy denotes the closeness of numerical solution to the exact solution. Usually however, the exact solution is unknown and we talk about the truncation error (caused by the numerical approximations of the derivatives) of a discretization method. A numerical method is said to be consistent if the truncation error tends to diminish with mesh refinement (step size Δt, Δx, or Δy tends to zero). A stable numerical method is one for which the error does not grow with time (or number of iterations). Finally, the convergence of a numerical method is ensured if it is consistent and stable.

Different numerical methods are used in the literature to solve flow problems; however, one of two methods is commonly encountered, Finite Difference Method (FDM) or Finite Volume Method (FVM). In the present study, and in order to numerically solve the system of governing equations (3.17) - (3.21) and associated boundary conditions (3.22) – (3.24), the two numerical methods are adopted.

3.3.1 Finite Difference Method

The finite difference method is one of the first numerical approaches applied to solve differential equations. It was first used by L. Euler around 1768 in one dimensional space then extended to two-dimensional space probably by C. Runge in 1908. The principle is to locally discretize the derivatives of flow variables using Taylor series expansion on each of the domain grid points. The finite difference method is widely used given its simplicity (easy to understand and implement especially for simple geometries), accuracy, stability, and rapid convergence. However, the range of applications is limited as it requires a structured grid.

For incompressible two-dimensional flows, it is possible to recast the primitive variables (u, v, p, T, S) form of governing equations (3.17) – (3.21) in an alternative stream function-vorticity formulation (ψ, Ω, T, S). This is done by introducing a change of variables that replaces velocity components with stream function ψ and vorticity Ω as follows:

$$u = \frac{\partial \psi}{\partial y}; \qquad v = -\frac{\partial \psi}{\partial x} \tag{3.37}$$

$$\Omega = \frac{\partial v}{\partial x} - \frac{\partial u}{\partial y} \tag{3.38}$$

By introducing these new variables, the dimensionless equations governing the convection become:

$$\frac{\partial \Omega}{\partial t} + \frac{\partial (u\Omega)}{\partial x} + \frac{\partial (v\Omega)}{\partial y} = Pr\left[\mu_a \left(\frac{\partial^2 \Omega}{\partial x^2} + \frac{\partial^2 \Omega}{\partial y^2}\right) + 2\left(\frac{\partial \mu_a}{\partial x}\frac{\partial \Omega}{\partial \mathrm{x}} + \frac{\partial \mu_a}{\partial y}\frac{\partial \Omega}{\partial \mathrm{y}}\right)\right] + S_\Omega \tag{3.39}$$

$$\frac{\partial T}{\partial t} + \frac{\partial (uT)}{\partial x} + \frac{\partial (vT)}{\partial y} = \left[\frac{\partial^2 T}{\partial x^2} + \frac{\partial^2 T}{\partial y^2}\right] \tag{3.40}$$

$$\frac{\partial S}{\partial t} + \frac{\partial (uS)}{\partial x} + \frac{\partial (vS)}{\partial y} = \frac{1}{Le}\left[\frac{\partial^2 S}{\partial x^2} + \frac{\partial^2 S}{\partial y^2}\right] \tag{3.41}$$

and

$$\frac{\partial^2 \psi}{\partial x^2} + \frac{\partial^2 \psi}{\partial y^2} = -\Omega \tag{3.42}$$

with

$$S_\Omega = Pr\left[\left(\frac{\partial^2 \mu_a}{\partial x^2} - \frac{\partial^2 \mu_a}{\partial y^2}\right)\left(\frac{\partial u}{\partial y} + \frac{\partial v}{\partial x}\right) - 2\frac{\partial^2 \mu_a}{\partial x \partial y}\left(\frac{\partial u}{\partial x} - \frac{\partial v}{\partial y}\right)\right] + Pr\, Ra_T\left[\frac{\partial T}{\partial x} + N\frac{\partial S}{\partial x}\right] \tag{3.43}$$

The two momentum equations (3.18) and (3.19) combine into one vorticity transport equation (3.39) by eliminating pressure (take the $\partial/\partial y$ of the first equation and $\partial/\partial x$ of the second equation then subtract). Further, flows for which velocity field is specified by a stream function automatically satisfy the continuity equation since:

$$\frac{\partial u}{\partial x} + \frac{\partial v}{\partial y} = \frac{\partial}{\partial x}\left(\frac{\partial \psi}{\partial y}\right) + \frac{\partial}{\partial y}\left(-\frac{\partial \psi}{\partial x}\right) = \frac{\partial^2 \psi}{\partial x \partial y} - \frac{\partial^2 \psi}{\partial x \partial y} = 0 \tag{3.44}$$

thus, the continuity equation no longer needs to be addressed. As a result, an additional equation for ψ is required to solve the problem. For this, the Poisson equation (3.42) is obtained by substituting the definition of velocity components in terms of stream function into equation (3.38). Finally, the governing equations are replaced by a set of four partial differential equations instead of five.

The associated boundary conditions are given as follows:

$$u = v = \psi = 0 \; and \; \frac{\partial T}{\partial x} + a = \frac{\partial S}{\partial x} + c = 0 \quad for \; x = 0 \; and \; x = A; \quad (3.45)$$

$$u + ePe = v = \psi = 0 \; and \; \frac{\partial T}{\partial y} + b = \frac{\partial S}{\partial y} + d = 0 \; for \; y = 0; \quad (3.46)$$

$$u - Pe = v = \psi = 0 \; and \; \frac{\partial T}{\partial y} + b = \frac{\partial S}{\partial y} + d = 0 \; for \; y = 1 \quad (3.47)$$

The finite difference method is applied to solve the system of governing equations (3.39) – (3.42) and boundary conditions (3.45) – (3.47). The procedure is described in further details in [87]. One difference is that instead of using Woods approach [88] for evaluating vorticity along the sliding horizontal walls, which leads to inaccurate results in the case of driven cavities, equation (3.38) is discretized as follows:

For bottom wall:

$$\Omega_{i,1} = \frac{v_{i+1,1} - v_{i-1,1}}{2\Delta x} - \frac{4u_{i,2} - u_{i,3} - 3u_{i,1}}{2\Delta y} \quad (3.48)$$

For top wall:

$$\Omega_{i,m_y+1} = \frac{v_{i+1,m_y+1} - v_{i-1,m_y+1}}{2\Delta x} - \frac{u_{i,m_y-1} - 4u_{i,m_y} + 3u_{i,m_y+1}}{2\Delta y} \quad (3.49)$$

with m_y is the number of intervals in the 2D rectangular uniform grid following the y direction.

3.3.2 Finite Volume Method

The finite difference method presented above is based on nodal relations for partial differential equations. In contrast, the finite volume method is based on the discretization of conservation laws (Eqs. (3.17) – (3.21)) in integral form. The finite volume method consists of partitioning the computational domain into a finite set of elementary or control volumes surrounding the mesh points on which we integrate the partial differential equations. In a two-dimensional case, these volumes are of size $\Delta x \times \Delta y$ (Figure 3.2). The physical variables we want to compute are assumed constant in each control volume.

Since the finite volume method discretize the balance equations (conservation laws) directly, it has an advantage over the finite difference method as it imposes conservation

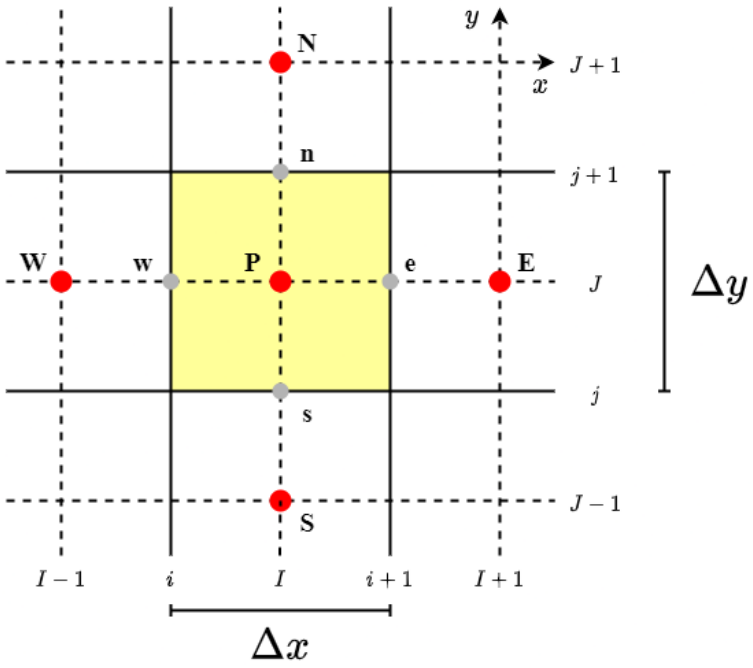

Figure 3.2. Two-dimensional control volume for finite volume method.

of quantities at discretized level, i.e., mass, momentum, energy, and concentration are locally conserved (fluxes entering a given volume are equal to those leaving the adjacent volume). Because of this virtue, FVM has been widely used in numerous fields such as fluid mechanics and petroleum engineering, as well as in heat and mass transfer.

The conservations laws (Eqs. (3.17) – (3.21)) can be written in the following form:

$$\frac{\partial \phi}{\partial t} + \frac{\partial}{\partial x}\left(u\phi - \Gamma \frac{\partial \phi}{\partial x}\right) + \frac{\partial}{\partial y}\left(v\phi - \Gamma \frac{\partial \phi}{\partial y}\right) = S_\phi \tag{3.50}$$

with Γ and S_ϕ are the diffusion coefficient and the source term, respectively.

Integrating Eq. (3.50) over the control volume, the two-dimensional discretization equation expressing the dependence of ϕ_P on the values of neighboring grid points $\phi_E, \phi_W, \phi_N,$ and ϕ_S is written as:

$$a_P \phi_P = a_E \phi_E + a_W \phi_W + a_N \phi_N + a_S \phi_S + b \tag{3.51}$$

For more information on the finite volume method, refer to [89]. The discretized equations system is then solved using a line-by-line solver combining Tri-Diagonal Matrix Algorithm (TDMA) and Gauss-Seidel method.

Unlike for compressible flows where the pressure can be obtained from density and temperature by using the equation of state $p = p(\rho, T)$, for incompressible flows the density is constant and therefore independent of pressure, so we don't have a separate equation for pressure. However, a correct pressure field need to be supplied into the momentum equations in order for the resulting velocity field to satisfy the continuity constraint. The SIMPLE (Semi-Implicit Method for Pressure-Linked Equations) algorithm [90] is an iterative procedure adopted to solve the pressure–velocity linkage where a pressure correction equation is derived from the continuity equation. The process is iterated until convergence evaluated with the threshold:

$$MAX\left(\frac{|f^{k+1}-f^{k}|}{|f^{k+1}|}\right) \leq 10^{-7} \tag{3.52}$$

where, f^{k} is the value of u, v, p, T, or S at the k^{th} iteration level.

3.4 Analytical approach

The Navier-Stokes equations are highly complex partial differential equations given their nonlinear character, making exact analytical solutions impossible in general. However, it is possible to find analytical solutions in some particular cases based on assumptions about the fluid, the problem geometry, or about the flow structure. Parallel flow is one of the cases, in which only one velocity component is different from zero for two-dimensional flows.

In the present work and for shallow rectangular cavities $(A >> 1)$, the analytical solution is derived based on the flow parallel aspect and the stratification of temperature and concentration fields leading to the following simplifications:

$$u(x,y) = u(y), v(x,y) = 0, \psi(x,y) = \psi(y),$$

$$T(x,y) = C_T\left(x - \frac{A}{2}\right) + \theta_T(y) \; and \; S(x,y) = C_S\left(x - \frac{A}{2}\right) + \theta_S(y) \tag{3.53}$$

where, $C_T = \left(\frac{\partial T}{\partial x}\right)_{x=A/2}$ and $C_S = \left(\frac{\partial S}{\partial x}\right)_{x=A/2}$ are the unknown constant temperature gradient and the unknown constant concentration gradient in the x-direction, respectively.

3.4.1 Approximate governing equations

The non-dimensional governing equations (3.17) – (3.21) are simplified using the above approximations as follows:

$$\frac{d^2}{dy^2}\left[\left|\frac{du}{dy}\right|^{n-1}\frac{du}{dy}\right] = ERa_T \tag{3.54}$$

$$C_T u = \frac{d^2\theta_T(y)}{dy^2} \tag{3.55}$$

$$C_S u = \frac{1}{Le}\frac{d^2\theta_S(y)}{dy^2} \tag{3.56}$$

with:

$$E = C_T + NC_S \tag{3.57}$$

The associated boundary conditions reduce to:

$$u + ePe = \psi = \frac{d\theta_T(y)}{dy} + b = \frac{d\theta_S(y)}{dy} + d = 0 \text{ for } y = 0; \tag{3.58}$$

$$u - Pe = \psi = \frac{d\theta_T(y)}{dy} + b = \frac{d\theta_S(y)}{dy} + d = 0 \text{ for } y = 1 \tag{3.59}$$

with:

$$\int_0^1 u(y)dy = 0 \tag{3.60}$$

$$\int_0^1 \theta_T(\mathrm{y})dy = 0 \tag{3.61}$$

$$\int_0^1 \theta_S(\mathrm{y})dy = 0 \tag{3.62}$$

as return flow, mean temperature, and mean concentration conditions, respectively.

3.4.2 Integration of approximate governing equations for double lid-driven cavities

Integrating the system of equations (3.54) – (3.56) and conditions (3.58) – (3.62) leads to the analytic expressions of velocity, temperature, and concentration. However, taking into account the nature of the governing equations, such complex calculations require special numerical treatment. The fluids' nonlinear behavior and du/dy sign change

induced by the return flow cause the velocity expression to be different according to the value of y: $0 \le y \le y_0$, $y_0 \le y \le y_1$, or $y_1 \le y \le 1$, where y_0 and y_1 are the values of y for which $\frac{du}{dy} = 0$ ($y_1 = 1 - y_0$ because the flow is centro-symmetric in the core region for double lid-driven cavities). To simplify the analytical equations, the function $f(y) = \frac{y^2}{2} - \frac{y}{2} + \frac{y_0 y_1}{2}$ is introduced. Accordingly, for:

- $0 \le y \le y_0$

$$u(y) = E^{\frac{1}{n}} Ra_T^{\frac{1}{n}} F(y) - Pe \tag{3.63}$$

$$\theta_T(y) = C_T E^{\frac{1}{n}} Ra_T^{\frac{1}{n}} \left[G(y) - \int_0^1 G(y)dy \right] - C_T Pe \frac{y^2}{2} + C_T \frac{Pe}{6} - b(y - \tfrac{1}{2}) \tag{3.64}$$

$$\theta_S(y) = LeC_S E^{\frac{1}{n}} Ra_T^{\frac{1}{n}} \left[G(y) - \int_0^1 G(y)dy \right] - LeC_S Pe \frac{y^2}{2} + LeC_S \frac{Pe}{6} - d(y - \tfrac{1}{2}) \tag{3.65}$$

where:

$$F(y) = \int_0^y f(y)^{1/n} dy \tag{3.66}$$

$$G(y) = \int_0^y \int_0^y \int_0^y f(y)^{\frac{1}{n}} dydydy \tag{3.67}$$

- $y_0 \le y \le y_1$

$$u(y) = E^{\frac{1}{n}} Ra_T^{\frac{1}{n}} F(y) - Pe \tag{3.68}$$

$$\theta_T(y) = C_T E^{\frac{1}{n}} Ra_T^{\frac{1}{n}} \left[G(y) - \int_0^1 G(y)dy \right] - C_T Pe \frac{y^2}{2} + C_T \frac{Pe}{6} - b(y - \tfrac{1}{2}) \tag{3.69}$$

$$\theta_S(y) = LeC_S E^{\frac{1}{n}} Ra_T^{\frac{1}{n}} \left[G(y) - \int_0^1 G(y)dy \right] - LeC_S Pe \frac{y^2}{2} + LeC_S \frac{Pe}{6} - d(y - \tfrac{1}{2}) \tag{3.70}$$

where:

$$F(y) = \int_0^{y_0} f(y)^{\frac{1}{n}} dy + \int_y^{y_0} [-f(y)]^{\frac{1}{n}} dy \tag{3.71}$$

$$G(y) = \frac{(y-y_0)^2}{2} \int_0^{y_0} f(y)^{\frac{1}{n}} dy + \int_{y_0}^{y} \left[\int_{y_0}^{y} \left[\int_{y}^{y_0} [-f(y)]^{\frac{1}{n}} dy \right] dy \right] dy$$
$$+(y-y_0) \int_0^{y_0} \left[\int_0^{y} f(y)^{\frac{1}{n}} dy \right] dy + \int_0^{y_0} \left[\int_0^{y} \left[\int_0^{y} f(y)^{1/n} dy \right] dy \right] dy \tag{3.72}$$

- $y_1 \leq y \leq 1$

$$u(y) = E^{\frac{1}{n}} Ra_T{}^{\frac{1}{n}} \left(F(y) - F(1) \right) + Pe \tag{3.73}$$

$$\theta_T(y) = C_T E^{\frac{1}{n}} Ra_T{}^{\frac{1}{n}} \left[\begin{array}{c} G(y) - \int_0^1 G(y) dy + \\ \left(\frac{1}{2} - y \right) \int_0^1 F(y) dy - F(1) \left(\frac{y^2}{2} - y + \frac{1}{3} \right) \end{array} \right]$$
$$+C_T Pe(\frac{y^2}{2} - y + \frac{1}{3}) - b(y - \frac{1}{2}) \tag{3.74}$$

$$\theta_S(y) = LeC_S E^{\frac{1}{n}} Ra_T{}^{\frac{1}{n}} \left[\begin{array}{c} G(y) - \int_0^1 G(y) dy + \\ \left(\frac{1}{2} - y \right) \int_0^1 F(y) dy - F(1) \left(\frac{y^2}{2} - y + \frac{1}{3} \right) \end{array} \right]$$
$$+LeC_S Pe(\frac{y^2}{2} - y + \frac{1}{3}) - d(y - \frac{1}{2}) \tag{3.75}$$

where:

$$F(y) = \int_0^{y_0} f(y)^{1/n} dy + \int_{y_1}^{y_0} [-f(y)]^{\frac{1}{n}} dy + \int_{y_1}^{y} f(y)^{\frac{1}{n}} dy \tag{3.76}$$

$$F(1) = \int_0^{y_0} f(y)^{1/n} dy + \int_{y_1}^{y_0} [-f(y)]^{\frac{1}{n}} dy + \int_{y_1}^{1} f(y)^{\frac{1}{n}} dy \tag{3.77}$$

$$G(y) = \frac{(y-y_1)(y+y_1-2)}{2}\left[\int_0^{y_0} f(y)^{\frac{1}{n}}dy \; + \int_{y_1}^{y_0}[-f(y)]^{\frac{1}{n}}dy\right] + \int_{y_1}^{y}\left[\int_1^{y}\left[\int_{y_1}^{y} f(y)^{\frac{1}{n}}dy\right]dy\right]dy + \int_{y_0}^{y_1}\left[\int_{y_0}^{y}\left[\int_{y}^{y_0}[-f(y)]^{\frac{1}{n}}dy\right]dy\right]dy + \frac{(y_1-y_0)^2}{2}\int_0^{y_0} f(y)^{\frac{1}{n}}dy \; + (y_1-y_0)\int_0^{y_0}\left[\int_0^{y} f(y)^{\frac{1}{n}}dy\right]dy + \int_0^{y_0}\left[\int_0^{y}\left[\int_0^{y} f(y)^{1/n}dy\right]dy\right]dy \tag{3.78}$$

The expression of ψ can be obtained by integrating Eq. (3.37) while taking into account the corresponding boundary conditions. As a result, the stream function at the center of the cavity ψ_c can be expressed as follows:

$$\psi_c = \psi\left(\frac{A}{2}, \frac{1}{2}\right) = \frac{E^{1/n}Ra_T{}^{1/n}}{R} - \frac{Pe}{2} \tag{3.79}$$

with:

$$R = \begin{bmatrix}\left(\frac{1}{2}-y_0\right)\int_0^{y_0} f(y)^{\frac{1}{n}}dy \; + \int_{y_0}^{\frac{1}{2}}\left[\int_y^{y_0}[-f(y)]^{\frac{1}{n}}dy\right]dy + \\ \int_0^{y_0}\left[\int_0^{y} f(y)^{\frac{1}{n}}dy\right]dy\end{bmatrix}^{-1} \tag{3.80}$$

Using Eq. (3.79), $u(y)$, $\theta_T(y)$, and $\theta_S(y)$ are expressed as follows:

- $0 \le y \le y_0$

$$u(y) = R\left(\psi_c + \frac{Pe}{2}\right)F(y) - Pe \tag{3.81}$$

$$\theta_T(y) = C_T R\left(\psi_c + \frac{Pe}{2}\right)\left[G(y) - \int_0^1 G(y)dy\right] - C_T Pe\frac{y^2}{2} + C_T\frac{Pe}{6} - b\left(y-\frac{1}{2}\right) \tag{3.82}$$

$$\theta_S(y) = LeC_S R\left(\psi_c + \frac{Pe}{2}\right)\left[G(y) - \int_0^1 G(y)dy\right] - LeC_S Pe\frac{y^2}{2} + LeC_S\frac{Pe}{6} - d\left(y-\frac{1}{2}\right) \tag{3.83}$$

- $y_0 \leq y \leq y_1$

$$u(y) = R\left(\psi_c + \frac{Pe}{2}\right)F(y) - Pe \tag{3.84}$$

$$\theta_T(y) = C_T R\left(\psi_c + \frac{Pe}{2}\right)\left[G(y) - \int_0^1 G(y)dy\right] - C_T Pe\frac{y^2}{2} + C_T\frac{Pe}{6} - b\left(y - \frac{1}{2}\right) \tag{3.85}$$

$$\theta_S(y) = LeC_S R\left(\psi_c + \frac{Pe}{2}\right)\left[G(y) - \int_0^1 G(y)dy\right] - LeC_S Pe\frac{y^2}{2} + LeC_S\frac{Pe}{6} - d\left(y - \frac{1}{2}\right) \tag{3.86}$$

- $y_1 \leq y \leq 1$

$$u(y) = R\left(\psi_c + \frac{Pe}{2}\right)\left(F(y) - F(1)\right) + Pe \tag{3.87}$$

$$\theta_T(y) = C_T R\left(\psi_c + \frac{Pe}{2}\right)\left[\begin{array}{c} G(y) - \int_0^1 G(y)dy + \left(\frac{1}{2} - y\right)\int_0^1 F(y)dy \\ -F(1)\left(\frac{y^2}{2} - y + \frac{1}{3}\right) \end{array}\right] + C_T Pe\left(\frac{y^2}{2} - y + \frac{1}{3}\right) - b\left(y - \frac{1}{2}\right) \tag{3.88}$$

$$\theta_S(y) = LeC_S R\left(\psi_c + \frac{Pe}{2}\right)\left[\begin{array}{c} G(y) - \int_0^1 G(y)dy + \left(\frac{1}{2} - y\right)\int_0^1 F(y)dy \\ -F(1)\left(\frac{y^2}{2} - y + \frac{1}{3}\right) \end{array}\right] + LeC_S Pe\left(\frac{y^2}{2} - y + \frac{1}{3}\right) - d\left(y - \frac{1}{2}\right) \tag{3.89}$$

The parallel flow approximation builds upon observations made in the core region away from the more complicated flow near the vertical edges of the cavity. Therefore, the exact thermal and solutal boundary conditions in the x-direction shown in Eq. (3.45) cannot be reproduced with this approximation. However, equivalent energy and concentration flux conditions across a transversal direction, at any x, can be obtained [91]:

$$\int_0^1 -\frac{\partial T}{\partial x}dy + \int_0^1 uTdy = \int_0^1 -\left(\frac{\partial T}{\partial x}\right)_{x=0\ or\ x=A} dy \tag{3.90}$$

$$\int_0^1 -\frac{\partial S}{\partial x}dy + Le\int_0^1 uSdy = \int_0^1 -\left(\frac{\partial S}{\partial x}\right)_{x=0\ or\ x=A} dy \tag{3.91}$$

In the parallel flow region and given conditions (3.45), Eqs. (3.90) and (3.91) become:

$$-C_T + \int_0^1 u(y)\theta_T(y)dy = a \tag{3.92}$$

$$-C_S + Le\int_0^1 u(y)\theta_S(y)dy = c \tag{3.93}$$

Replacing $u(y)$, $\theta_T(y)$, and $\theta_S(y)$ by their respective expressions:

$$C_T = \frac{a-b\left(R\left(\psi_c+\frac{Pe}{2}\right)Z+Pe\left({y_1}^2-y_1\right)\right)}{R^2\left(\psi_c+\frac{Pe}{2}\right)^2 X+PeR\left(\psi_c+\frac{Pe}{2}\right)Y+Pe^2\left(\frac{{y_1}^2-y_1}{2}\right)-1} \tag{3.94}$$

$$C_S = \frac{c-d\left(LeR\left(\psi_c+\frac{\mathrm{Pe}}{2}\right)Z+LePe\left({y_1}^2-y_1\right)\right)}{Le^2R^2\left(\psi_c+\frac{\mathrm{Pe}}{2}\right)^2 X+Le^2PeR\left(\psi_c+\frac{\mathrm{Pe}}{2}\right)Y+Le^2Pe^2\left(\frac{{y_1}^2-y_1}{2}\right)-1} \tag{3.95}$$

where:

$$X = A - D(C_1 + C_2 + C_3) + LH_5$$
$$-F(1)\begin{bmatrix} H_6 + B_3 - D(1-y_1) + L\left(\dfrac{{y_1}^2-y_1}{2}\right) \\ -F(1)\left(\dfrac{-{y_1}^3+3{y_1}^2-2y_1}{6}\right) \end{bmatrix} \tag{3.96}$$

$$Y = H_1 + H_3 + H_6 - B_1 - B_2 + B_3 - D(1-2y_1) + L\left(\frac{{y_1}^2-y_1}{2}\right) - F(1)\left(\frac{-{y_1}^3+3{y_1}^2-2y_1}{3}\right) \tag{3.97}$$

$$Z = H_2 + H_4 + H_5 - F(1)\left(\frac{{y_1}^2-y_1}{2}\right) \tag{3.98}$$

with:

$$A = \int_0^1 F(y)G(y)dy;\ B_1 = \int_0^{y_0} G(y)dy;\ B_2 = \int_{y_0}^{y_1} G(y)dy;$$
$$B_3 = \int_{y_1}^1 G(y)dy;\ C_1 = \int_0^{y_0} F(y)dy;\ C_2 = \int_{y_0}^{y_1} F(y)dy;$$
$$C_3 = \int_{y_1}^1 F(y)dy;\ D = \int_0^1 G(y)dy;\ H_1 = \int_0^{y_0} \left(\frac{1}{6} - \frac{y^2}{2}\right) F(y)dy;$$
$$H_2 = \int_0^{y_0} \left(\frac{1}{2} - y\right) F(y)dy;\ H_3 = \int_{y_0}^{y_1} \left(\frac{1}{6} - \frac{y^2}{2}\right) F(y)dy;$$
$$H_4 = \int_{y_0}^{y_1} \left(\frac{1}{2} - y\right) F(y)dy;\ H_5 = \int_{y_1}^1 \left(\frac{1}{2} - y\right) F(y)dy;$$
$$H_6 = \int_{y_1}^1 \left(\frac{3y^2 - 6y + 2}{6}\right) F(y)dy \text{ and } L = \int_0^1 F(y)dy \tag{3.99}$$

Finally, with $E = C_T + NC_S$, Eq. (3.79) leads to the following transcendental equation:

$$Le^2X^2R^{n+4}\left(\psi_c + \frac{Pe}{2}\right)^{n+4} + 2Le^2PeXYR^{n+3}\left(\psi_c + \frac{Pe}{2}\right)^{n+3}$$
$$+\left(-X(1+Le^2) + Le^2Pe^2Y^2 + 2Le^2Pe^2X\left(\frac{{y_1}^2 - y_1}{2}\right)\right)R^{n+2}\left(\psi_c + \frac{Pe}{2}\right)^{n+2}$$
$$+\left(2Le^2Pe^3Y\left(\frac{{y_1}^2 - y_1}{2}\right) - (1+Le^2)PeY\right)R^{n+1}\left(\psi_c + \frac{Pe}{2}\right)^{n+1}$$
$$+\left(Le^2Pe^4\left(\frac{{y_1}^2 - y_1}{2}\right)^2 - (1+Le^2)Pe^2\left(\frac{{y_1}^2 - y_1}{2}\right) + 1\right)R^n\left(\psi_c + \frac{Pe}{2}\right)^n$$
$$+ Ra_T(bLe^2 + dNLe)XZR^3\left(\psi_c + \frac{Pe}{2}\right)^3$$
$$-Ra_T\begin{bmatrix}\left(\left(a - bPe({y_1}^2 - y_1)\right)Le^2 + N\left(c - dLePe({y_1}^2 - y_1)\right)\right)X \\ -(bLe^2 + dNLe)PeYZ\end{bmatrix}R^2\left(\psi_c + \frac{Pe}{2}\right)^2$$
$$-Ra_T\begin{bmatrix}\left(\left(a - bPe({y_1}^2 - y_1)\right)Le^2 + N\left(c - dLePe({y_1}^2 - y_1)\right)\right)PeY \\ -(bLe^2 + dNLe)Pe^2\left(\frac{{y_1}^2 - y_1}{2}\right)Z + (b + dNLe)Z\end{bmatrix}R\left(\psi_c + \frac{Pe}{2}\right)$$
$$-Ra_T\left[\left(a - bPe({y_1}^2 - y_1)\right)Le^2 + N\left(c - dLePe({y_1}^2 - y_1)\right)\right]Pe^2\left(\frac{{y_1}^2 - y_1}{2}\right)$$
$$+Ra_T\left[\left(a - bPe({y_1}^2 - y_1)\right) + N\left(c - dLePe({y_1}^2 - y_1)\right)\right] = 0 \tag{3.100}$$

Coefficients $A, B_1, B_2, B_3, C_1, C_2, C_3, D, H_1, H_2, H_3, H_4, H_5, H_6, L, R,$ and $F(1)$ from equations (3.77), (3.80), and (3.99) which depend on the governing parameters $Pe, Ra_T, Le, N,$ and n are computed using the Gauss–Legendre integration method.

Newton-Raphson method is used to solve Eq. (3.100), the resulting ψ_c value is then used to calculate C_T and C_S values using Eqs. (3.94) and (3.95), respectively, for given values of $Pe,\ Ra_T, Le,\ N,$ and n.

3.4.3 Heat and mass transfer

For Nusselt and Sherwood numbers, and while considering Eqs. (3.29) – (3.36), simplifications in Eq. (3.53), and the centro-symmetric nature of the problem, their expressions are simplified as follows:

$$Nu_h = \frac{-a}{C_T} = \overline{Nu_h};\ Sh_h = \frac{-c}{C_S} = \overline{Sh_h} \tag{3.101}$$

$$Nu_v = \frac{b}{2\theta_T(0)} = \overline{Nu_v};\ Sh_v = \frac{d}{2\theta_S(0)} = \overline{Sh_v} \tag{3.102}$$

with:

$$\theta_T(0) = -C_T R\left(\psi_c + \frac{Pe}{2}\right) D + C_T \frac{Pe}{6} + \frac{b}{2} \tag{3.103}$$

$$\theta_S(0) = -LeC_S R\left(\psi_c + \frac{Pe}{2}\right) D + LeC_S \frac{Pe}{6} + \frac{d}{2} \tag{3.104}$$

We note that heat and mass transfer rates in the horizontal direction are related by the following equation:

$$\overline{Sh_h} = Le^2(\overline{Nu_h} - 1) + 1 \tag{3.105}$$

which can be verified numerically in the next two chapters.

3.4.4 Pure forced and pure natural convection

On the one hand, pure forced convective regime is obtained by setting $Ra_T = 0$, where the convection is driven by shear force only. On the other hand, the results for pure natural convection are obtained by considering a new cavity configuration with motionless walls ($u' = 0$ for $y' = 0$ and $y' = H'$). The governing equations are given by (3.17) – (3.21) with dimensionless dynamic boundary conditions

$(u(0) = u(1) = 0)$. Following the same procedure as before, the parallel flow approximation results in the following expressions:

$$C_T = \frac{a - bR\psi_c B}{R^2 {\psi_c}^2 A - 1} \tag{3.106}$$

$$C_S = \frac{c - LeR\psi_c B}{Le^2 R^2 {\psi_c}^2 A - 1} \tag{3.107}$$

with:

$$B = \int_0^1 \left(\frac{1}{2} - y\right) F(y) dy \text{ and } \psi_c = \frac{E^{1/n} {Ra_T}^{1/n}}{R} \tag{3.108}$$

The ensuing transcendental equation is written as follows:

$$\begin{aligned} &Le^2 A^2 R^{n+4} {\psi_c}^{n+4} - (1 + Le^2) A R^{n+2} {\psi_c}^{n+2} + R^n {\psi_c}^n \\ &+ Ra_T (bLe^2 + dNLe) ABR^3 {\psi_c}^3 - Ra_T (aLe^2 + cN) AR^2 {\psi_c}^2 \\ &- Ra_T (b + dNLe) BR\psi_c + Ra_T (\mathrm{a} + \mathrm{c}N) = 0 \end{aligned} \tag{3.109}$$

Nusselt and Sherwood numbers are computed using Eqs. (3.101) and (3.102).

3.4.5 Single lid-driven cavities

As mentioned before, the introduction of characteristic coordinates y_0 and y_1 is due to the sign change of du/dy and the nonlinear nature of governing equation (3.54) making a direct integration impossible. The values of y_0 and y_1 are computed by injecting equations (3.81), (3.84), and (3.87) in the return flow condition (3.60) and exploiting the centro-symmetric nature of the flow expressed by:

$$y_0 + y_1 = 1 \tag{3.110}$$

which is true for problems with symmetrical boundary conditions. Therefore, for single lid-driven cavities $(e = 0)$, Eq. (3.110) is no longer valid and an additional equation is needed to analytically solve the problem for non-Newtonian fluid flows described by Eq. (3.54). However, for a Newtonian fluid $(n = 1)$, Eq. (3.54) becomes:

$$\frac{\mathrm{d}^3 u(y)}{\mathrm{d}y^3} = ERa_T \tag{3.111}$$

As a result, and given the linear nature of governing equations (3.111), (3.55), and (3.56), the aforementioned limitation is removed and the integration of the equations is straightforward:

$$u(y) = \frac{Ra_T E}{12}(2y^3 - 3y^2 + y) + Pe(3y^2 - 2y) - ePe(3y^2 - 4y + 1) \tag{3.112}$$

$$\theta_T(y) = \frac{C_T Ra_T E}{1440}(12y^5 - 30y^4 + 20y^3 - 1) + \frac{C_T Pe}{60}[(15y^4 - 20y^3 + 2) - e(15y^4 - 40y^3 + 30y^2 - 3)] - b(y - \frac{1}{2}) \tag{3.113}$$

$$\theta_S(y) = \frac{LeC_S Ra_T E}{1440}(12y^5 - 30y^4 + 20y^3 - 1) + \frac{LeC_S Pe}{60}[(15y^4 - 20y^3 + 2) - e(15y^4 - 40y^3 + 30y^2 - 3)] - d(y - \frac{1}{2}) \tag{3.114}$$

Following the same steps as before, we find:

$$\psi(y) = \frac{Ra_T}{24} E\left(y^4 - 2y^3 + y^2\right) + Pe(y^3 - y^2) - ePe(y^3 - 2y^2 + y) \tag{3.115}$$

$$C_T = \frac{a + \frac{b}{12}\left(-\frac{Ra_T}{60}E + Pe(1+e)\right)}{-\frac{Ra_T^2}{362{,}880}E^2 + \frac{Ra_T Pe}{3360}(1+e)E - \frac{Pe^2}{210}(2e^2+3e+2) - 1} \tag{3.116}$$

$$C_S = \frac{c + \frac{dLe}{12}\left(-\frac{Ra_T}{60}E + Pe(1+e)\right)}{-\frac{Le^2 Ra_T^2}{362{,}880}E^2 + \frac{Le^2 Ra_T Pe}{3360}(1+e)E - \frac{Le^2 Pe^2}{210}(2e^2+3e+2) - 1} \tag{3.117}$$

where the following transcendental equation is obtained:

$$\frac{Le^2 Ra_T^4}{362{,}880^2}E^5 - \frac{Le^2 Ra_T^3 Pe}{609{,}638{,}400}(1+e)E^4 + Ra_T^2\left[\frac{Le^2 Pe^2}{38{,}102{,}400}(2e^2+3e+2) + \frac{(1+Le^2)}{362{,}880} + \frac{Le^2 Pe^2}{11{,}289{,}600}(1+e)^2 - \frac{Ra_T}{261{,}273{,}600}(bLe^2 + NdLe)\right]E^3 + Ra_T\left[-\frac{Le^2 Pe^3}{352{,}800}(1+e)(2e^2 + 3e + 2) - \frac{Pe(1+Le^2)}{3360}(1+e) + \frac{Ra_T}{362{,}880}(aLe^2 + Nc) + \left(\frac{Ra_T}{2{,}419{,}200} + \frac{Ra_T}{4{,}354{,}560}\right)Pe(bLe^2 + NdLe)(1+e)\right]E^2 + \left[\frac{Le^2 Pe^4}{44{,}100}(2e^2+3e+2)^2 + \frac{Pe^2(1+Le^2)}{210}(2e^2+3e+2) - \frac{Ra_T Pe}{3360}(aLe^2 + Nc)(1+e) - \frac{bRa_T}{720}\left(\frac{Le^2 Pe^2}{210}(2e^2+3e+2) + 1\right) - \frac{NdLeRa_T}{720}\left(\frac{Pe^2}{210}(2e^2+3e+2) + 1\right) - \frac{Ra_T Pe^2}{40{,}320}(bLe^2 + NdLe)(1+e)^2 + 1\right]E + \left[Le^2\left(a + \frac{bPe}{12}(1+e)\right) + N\left(c + \frac{dLePe}{12}(1+e)\right)\right]\frac{Pe^2}{210}(2e^2+3e+2) + a + \frac{bPe}{12}(1+e) + N\left(c + \frac{dLePe}{12}(1+e)\right) = 0 \tag{3.118}$$

Mean Nusselt and Sherwood numbers are computed using Eqs. (3.101) and (3.102).

For pure natural convection regime:

$$C_T = -\frac{\left(a-\frac{bRa_T}{720}E\right)}{\frac{Ra_T^2}{362{,}880}E^2+1} \tag{3.119}$$

$$C_S = -\frac{\left(c-\frac{dLeRa_T}{720}E\right)}{\frac{Le^2Ra_T^2}{362{,}880}E^2+1} \tag{3.120}$$

and the resulting transcendent equation is:

$$\frac{Le^2Ra_T^4}{362{,}880^2}E^5 + Ra_T^2\left[\frac{\left(1+Le^2\right)}{362{,}880} - \frac{Ra_T}{261{,}273{,}600}(bLe^2+NdLe)\right]E^3 + \left[\frac{Ra_T^2}{362{,}880}(aLe^2 + Nc)\right]E^2 + \left[-\frac{bRa_T}{720} - \frac{NdLeRa_T}{720} + 1\right]E + \mathrm{a} + Nc += 0 \tag{3.121}$$

As for pure forced convection, we get the following expressions:

$$C_T = -\frac{\left(a+\frac{bPe}{12}(1+e)\right)}{\frac{Pe^2}{210}(2e^2+3e+2)+1} \tag{3.122}$$

$$C_S = -\frac{\left(c+\frac{dLePe}{12}(1+e)\right)}{\frac{Le^2Pe^2}{210}(2e^2+3e+2)+1} \tag{3.123}$$

with the transcendent equation:

$$\left[\frac{Le^2Pe^4}{44{,}100}(2e^2+3e+2)^2 + \frac{Pe^2(1+Le^2)}{210}(2e^2+3e+2)+1\right]E + \left[Le^2\left(a+\frac{bPe}{12}(1+e)\right) + N\left(c+\frac{dLePe}{12}(1+e)\right)\right]\frac{Pe^2}{210}(2e^2+3e+2) + a + \frac{bPe}{12}(1+e) + N\left(c+\frac{dLePe}{12}(1+e)\right) = 0 \tag{3.124}$$

CHAPTER 4 Double-Diffusive Mixed Convection in a Single Lid-Driven Cavity Filled with Newtonian Fluid

4.1 Introduction

In this chapter we consider a horizontal rectangular cavity (Fig. 4.1) filled with Newtonian fluid and submitted to uniform heat and mass fluxes along the vertical walls while the horizontal ones are insulated and impermeable to mass transfer ($a = c = 1$ and $b = d = 0$). The cavity top wall slides from left to right (i.e., acting in the same direction as imposed heat and mass fluxes) with a constant velocity u_0'; while the remaining walls are motionless ($e = 0$). Double-diffusive mixed convection in the described configuration is investigated numerically and analytically. To better understand convection phenomena, the dominance regions of convective regimes, namely natural, mixed, and forced convection are defined. Next, the effects of governing parameters on flow structure and heat and mass transfer are illustrated and amply discussed for each regime in terms of stream function ψ, average horizontal Nusselt number $\overline{Nu_h}$, average horizontal Sherwood number $\overline{Sh_h}$, streamlines, isotherms, and iso-concentrations along with velocity, temperature, and concentration profiles. The numerical results presented in this chapter and the next two chapters are obtained using finite volume method.

4.2 Effect of Prandtl number

The generalized Prandtl number expressed in Eq. (3.26) is not a fluid property alone given its dependence on H' and n; however, the parameter reduces to conventional Pr for a Newtonian fluid ($n = 1$). For the present study, almost all fluids of interest have a Pr value much larger than unity. Conducted Numerical tests show that for $Pr \geq 10$, increasing Prandtl number does not affect fluid flow and heat and mass transfer. Such result can be confirmed while referring to governing equations (3.18) and (3.19), where increasing Prandtl number results in diminishing the convective terms (terms on the left-hand side of the equations) compared to the diffusive terms (terms on the right-hand side of the equations). Another confirmation of this finding is that the analytical

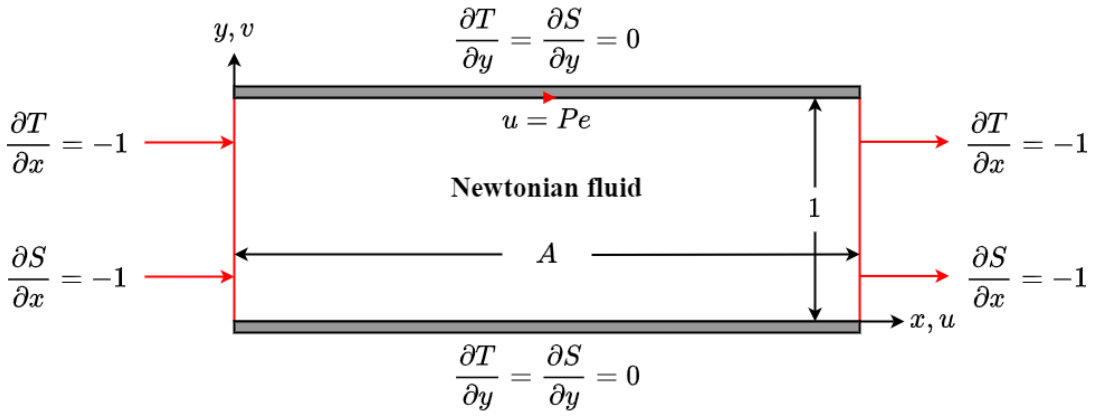

Figure 4.1. Geometry of the investigated configuration along with coordinate system and associated boundary conditions. The vertical walls are submitted to uniform density of heat and mass fluxes, while the horizontal ones are insulated and impermeable. The top wall slides continuously from left to right with a constant velocity, while the remaining boundaries are motionless.

solution, established in the previous chapter, is independent of Pr. Similar conclusions about the asymptotic value of Prandtl number are reported in previously published works [92-94].

4.3 Numerical code validation

The present finite volume numerical code is verified using benchmark results from the literature to assess its accuracy. Table 4.1 compares the obtained results with previously published studies on mixed convection inside a lid-driven cavity. The good agreement is obvious in terms of the computed average Nusselt number; thus, confirm the capability of our numerical method to accurately model mixed convection within lid-driven cavities.

4.4 Mesh size choice

The choice of the grid size is made based on numerical trail-and error tests as to get the best tradeoff between solutions accuracy and convergence time. Table 4.2 shows that for $A = 24$ (the reasons for choosing this value for the cavity aspect ratio will be discussed later), a uniform grid size of 341×81 is found sufficient to accurately simulate fluids' flow and temperature and concentration distributions within the cavity.

Table 4.1 – Comparison of average Nusselt number with published results in the literature for a lid-driven enclosure with $Gr = 100, Pr = 0.71$, and different values of Re.

Re	Present work	Ref. [71]	Ref. [36]	Ref. [37]	Ref. [40]	Ref. [41]	Ref. [42]
1	1.0073	1.0094	1.00033	-	-	-	-
100	2.0534	2.09	2.03116	1.94	2.10	1.985	2.01
400	4.1273	4.08082	4.0246	3.84	3.85	3.8785	3.91
1000	6.7267	6.54687	6.48423	6.33	6.33	6.345	6.33

Table 4.2 – Convergence tests using $\overline{Nu_h}$ for $A = 24, Ra_T = 10^5, Le = 5, N = 1$, and different values of Pe in a single lid-driven cavity.

Pe	Grids					Analytical Solution
	(301,81)	(321,81)	(341,81)	(341,121)	(361,81)	
0.1	31.601	31.658	31.689	31.660	31.722	31.401
1.0	31.909	31.968	32.000	31.967	32.033	31.706
5.0	33.343	33.408	33.444	33.418	33.479	33.131
25.0	42.4	42.506	42.572	42.555	42.633	42.143
50.0	59.638	59.839	59.977	59.942	60.096	59.364
100.0	123.072	123.711	124.197	124.133	124.597	123.308
150.0	233.249	234.808	236.045	235.906	237.045	235.538

4.5 Value of A satisfying the large aspect ratio approximation

In order for numerical results to be in agreement with analytical ones, and given that the parallel flow approximation is valid for shallow enclosures $A >> 1$, we need to define the value of aspect ratio A after which the flow characteristics computed numerically are invariant to A. Figure 4.2 illustrates the variation of $\overline{Nu_h}$ with A for $Ra_T = 10^5,\ Le = 5,\ N = 1$ and several values of Pe. The heat transfer rate reaches an asymptotic state as the aspect ratio keeps increasing, we also detect the forced regime

($Pe = 200$) retarding role as it delays the reach of such asymptotic state compared to natural regime. The figure shows that $A = 24$ is the smallest value that leads to numerical results independent of the aspect ratio and in good agreement with analytical results, and that for different values of governing parameters. Mamou et al. [95] showed that such findings can be generalized to a wide range of Le and N values. Furthermore, Table 4.2 shows a perfect agreement between analytical and numerical results which validates both the analytical approach and the numerical code and justifies the choice of $A = 24$ as an asymptotic value. Further confirmation of such facts for a wide range of governing parameters can be gained from comparing numerical and analytical curves portrayed below.

Accordingly, Newtonian double-diffusive mixed convection in shallow rectangular cavities is mainly governed by: Péclet number Pe, thermal Rayleigh number Ra_T, Lewis number Le, and buoyancy ratio N. In this chapter, the effects of said parameters on fluids' flow and heat and mass transport phenomena are investigated in details for three separate convective regimes: natural, mixed, and forced convection.

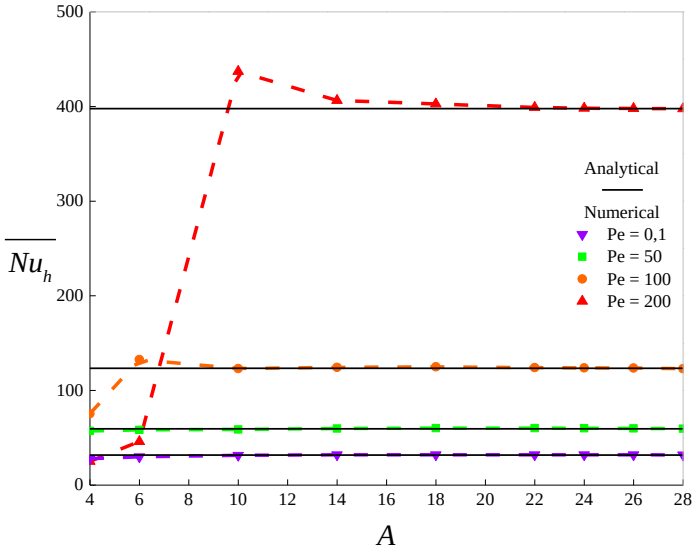

Figure 4.2. Evolution of numerical average horizontal Nusselt number ($\overline{Nu_h}$) with the cavity aspect ratio $\left(A = \frac{L'}{H'}\right)$ for $Ra_T = 10^5, Le = 5, N = 1$, and different Pe values in a single lid-driven enclosure.

4.6 Mixed convection parameter

The modified Richardson number Gr/Re^{γ} (otherwise called the mixed convection parameter with $Pe = RePr$ and $Ra_T = GrPr$) compares the effect of buoyancy forces generated by applied heat and mass fluxes to that of shear force induced by sliding walls on the convective regime. Thus, compares the strengths of natural and forced convection and allows us to separate three convective regimes. First, dominant natural convection regime characterized by strong buoyancy force and insignificant contribution of shear force to the overall convective regime. Second, mixed convection regime with buoyancy force and shear force are of comparable magnitudes as both contribute to the overall convection. Third, dominant forced regime where shear force dominates buoyancy effect. The exponent γ depends on the working fluid nature, the enclosure geometry, and the associated thermal and solutal boundary conditions.

The separation of convective regimes is crucial when investigating mixed convection as it offers a better understanding of different convection phenomena and sets boundaries for each regime in terms of the governing parameters. Clearly the governing equations do not specify any physical boundaries that separate the three convective regimes, making the procedure purely numerical where a practically suitable threshold needs to be defined to separate natural, mixed, and forced regimes. Based on the assumptions above, a threshold of 5% is chosen. If heat and mass transfer rates deviate from the values computed in the case of pure natural or pure forced regime by less than 5%, the regime is flagged as dominant natural or dominant forced regime, respectively, if not the regime is considered mixed.

For the purpose of focusing on the effect of mixed convection parameter alone, we set $Le = 1$. In this case, the temperature and concentration have similar diffusion characteristics, meaning that the computed deviations from the pure regimes' values will be the same as $\overline{Nu_h} = \overline{Sh_h}$. Accordingly, the following ratios are used to define the mixed convection parameter:

$$\varepsilon_{Nu_{h,n}} = \frac{|\overline{Nu_h} - \overline{Nu_{h,n}}|}{\overline{Nu_{h,n}}} \; ; \qquad \varepsilon_{Nu_{h,f}} = \frac{|\overline{Nu_h} - \overline{Nu_{h,f}}|}{\overline{Nu_{h,f}}} \tag{4.1}$$

with $\overline{Nu_{h,n}}$ and $\overline{Nu_{h,f}}$ are the average horizontal Nusselt numbers for pure natural and pure forced convections, respectively. The regime is designated as dominant natural

convection for $\varepsilon_{Nu_{h,n}} < 5\%$, while the regime is qualified as dominant forced convection for $\varepsilon_{Nu_{h,f}} < 5\%$. Otherwise, the regime is flagged as mixed convection.

Figure 4.3 is drawn with points $\left(log\ (Ra_T), log(Pe)\right)$ that verify $\varepsilon_{Nu_{h,n}} = 5\%$ and $\varepsilon_{Nu_{h,f}} = 5\%$ obtained analytically (solid lines) and numerically (symbols). A good agreement can be seen between both solutions where two parallel straight lines split the domain defined with Ra_T and Pe values into three separate regions. The region on the left of line (1) corresponds to dominant natural convection ($\varepsilon_{Nu_{h,n}} < 5\%$) . The second region on the right of line (2) corresponds to dominant forced convection ($\varepsilon_{Nu_{h,f}} < 5\%$). The third region, enclosed by lines (1) and (2), exhibits a mixed convection regime. Lines (1) and (2) can be correlated in the form of mixed convection parameter as follows:

$$\frac{Ra_T}{Pe^{3.0}} = \eta_n \text{ and } \frac{Ra_T}{Pe^{3.0}} = \eta_f \tag{4.2}$$

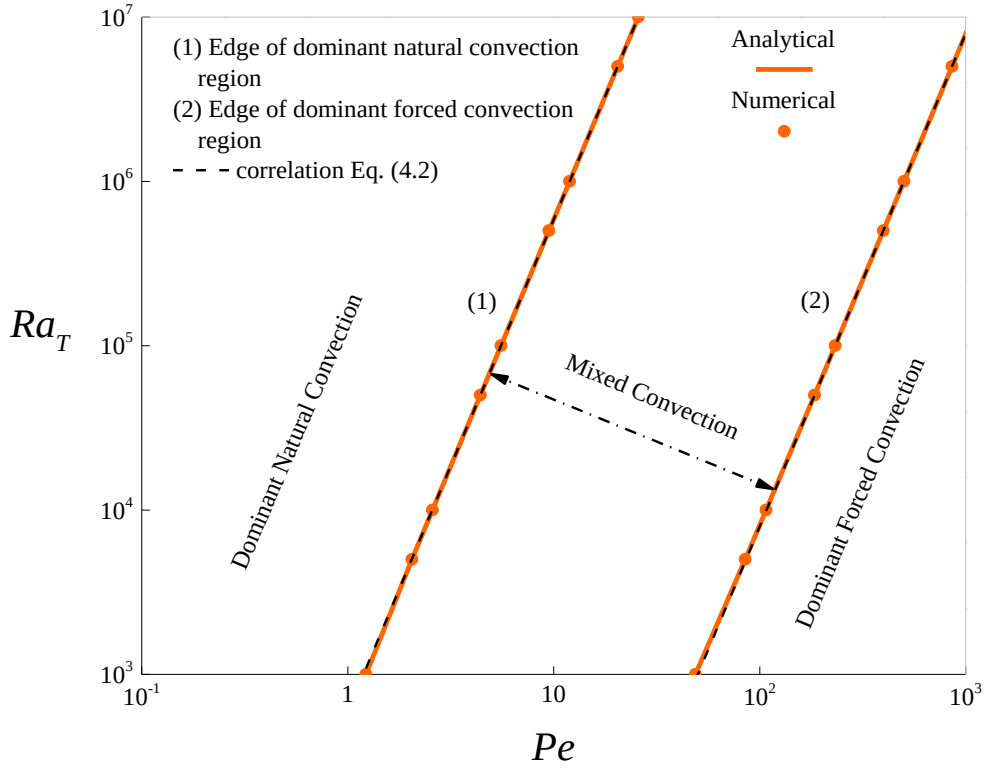

Figure 4.3. Natural, forced, and mixed convection dominance regions for $Le = 1$ and $N = 1$ inside a single lid-driven rectangular cavity.

outlining dominant natural and dominant forced convective regime limits, respectively. The values of coefficients η_n and η_f are presented in Table 4.3 and shown in Figure 4.3 with dashed lines.

Finally, for the considered cavity configuration, the associated boundary conditions, and for $Le = 1$ and $N = 1$, the mixed convection regime is delimited as follows:

$$0.0079 < \frac{Ra_T}{Pe^{3.0}} < 584.83 \tag{4.3}$$

4.7 Dynamical, thermal, and solutal structures

Streamlines (top), isotherms (middle), and iso-concentrations (bottom) are shown in Figure 4.4 for $Ra_T = 10^5,\ Le = 5,\ N = 1$, and various values of Pe. As the wall is sliding from left to right in the same direction as the imposed temperature and concentrations gradients, the buoyancy and shear effects work together (assisting flow) causing the flow to be unicellular and clockwise. Plus, except for the edges of the cavity near the vertical walls where the flow experiences a rotation of 180°, fluid flow parallel to the horizontal direction while the thermal and solutale fields are linearly stratified in the x-direction.

For low values of Pe (i.e., $\frac{Ra_T}{Pe^{3.0}} > \eta_n$), dynamical, thermal, and solutale fields are similar to the ones obtained in pure natural convection case (Figure 4.5), where the dynamical field is Centro-symmetric with horizontal parallelism while isotherms and iso-concentrations display stratification in the core region of the enclosure. Thus, confirming that buoyancy force dominates the shear one. As Pe increases, streamlines, isotherms, and iso-concentrations become more sensitive to the effect of the moving wall since the Centro-symmetric pattern starts to disappear and the inclinations of the isotherms and iso-concentrations with respect to the y-direction increases. For large

Table 4.3 – Correlation coefficients η_n and η_f.

Convection regime	**Natural convection η_n**	**Forced convection η_f**
	584.83	0.0079

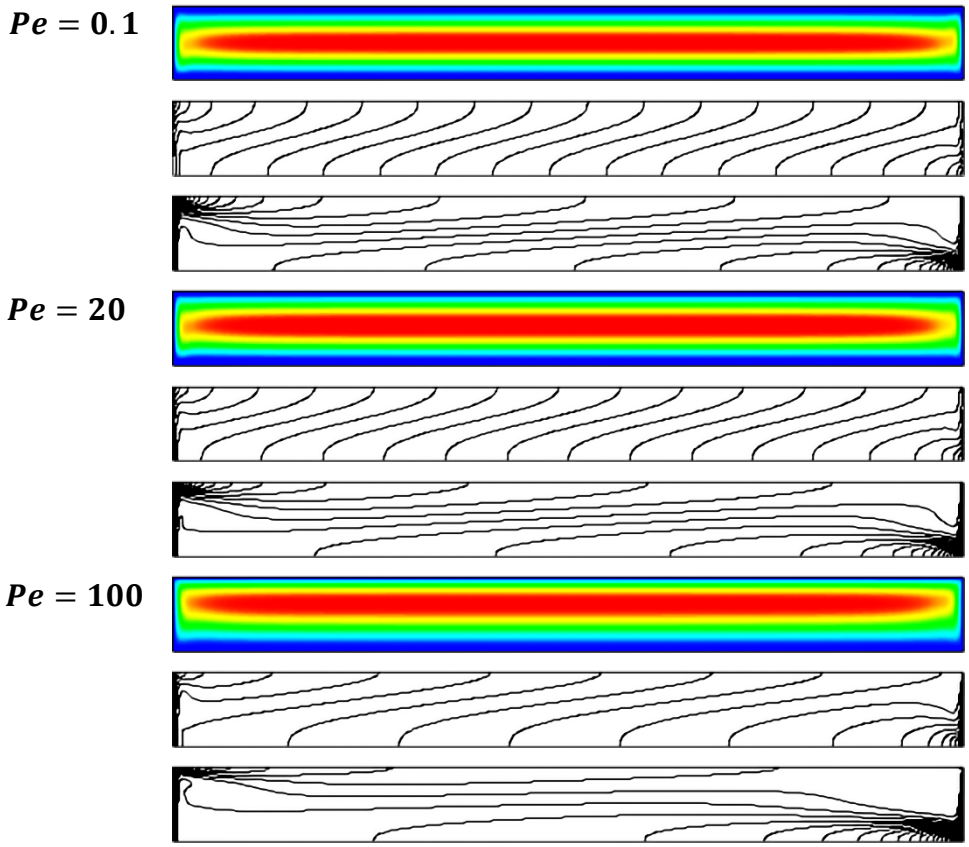

Figure 4.4. Streamlines (top), isotherms (middle), and iso-concentrations (bottom) for $A = 24, Ra_T = 10^5, Le = 5$ and $N = 1$ while varying Péclet number to account for the different convective regimes (natural, mixed, and forced convection) inside a single lid-driven cavity. (Scale not respected).

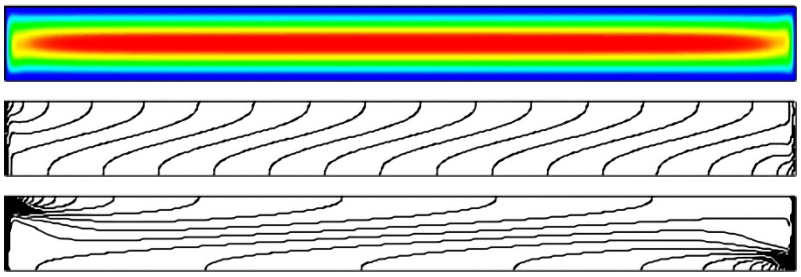

Figure 4.5. Streamlines (top), isotherms (middle), and iso-concentrations (bottom) for pure natural convection at $A = 24,\ Ra_T = 10^5, Le = 5,$ and $N = 1$ inside a single lid-driven cavity. (Scale not respected).

enough Pe values (i.e., $\frac{Ra_T}{Pe^{3.0}} < \eta_f$), we end up with patterns similar to the ones found in pure forced convection for $Pe = 100$ and $Pe = 200$ (Figure 4.6) where the streamlines are more packed near the top moving wall showing that the flow is powerful in that region, while isotherms and iso-concentrations become more tilted and practically linear in the center of the cavity. In this case it is obvious that the sliding wall' shear force dominates the convection.

It's worth to note that as Pe increases, a boundary layer of isotherms and iso-concentrations starts to form near the vertical walls, indicating that heat and mass transfer strengthen in the region. The layer is more noticeable near the left wall.

4.8 Effect of Péclet number

The evolutions of $|\psi_c|$, $\overline{Nu_h}$, and $\overline{Sh_h}$ with Péclet number Pe are presented in Figure 4.7 for $Le = 5, N = 1$, and different values of Ra_T. For low values of Pe, flow characteristics are invariant to Pe while depending on Ra_T, plus the results match the ones obtained in the case of pure natural convection regime indicating that fluid flow and heat and mass transfer are mainly assured by natural convection. After a given value of Pe, $|\psi_c|$, $\overline{Nu_h}$, and $\overline{Sh_h}$ start to increase slowly due to the contribution of shear

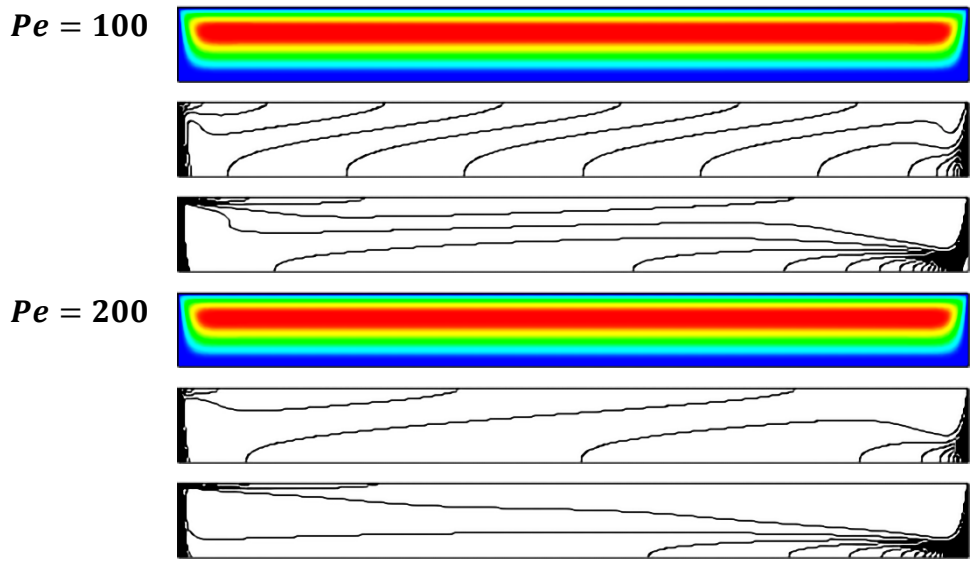

Figure 4.6. Streamlines (top), isotherms (middle), and iso-concentrations (bottom) for pure forced convection $(Ra_T = 0)$ at $A = 24, Le = 5, N = 1$ and different Pe values inside a single lid-driven cavity. (Scale not respected).

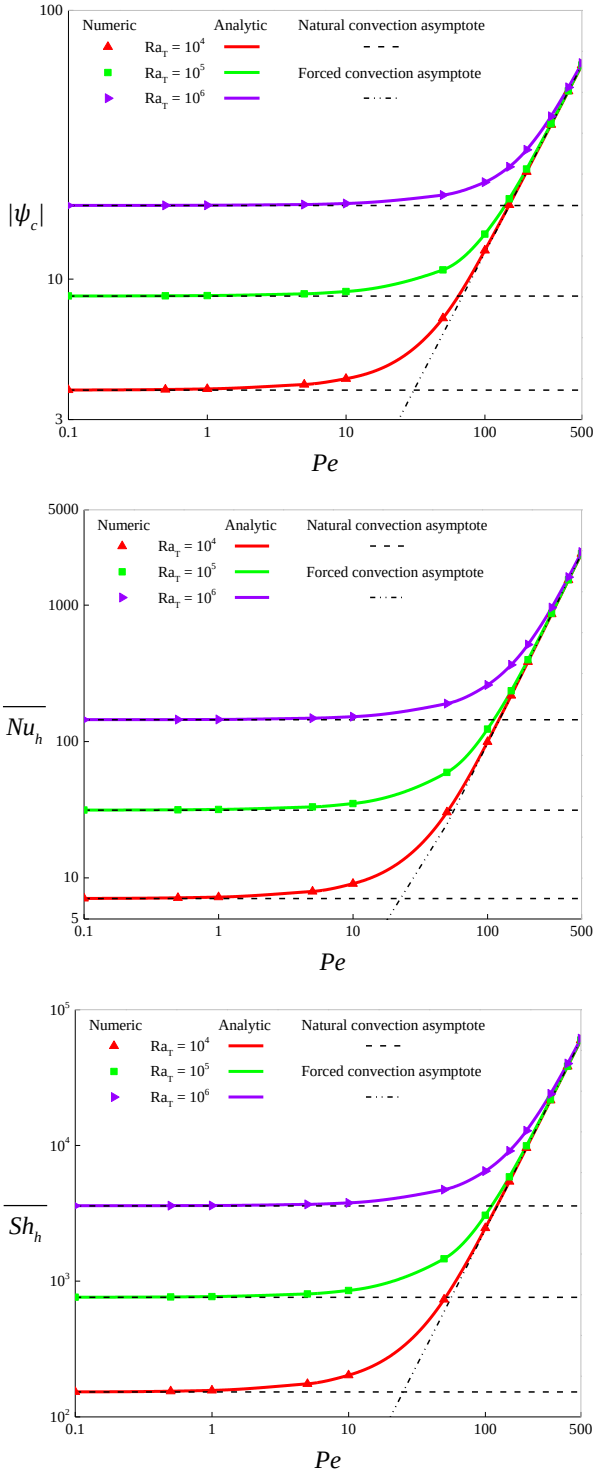

Figure 4.7. Evolutions of the stream function at the center of the cavity $\left(x = \frac{A}{2},\ y = 1/2\right)$ (top), horizontal Nusselt number (middle), and horizontal Sherwood number (bottom) with Péclet number (Pe) for $Le = 5, N = 1$, and different values of Ra_T inside a single lid-driven cavity.

effect generated by the moving wall. The said value of Péclet number can be correlated by $\left(\frac{Ra_T}{\eta_n}\right)^{\frac{1}{3.0}}$, where it increases as Ra_T increases owing to the well-established effect of thermal Rayleigh number in reinforcing natural convection; thus, delaying the transition from natural regime to mixed one. Finally, as Pe keeps increasing, the shear effect dominates the buoyancy one and flow characteristics increase linearly with Pe indicating a dominant forced convection $\left(\frac{Ra_T}{Pe^{3.0}} < \eta_f\right)$. Such fact can be further confirmed as the results agree with the ones obtained for pure forced convection.

Pure natural convection results are given by Eqs. (4.4) and (4.5) for $\overline{Nu_h}$ and $\overline{Sh_h}$, respectively. For pure forced convection regime, the results are defined by Eqs. (4.6) and (4.7) for $\overline{Nu_h}$ and $\overline{Sh_h}$, respectively. These results are shown in Figure 4.7 as dashed lines.

$$\overline{Nu_{h,n}} = \frac{Ra_T^2}{362{,}880}E^2 + 1 \tag{4.4}$$

$$\overline{Sh_{h,n}} = \frac{Le^2 Ra_T^2}{362{,}880}E^2 + 1 \tag{4.5}$$

$$\overline{Nu_{h,f}} = \frac{Pe^2}{105} + 1 \tag{4.6}$$

$$\overline{Sh_{h,f}} = \frac{Le^2 Pe^2}{105} + 1 \tag{4.7}$$

4.9 Effect of thermal Rayleigh number

To further illustrate the influence of thermal Rayleigh number Ra_T, the variations of $|\psi_c|$, $\overline{Nu_h}$, and $\overline{Sh_h}$ as a function of Ra_T are depicted in Figure 4.8 for $Le = 5$, $N = 1$, and various values of Pe. The evolution patterns of $|\psi_c|$, $\overline{Nu_h}$, and $\overline{Sh_h}$ are similar to those with Péclet number discussed above considering buoyancy effect and shear force respective magnitudes. For small values of Ra_T, flow characteristics are invariant as forced convection dominates (results agree with the ones obtained for pure forced convection regime), where increasing Pe increases the extent of the invariability range as it strengthens the shear effect. After which they first experience a slight

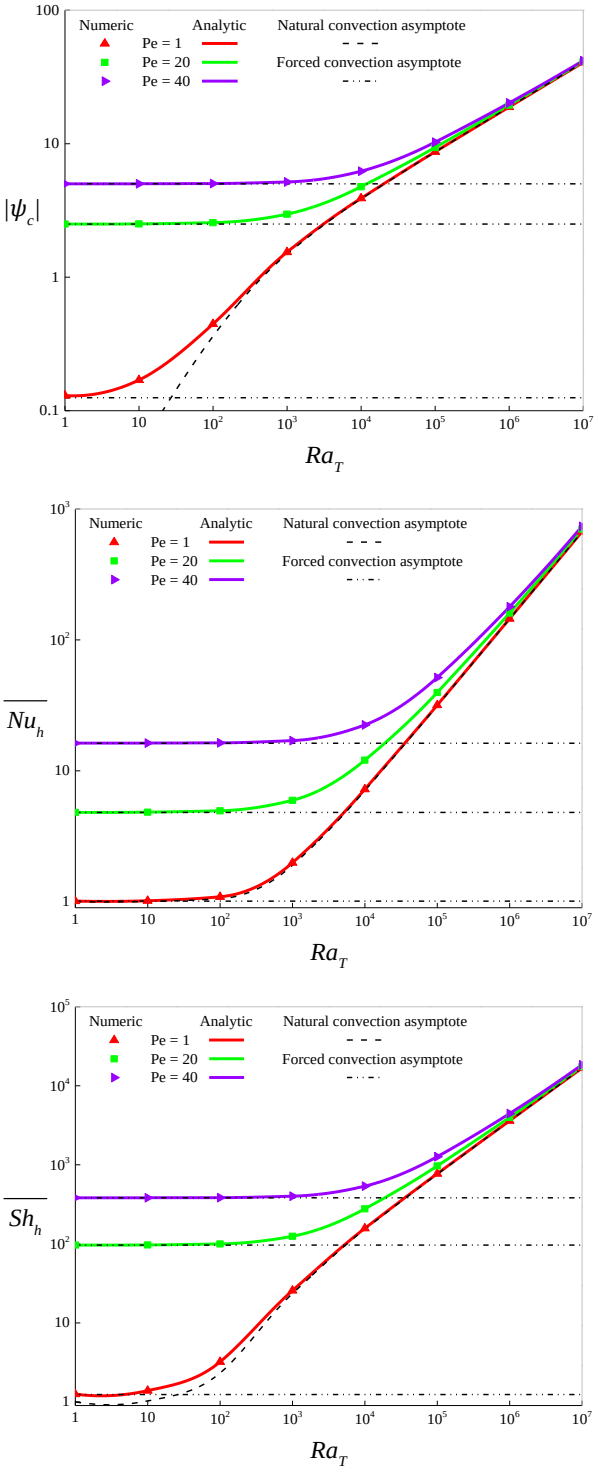

Figure 4.8. Evolutions of the stream function at the center of the cavity $\left(x = \frac{A}{2},\ y = \frac{1}{2}\right)$ (top), horizontal Nusselt number (middle), and horizontal Sherwood number (bottom) with thermal Rayleigh number (Ra_T) for $Le = 5, N = 1$, and different values of Pe inside a single lid-driven cavity.

increase (mixed convection regime), the threshold signaling this change in behavior is defined by ($Pe^{3.0}\eta_f$) where forced convection no longer dominates fluid flow and heat and mass transfer, which agrees with the mixed convection regime limits given by Eq. (4.3). Next, after the transition phase, all quantities increase monotonically (dominating natural convection for $\frac{Ra_T}{Pe^{3.0}} > \eta_n$) due to the role of enhancing buoyancy force in promoting convection. The dashed lines describing pure forced convection results are defined by Eqs. (4.6) and (4.7) for $\overline{Nu_h}$ and $\overline{Sh_h}$, respectively. As for pure natural convection, asymptotic limits of the results are defined by Eqs. (4.4) and (4.5) for $\overline{Nu_h}$ and $\overline{Sh_h}$, respectively.

There are two points that deserve mentioning. First, for low values of Pe ($Pe \leq 1$) and when Ra_T is small enough ($Ra_T < 10$), fluid flow and heat and mass transfer are governed by diffusion ($|\psi_c| \leq 10^{-1}$, $\overline{Nu_h} \approx 1$, and $1 < \overline{Sh_h} < 2$). Outside this zone, increasing Ra_T results in increasing $|\psi_c|$ and $\overline{Sh_h}$ without affecting $\overline{Nu_h}$ at first, which increases only when $Ra_T \geq 100$. Second, because $Le = 5$, mass transfer is more important than heat transfer.

4.10 Effect of Lewis number

Variations of $|\psi_c|$, $\overline{Nu_h}$, and $\overline{Sh_h}$ with Lewis number Le are reported in Figure 4.9 for $Ra_T = 10^5, N = 1$, and different values of Pe. For low values of Le, the upper plateaus for $|\psi_c|$ and $\overline{Nu_h}$ indicate that thermal convection dominates thermal conduction, while the lower plateau characterized by $\overline{Sh_h} \approx 1$ indicate the diffusive nature of mass transfer. Furthermore, increasing Pe has no effect on flow characteristics showing that thermal convection also dominates the shear effect induced by driven wall. As Le increases, a descent in the values of $|\psi_c|$ and $\overline{Nu_h}$ while $\overline{Sh_h}$ starts to rise slowly indicate a change in the heat and mass transport mechanisms. Finally, for $Le > 1$, $\overline{Sh_h}$ increases monotonically knowing that Sherwood number depends strongly on Lewis number as increasing it strengthens convective mass transfer. In contrast, a lower plateau is observed for $|\psi_c|$ and $\overline{Nu_h}$ as heat transfer is mainly by diffusion (i.e., heat conduction). Further, the effect of varying Pe on flow characteristics becomes obvious signaling that shear force impacts the convective regime.

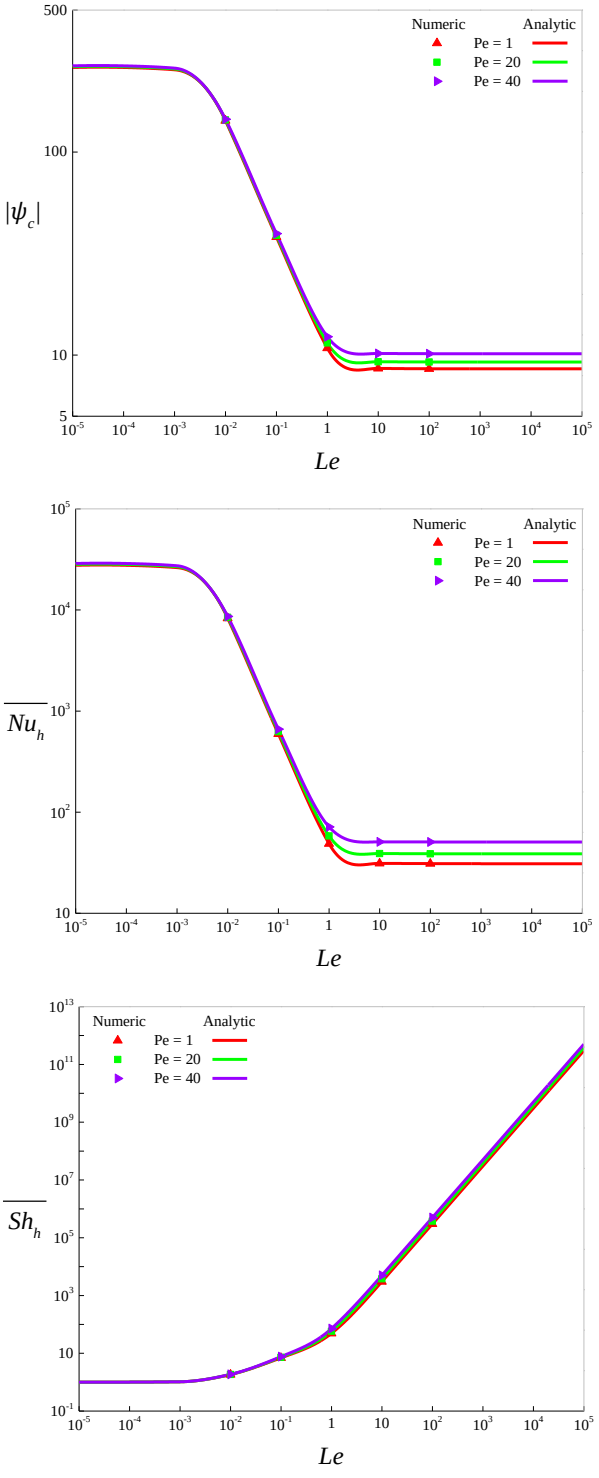

Figure 4.9. Evolutions of the stream function at the center of the cavity $(x = A/2,\ y = 1/2)$ (top), horizontal Nusselt number (middle), and horizontal Sherwood number (bottom) with Lewis number (Le) for $Ra_T = 10^5, N = 1$, and different values of Pe inside a single lid-driven cavity.

4.11 Effect of buoyancy ratio

The results of varying N on $|\psi_c|$, $\overline{Nu_h}$, and $\overline{Sh_h}$ are reported in Figure 4.10 for $Ra_T = 10^5$, $Le = 5$, and various values of Pe. For buoyancy aiding flow case ($N > 0$) discussed here, three convective regimes appear:

- for a range of small values of N ($N < 10$) , thermal buoyancy force dominates convection resulting in $|\psi_c|$, $\overline{Nu_h}$, and $\overline{Sh_h}$ being indifferent to changes in N value as solutal buoyancy force input is insignificant; thus, only the effect of the moving wall can be seen.
- an intermediate regime, for which the increase of $|\psi_c|$, $\overline{Nu_h}$, and $\overline{Sh_h}$ begins to be seen, the solutal buoyancy force starts to take importance compared to the thermal buoyancy one. As a result, the effect of the moving wall, acting in the same direction as the buoyancy forces to enhance convection, starts to diminish.
- a regime where $|\psi_c|$, $\overline{Nu_h}$, and $\overline{Sh_h}$ increase in a monotonous and pronounced way with N; further, the effect of the moving wall shear force vanishes indicating a convective regime where solutal buoyancy force is predominant.

We note that, beyond $Le = 10^3$ and $N = 10^3$, the numerical code cannot generate stable results.

4.12 Horizontal velocity, Temperature, and Concentration

Horizontal velocity (top), temperature (middle), and concentration (bottom) profiles at mid-length of the enclosure $\left(x = \frac{A}{2}\right)$ are shown in Figure 4.11 for $Pe = 25$, $Le = 5$, $N = 1$, and various representative values of Ra_T. The critical value of thermal Rayleigh number Ra_{Tcr} defines the onset of buoyancy-driven fluid flow. For dominant forced convection regime ($Ra_T < Ra_{Tcr}$), the illustrated profiles are asymmetric given the fact that horizontal dynamical boundary conditions are of asymmetric nature (only the top wall is moving). For the velocity, as Ra_T increases the extremum values augments where the minimum value becomes more amplified and the maximum value increases as it moves far from the moving wall ($y = 1$). Thus, indicating that the flow becomes faster and more intense in that region away from the moving wall, which shows that buoyancy force dominates convection ($Ra_T > Ra_{Tcr}$). The threshold that

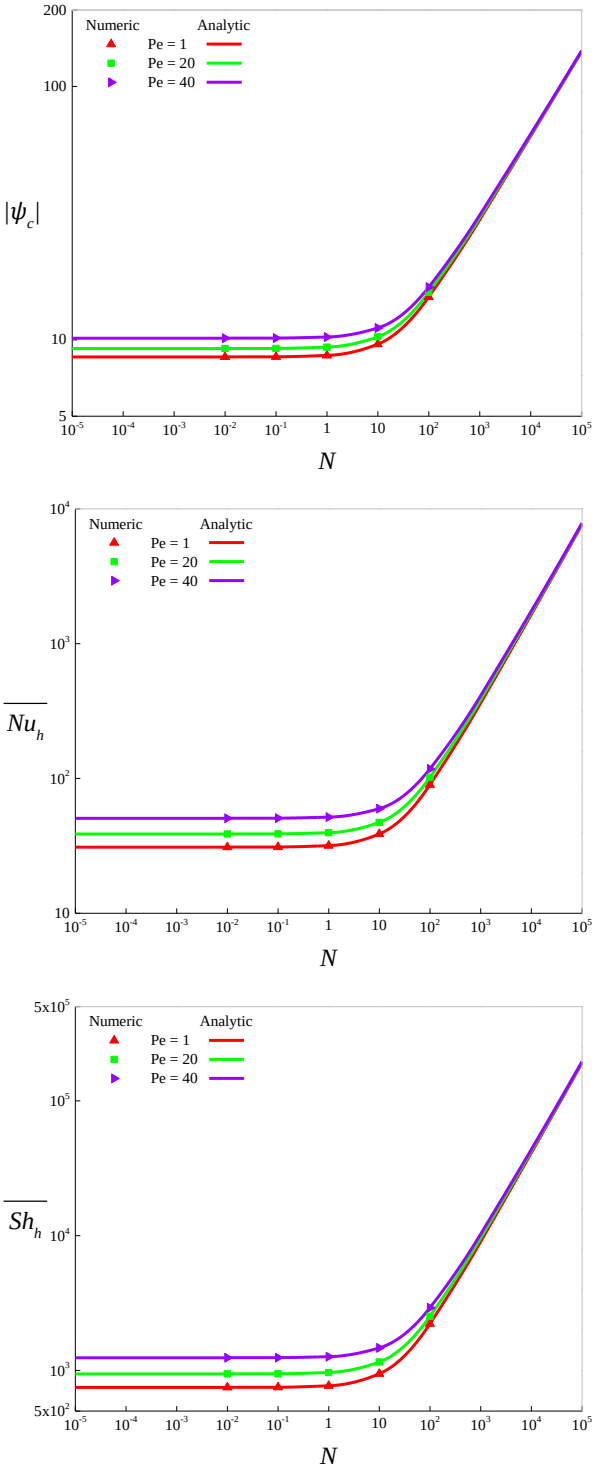

Figure 4.10. Evolutions of the stream function at the center of the cavity $(x = A/2,\ y = 1/2)$ (top), horizontal Nusselt number (middle), and horizontal Sherwood number (bottom) with buoyancy ratio (N) for $Ra_T = 10^5, Le = 5$, and different values of Pe inside a single lid-driven cavity.

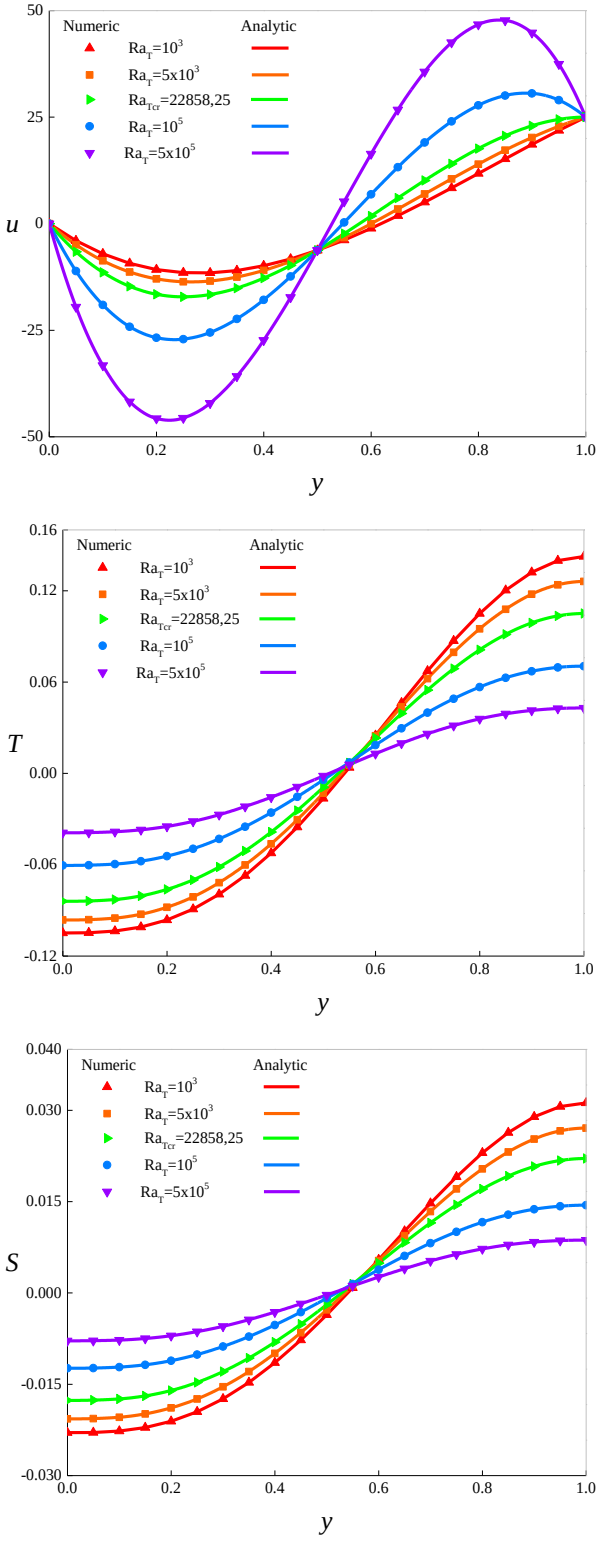

Figure 4.11. Horizontal velocity u (top), temperature T (middle), and concentration S (bottom) profiles at mid-length of the cavity $(x = A/2)$ along the vertical coordinate (y) for $Pe = 25, Le = 5, N = 1$, and various values of Ra_T inside a single lid-driven cavity. $Ra_{T(cr)}$ signals the onset of buoyancy-driven flow.

results in these extremums and indicates that the flow is buoyancy-driven (Ra_{Tcr}) is given by (see Figure 4.11):

$$Ra_{Tcr} = \frac{1}{\left[\frac{19}{630}(Le^2+N)Pe^2+1+N\right]}\left[\frac{1444}{33075}Le^2Pe^5 + \frac{152}{105}(1+Le^2)Pe^3 + 48Pe\right] \tag{4.8}$$

The fact that both shear and buoyancy effects work in the same direction from left to right results in monocellular clockwise flow, where the velocity is positive on the top region of the cavity while negative on the bottom. As for the temperature and concentration profiles, they also present two zones. The one with positive signs in the top and the one with negative signs in the bottom with extremum values that increases as Ra_T decreases indicating that the flow is losing its intensity, as confirmed by the velocity profiles and the values of heat and mass transfer rates that decrease as Ra_T decreases.

For temperature, the clockwise flow makes the top of the cavity warm and the bottom cold by transferring heat from the hot left wall and discharging it along the right wall. The concentration profiles are similar given that mass transfer exhibits similar phenomenon.

4.13 Conclusions

Double-diffusive mixed convection in a single lid-driven rectangular cavity filled with Newtonian fluid and subjected to uniform heat and mass fluxes applied to the vertical short sides (i.e., Neumann type conditions) while the long horizontal boundaries are insulated and impermeable is studied numerically and analytically. In the case of shallow enclosures ($A \geq 24$), the flow characteristics become indifferent to aspect ratio A variation. Likewise, for Prandtl numbers $Pr \geq 10$, varying Pr does not influence fluid flow and heat and mass transfer characteristics. As a result, the main parameters governing convection reduce to: Péclet number Pe, thermal Rayleigh number Ra_T, Lewis number Le, buoyancy ratio N. Numerical solutions, using finite volume method, are given for wide ranges of governing parameters ($10^{-2} \leq Le \leq 10^2,\ 10^{-2} \leq N \leq 10^2,\ 0.1 \leq \mathrm{Pe} \leq 500,\ 1 \leq \mathrm{Ra_T} \leq 10^7$). Further, using the parallel flow approximation valid for shallow enclosures, an analytical solution is established. Both solutions show good agreement within the explored ranges of the governing parameters.

The finite difference method also shows a perfect agreement with the numerical results obtained by the finite volume method.

The parameter $Ra_T/Pe^{3.0}$ is found to perfectly outline natural, forced, and mixed convective regimes, where the following boundaries:

$$0.0079 < \frac{Ra_T}{Pe^{3.0}} < 584.83$$

delimit the mixed regime for shallow single lid-driven rectangular cavity filled with Newtonian fluid and for governing parameters $Le = 1$ and $N = 1$. Whereas natural and forced regimes are found to dominate outside these limits.

The effects of governing parameters on fluid flow and heat and mass transfer are investigated, where increasing Péclet number results in stronger shear effect; thus, enhances flow intensity and heat and mass transfer rates. While increasing Rayleigh number results in a similar effect, but this time due to reinforced buoyancy force which leads to a more active convection. Lewis number affects strongly mass transfer while no change is noticed on flow intensity and heat transfer. As for increasing buoyancy ratio, it enhances flow characteristics as a beneficial result of dominant mass buoyancy force.

CHAPTER 5 Double-Diffusive Mixed Convection in Double Lid- Driven Rectangular Cavities Filled with Non-Newtonian Fluids

5.1 Introduction

In this chapter we investigate, both numerically and analytically, rectangular cavities (Fig. 5.1) confining non-Newtonian fluids and subjected to uniform density of heat and mass fluxes along the short vertical walls, whereas the long horizontal ones are insulated and impermeable ($a = c = 1\ and\ b = d = 0$). As for the kinematic boundary conditions, both horizontal walls move in opposite directions with the same uniform velocity u_0' acting in the same direction as imposed heat and mass fluxes ($e = 1$), while the vertical ones are motionless. Numerical tests show that for Prandtl numbers $Pr \geq 10$, increasing it further does not affect non-Newtonian fluids flow and heat and mass transfer. The effects of governing parameters on double-diffusive mixed convection fluid flow and heat and mass transfer characteristics are thoroughly inspected for the three separate regimes: natural, mixed, and forced convection.

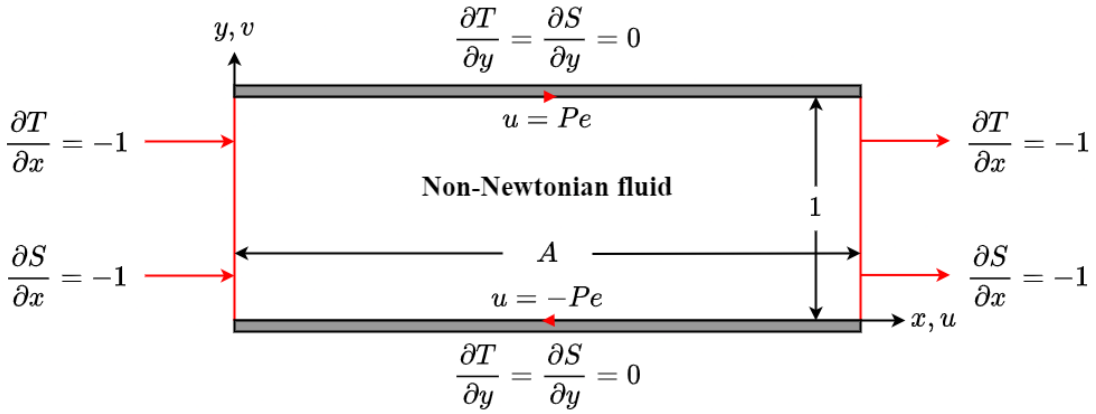

Figure 5.1. Geometry of the investigated configuration along with coordinate system and associated boundary conditions. Uniform density of heat and mass fluxes are applied to motionless vertical walls, while the horizontal ones are insulated, impermeable, and move in opposite directions with the same uniform velocity.

5.2 Numerical code validation

In chapter 4, we confirm the accuracy of our numerical code for modeling mixed convection inside lid-driven cavities. Additionally, and in order to examine the numerical code ability to generalize to non-Newtonian flows, Table 5.1 shows a comparison with published results for different power-law indexes in terms of the relative average Nusselt number Nu_r (ratio of the average Nusselt number for non-Newtonian fluid $Nu_{n\#1}$ to that of Newtonian fluid $Nu_{n=1}$). Here again, the present results are fully consistent with the benchmark results justifying the use of the present numerical code to simulate non-Newtonian fluids' flow characteristics. It is worth mentioning that Prandtl number and Rayleigh number used in Table 5.1 benchmark studies are given by [96, 97]:

$$Pr^* = \frac{(k/\rho)^{1/(2-n)} {H'}^{2(1-n)/(2-n)}}{\alpha} \text{ and } Ra^* = \frac{g\beta_t {H'}^4 q'}{(k/\rho)^{1/(2-n)} {H'}^{2(1-n)/(2-n)} \alpha\lambda} \quad (5.1)$$

linked to Pr and Ra_T defined in Eq. (3.26) by the following expressions:

$$Pr = {Pr^*}^{(2-n)} \text{ and } Ra_T = Ra^* Pr^{\frac{n-1}{2-n}} \quad (5.2)$$

5.3 Mesh size choice

As before, the choice of the grid size is made in order to get the best tradeoff between the computation time and the solutions accuracy. Tables 5.2, 5.3, and 5.4 show that for $A = 24$ (value after which the flow characteristics become independent of the aspect ratio A) a uniform grid size of 381×121 is sufficient to model accurately non-Newtonian fluids flow and temperature and concentration distributions inside double lid-driven rectangular cavities.

Table 5.1 – Comparison of relative average Nusselt number ($Nu_r = Nu_{n\#1}/Nu_{n=1}$) for $Pr^* = 100,\ Ra^* = 10^4\ and\ 10^5$ and different values of n.

	Ra^*	$n = 0.6$	$n = 0.8$	$n = 1.0$	$n = 1.2$	$n = 1.4$
Present work	10^4	1.06	1.03	1	0.97	0.94
Present work	10^5	1.45	1.16	1	0.89	0.82
Ref. [96]	10^4	1.04	1.02	1	0.97	0.93
Ref. [96]	10^5	1.48	1.18	1	0.89	0.82
Ref. [97]	10^4	-	-	-	-	-
Ref. [97]	10^5	1.46	1.17	1	-	-

Table 5.2 – Convergence tests for $A = 24, Ra_T = 10^5, Le = 10, N = 1, n = 0.6$, and different values of Pe in a double lid-driven cavity.

Pe	Grids					Analytical solution
	(241,61)	(321,81)	(381,121)	(421,121)	(481,181)	
			$\lvert\psi_c\rvert$			
0.1	20.472	19.514	19.069	18.91	18.691	18.77988
25	24.402	20.736	20.303	20.138	19.8344	19.43714
100	32.352	31.731	31.533	31.434	31.338	31.99374
			$\overline{Nu_h}$			
0.1	141.28	142.993	142.247	142.704	142.256	145.412
25	169.328	171.575	174.113	174.747	173.489	181.2176
100	439.057	462.393	473.12	479.579	486.51	483.02
			$\overline{Sh_h}$			
0.1	14021	14211.2	14252.5	14330.5	14270.8	14442.2
25	16835.2	17056.5	17525.6	17623.8	17449.7	18022.76
100	43808.4	46138.5	47213	47857	48549.2	48203

Table 5.3 – Convergence tests for $A = 24, Ra_T = 10^5, Le = 10, N = 1, n = 1.0$, and different values of Pe in a double lid-driven cavity.

Pe	Grids					Analytical solution
	(241,61)	(321,81)	(381,121)	(421,121)	(481,181)	
			$\lvert\psi_c\rvert$			
0.1	8.617	8.514	8.492	8.485	8.466	8.559681
25	10.915	10.82	10.789	10.792	10.784	10.63974
100	25.726	25.696	25.687	25.684	25.683	26.73264
			$\overline{Nu_h}$			
0.1	30.673	31.011	31.057	31.088	31.098	30.82649
25	56.118	57.19	57.447	57.57	57.568	59.92474
100	336.895	350.14	354.323	356.217	357.226	361.091
			$\overline{Sh_h}$			
0.1	2872.06	2920.249	3001.5	3005.2	3006.4	2983.649
25	5512.8	5620	5738.7	5758	5757.2	5893.474
100	33590.5	34915	35330	35525	35620.3	36010.1

Table 5.4 – Convergence tests for $A = 24, Ra_T = 10^5, Le = 10, N = 1, n = 1.4$, and different values of Pe in a double lid-driven cavity.

Pe	Grids					Analytical solution
	(241,61)	(321,81)	(381,121)	(421,121)	(481,181)	
			$\|\psi_c\|$			
0.1	4.581	4.617	4.61	4.591	4.471	4.664025
25	7.616	7.57	7.55	7.587	7.616	7.640985
100	25.028	25.052	25.054	25.052	24.916	25.00425
			$\overline{Nu_h}$			
0.1	9.746	9.941	9.797	9.855	10.275	9.805278
25	31.192	31.1	32.095	31.78	31.228	30.77634
100	332.656	341.368	334.097	333.4	324.861	339.618
			$\overline{Sh_h}$			
0.1	795.151	865.09	860.853	833.234	790.289	881.5278
25	3052.157	3120.496	3099.7	3075	3020.5	2978.634
100	33155.6	34020.8	33350.2	33215	32350.7	33862.8

5.4 Value of A satisfying the large aspect ratio approximation

Figure 5.2 show the evolutions of $\overline{Nu_h}$ with A for $Ra_T = 10^5$, $Le = 10$, $N = 1$, and various values of Pe and n. As the aspect ratio increases, an asymptotic behavior of $\overline{Nu_h}$ can be seen with forced convection regime ($Pe \geq 100$) playing a role in delaying the reach of the asymptotic state which is more obvious for pseudoplastic fluids $(0 < n < 1)$. Thus, for all considered values of governing parameters, $A = 24$ is the smallest value of the cavity aspect ratio for which numerical results become independent of A and match the results obtained analytically.

All things considered, double-diffusive mixed convection in shallow lid-driven rectangular cavities filled with non-Newtonian fluids is mainly governed by: Péclet number Pe, thermal Rayleigh number Ra_T, Lewis number Le, buoyancy ratio N, and power-law behavior index n.

5.5 Mixed convection parameter

The literature proposes many disconnected indications to distinct natural, mixed, and forced regimes. Further, the proposed mixed convection parameters do not take into account the working fluid nature especially the non-linear behavior of non-Newtonian

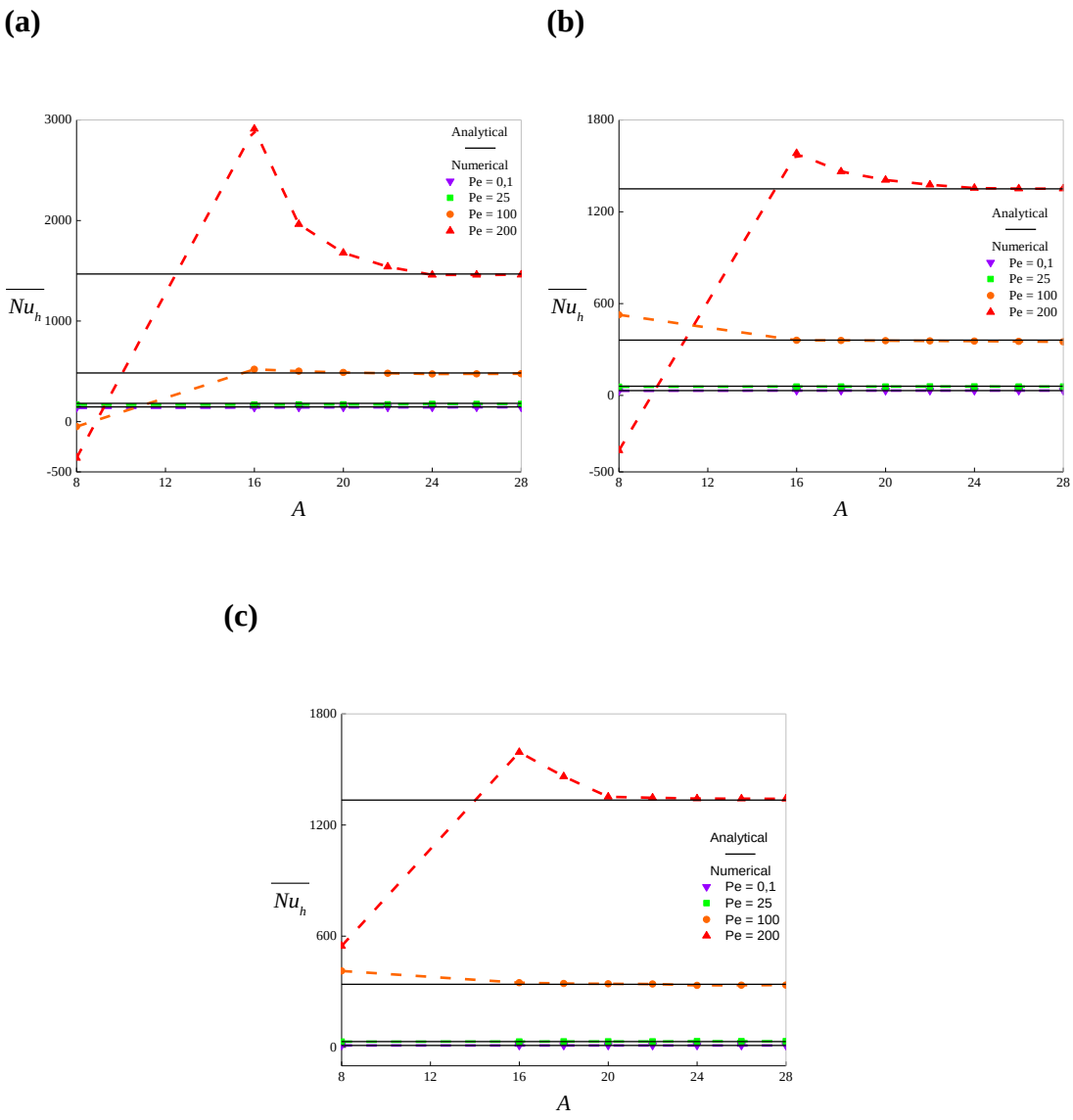

Figure 5.2. Variation of numerical horizontal Nusselt number $(\overline{Nu_h})$ with the cavity aspect ratio $\left(A = \frac{L'}{H'}\right)$ while varying Péclet number (Pe) to account for the different convective regimes (natural, mixed, and forced convection) for: (a) pseudoplastic fluid $(n = 0.6)$, (b) Newtonian fluid $(n = 1.0)$, and (c) dilatant fluid $(n = 1.4)$ at $Ra_T = 10^5, Le = 10,$ and $N = 1$ inside double lid-driven cavities.

fluids despite their importance for both academic and industrial sectors. Consequently, the limits between convective regimes need to be defined with a clear and practical criterion taking into account non-Newtonian fluids nature. The same numerical procedure as explained in the previous chapter, with a threshold of 5%, is adopted to separate the three convective regimes.

Figure 5.3 is built using Eq. (4.1) where the points $\left(log\ (Ra_T), log(Pe)\right)$ that verify $\varepsilon_{Nu_{h,n}} = 5\%$ and $\varepsilon_{Nu_{h,f}} = 5\%$ are obtained analytically (solid lines) and numerically (symbols). The agreement between both solutions is obvious. For each considered value of the power-law behavior index n, two parallel straight lines split the domain of explored ranges of Ra_T and Pe into three distinct zones as discussed in the previous chapter. The shift from dominant natural regime to dominant forced regime for the same value of Ra_T requires higher values of Pe as n decreases, indicating that the transition requires higher shear force as the fluid behavior changes from shear thickening to shear thinning. Such result is to be expected as decreasing n enhances natural convection flow characteristics; thus, delaying the transition toward dominant forced regime. Lines (1) and (2) can be correlated in the form of the mixed convection parameter as follows:

- For $n = 0.6$:

$$\frac{Ra_T}{Pe^{2.6}} = \eta_n \text{ and } \frac{Ra_T}{Pe^{2.6}} = \eta_f \tag{5.3}$$

- For $n = 1.0$:

$$\frac{Ra_T}{Pe^{3.0}} = \eta_n \text{ and } \frac{Ra_T}{Pe^{3.0}} = \eta_f \tag{5.4}$$

- For $n = 1.4$:

$$\frac{Ra_T}{Pe^{3.4}} = \eta_n \text{ and } \frac{Ra_T}{Pe^{3.4}} = \eta_f \tag{5.5}$$

representing the limits for natural and forced regime, respectively. The fluid nature affects the exponent γ as it increases with the power-law behavior index. The values of coefficients η_n and η_f are given in Table 5.5 and illustrated in Figure 5.3 with dashed lines for different values of n. Accordingly, and for $Le = 1$ and $N = 1$, mixed convection regime in the case of double-lid driven rectangular cavities filled with non-Newtonian fluids and subjected to horizontal uniform density of heat and mass fluxes is delimited as follows:

$$0.0259 < \frac{Ra_T}{Pe^{2.6}} < 452.21;\ 0.0299 < \frac{Ra_T}{Pe^{3.0}} < 7085;$$
$$0.0225 < \frac{Ra_T}{Pe^{3.4}} < 86710 \tag{5.6}$$

for $n = 0.6, n = 1.0,$ and $n = 1.4$, respectively.

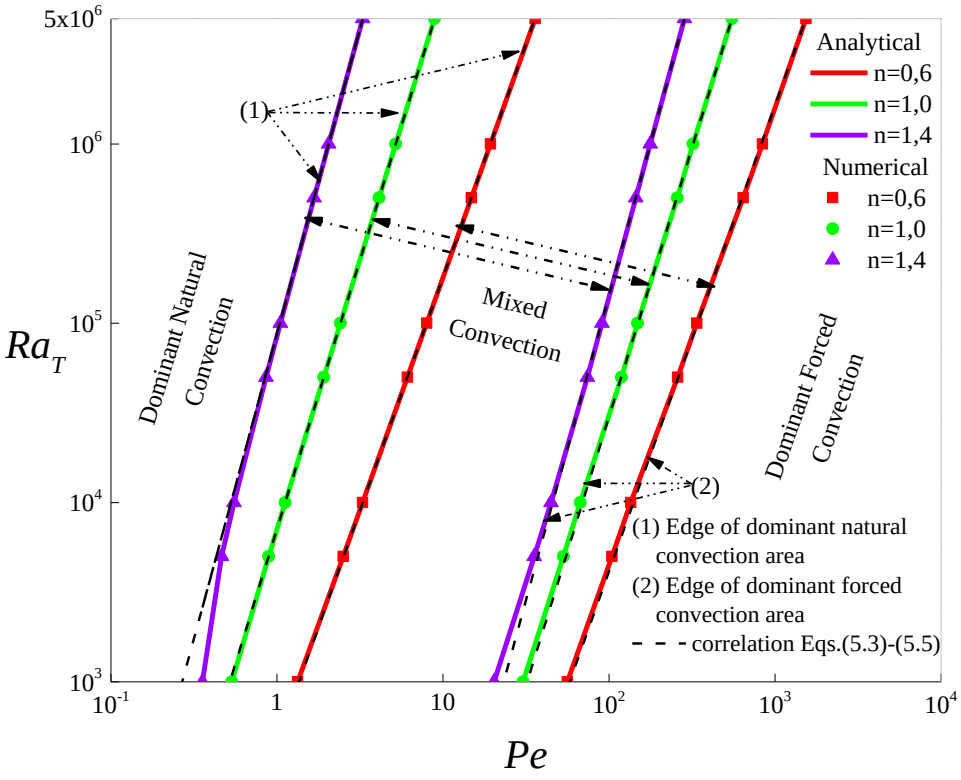

Figure 5.3. The dominance regions of the three convective regimes: natural, forced, and mixed convection for different values of flow behavior index n at $Le = 1$ and $N = 1$ inside double lid-driven rectangular cavities.

Table 5.5 – Correlation coefficients η_n and η_f for characteristic values of n.

Power-law behavior index n	**Natural convection** η_n	**Forced convection** η_f
0.6	452.21	0.0259
1.0	7085	0.0299
1.4	86710	0.0225

5.6 Dynamical, thermal, and solutal structures

Representative streamlines (top), isotherms (middle), and iso-concentrations (bottom) are displayed in Figures 5.4, 5.5, and 5.6 for $Ra_T = 10^5, Le = 10, N = 1$, and several characteristic values of Pe and n. As expected, the flow is unicellular and clockwise owing to the fact that buoyancy force and moving walls shear effect are acting in the same direction from left to right. Furthermore, excluding the end sides near the vertical

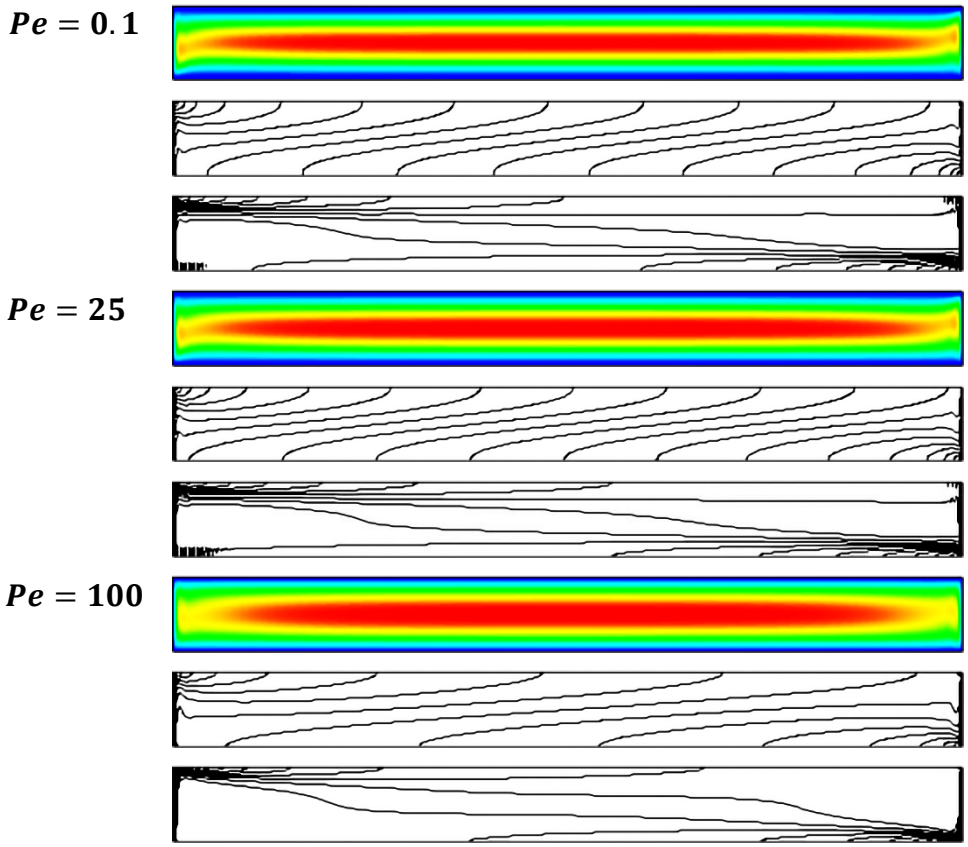

Figure 5.4. Streamlines (top), isotherms (middle), and iso-concentrations (bottom) for pseudoplastic fluid $(n = 0.6)$ at $A = 24, Ra_T = 10^5$, $Le = 10$ and $N = 1$ while varying Péclet number (Pe) inside double lid-driven rectangular cavity. (Scale not respected).

walls where the flow undergoes a rotation of 180°, streamlines exhibit a parallel aspect in the central part of the cavity. The isotherms and iso-concentrations are linearly stratified in the x-direction, where they become less inclined with regard to the vertical direction as n increases.

For low values of Pe, the profiles are similar to the ones obtained in the case of pure natural convection (see Figure 5.7). The streamlines are shifted away from horizontal walls indicating the absence of fluid circulation due to moving walls. Accordingly, natural convection predominates fluid flow $\left(\frac{Ra_T}{Pe^{\gamma}} > \eta_n\right)$. As Pe increases, the streamlines become more crowded near the sliding horizontal walls signaling a strong flow circulation in that region and confirm that forced convection dominates natural convection $\left(\frac{Ra_T}{Pe^{\gamma}} < \eta_f\right)$. This occurs first for dilatant fluids, given that decreasing the

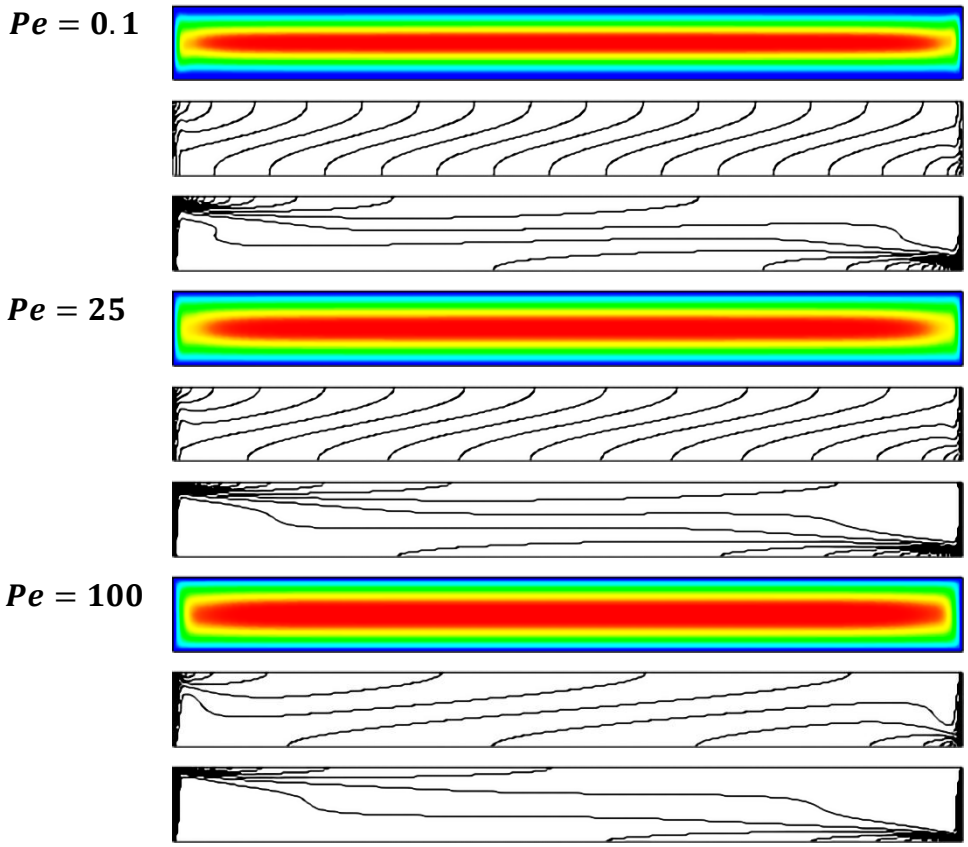

Figure 5.5. Streamlines (top), isotherms (middle), and iso-concentrations (bottom) for Newtonian fluid ($n = 1.0$) at $A = 24, Ra_T = 10^5$, $Le = 10$ and $N = 1$ while varying Péclet number (Pe) inside double lid-driven rectangular cavity. (Scale not respected).

power-law index strengthens natural convection fluid flow and heat and mass transfer characteristics leading to delay the dominance of the forced regime. As for temperature and concentration fields, we observe that as Pe rises, thinner boundary layers appear near both vertical walls indicating a strong temperature and concentration gradients in these end regions. The layers' widths grow and become more noticeable as n increases.

For high enough values of Pe ($Pe = 100$), the isotherms and iso-concentrations become practically linear in the center of the cavity where the results match the ones found in the case of pure forced convection (see Figure 5.8).

5.7 Effect of Péclet number

The evolutions of flow characteristics $|\psi_c|$, $\overline{Nu_h}$, and $\overline{Sh_h}$ with Péclet number Pe are shown in Figure 5.9, for $Le = 10, N = 1$, and different values of Ra_T and n. For low

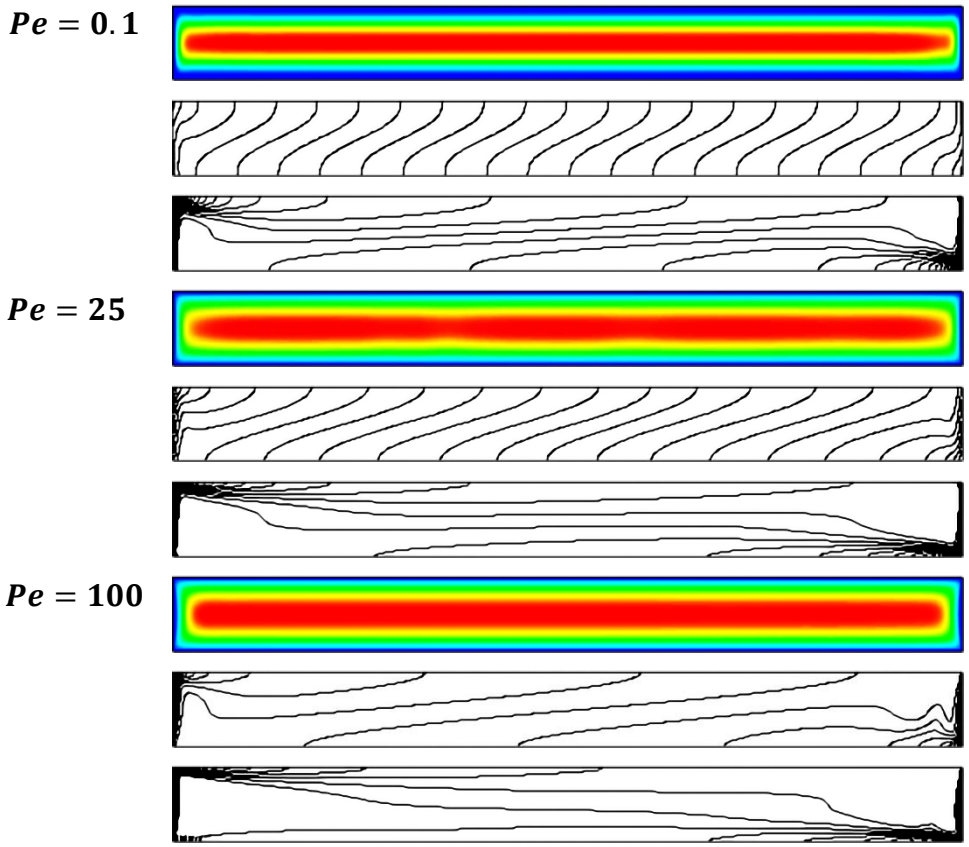

Figure 5.6. Streamlines (top), isotherms (middle), and iso-concentrations (bottom) for dilatant fluid $(n = 1.4)$ at $A = 24, Ra_T = 10^5$, $Le = 10$ and $N = 1$ while varying Péclet number (Pe) inside double lid-driven rectangular cavity. (Scale not respected).

values of Pe, the natural convection regime is clearly dominating $\left(\frac{Ra_T}{Pe^{\gamma}} > \eta_n\right)$ as the intensity of fluid circulation and heat and mass transfer rates are not affected while increasing Pe. Plus, the obtained results are identical to those obtained in the case of pure natural convection shown as dashed lines. After a given value of Pe, a slow increase of the illustrated quantities begins to show denoting a regime change from natural to mixed convection. The said value of Pe depends on Ra_T and n, as increasing thermal Rayleigh number or decreasing the power-law index delays the transition from natural regime to mixed one. The former strengthens buoyancy force while the latter enhances convective flow characteristics in natural regime; therefore, the transition requires greater Pe values (higher shear force). Finally, for high values of Péclet number, the three quantities rise in a monotonous way matching the results obtained in pure forced convection regime, illustrated as dashed lines; thus, indicating that forced

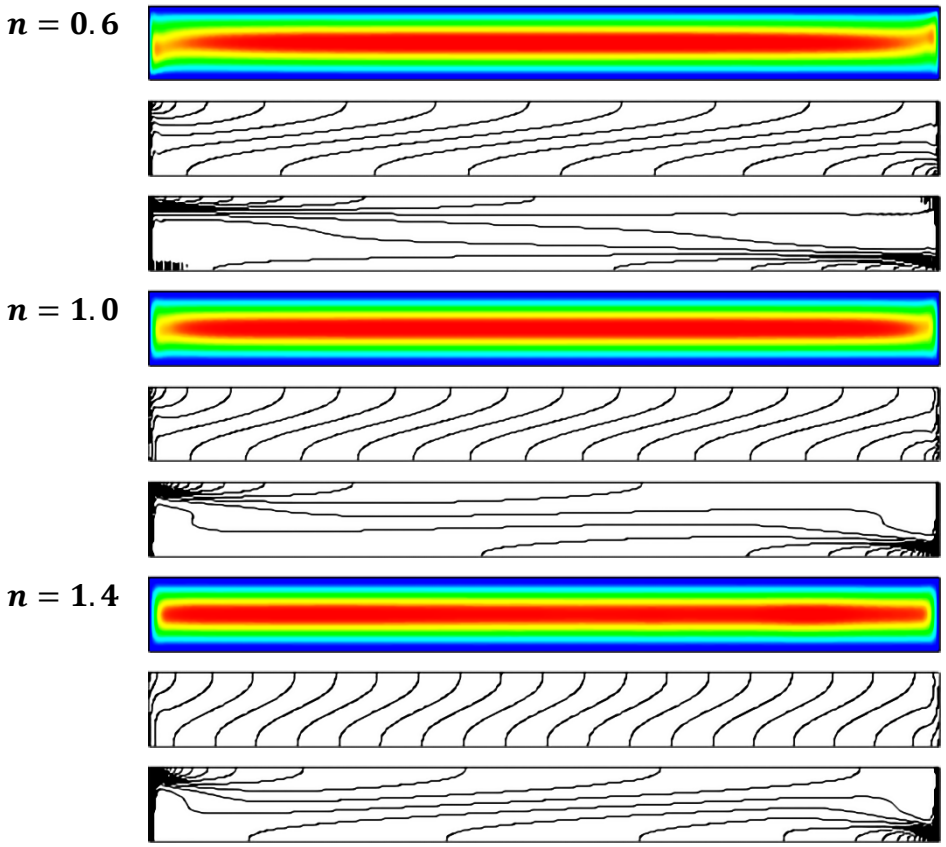

Figure 5.7. Streamlines (top), isotherms (middle), and iso-concentrations (bottom) for pure natural convection at $Ra_T = 10^5, Le = 10,$ and $N = 1$. The results are presented for different fluid behaviors: pseudoplastic $(n = 0.6)$, Newtonian $(n = 1.0)$, and dilatant $(n = 1.4)$ inside double lid-driven rectangular cavity. (Scale not respected).

convection dominates fluid flow and heat and mass transfer. The observed effect of Pe can be further confirmed from Fig. 10(a) showing that as Pe increases, the value of y_0 decreases until it reaches zero, meaning that the effect of moving walls dominates the convection $\left(\frac{Ra_T}{Pe^{\gamma}} < \eta_f\right)$. The fluids with shear-thickening behavior are the first to reach the forced regime compared to shear-thinning ones.

One key finding is that, as forced convection contribution in the convective regime begins to strengthen while increasing Pe, the effect of n on flow characteristics begins to shrink until it vanishes totally as forced convection fully dominates the convective regime. Therefore, the strength of sliding walls shear force can affect non-Newtonian fluids rheological behavior.

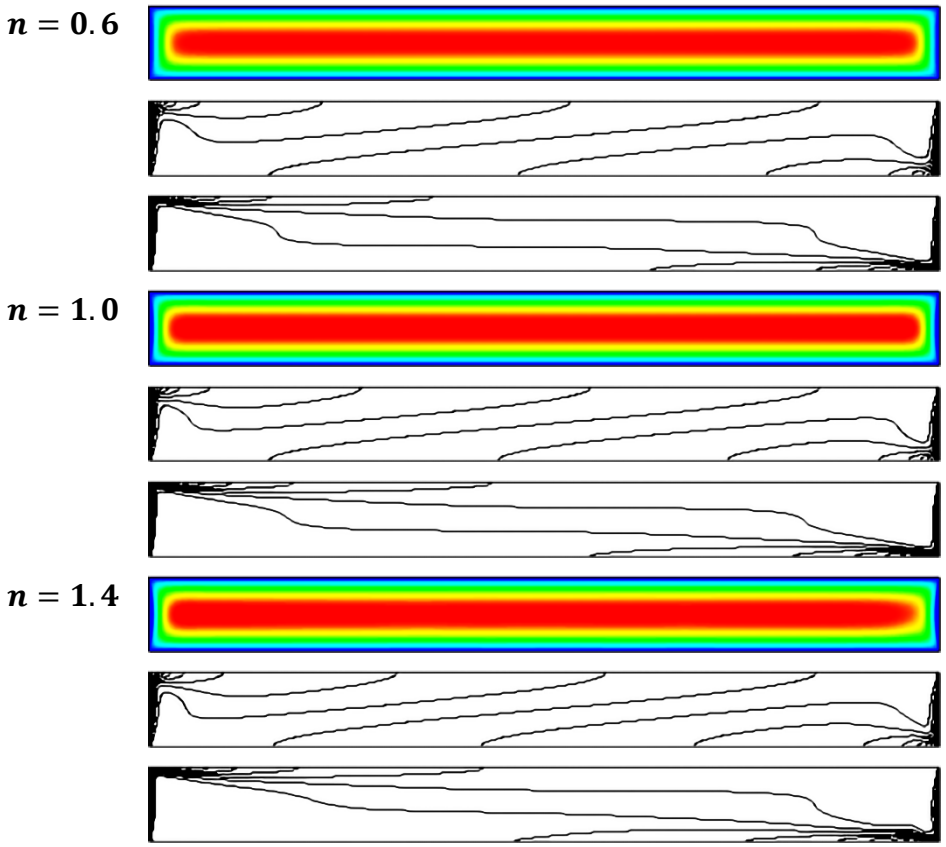

Figure 5.8. Streamlines (top), isotherms (middle), and iso-concentrations (bottom) for pure forced convection ($Ra_T = 0$) at $Pe = 100, Le = 10,$ and $N = 1$. The results are presented for different fluid behaviors: pseudoplastic ($n = 0.6$), Newtonian ($n = 1.0$), and dilatant ($n = 1.4$) inside double lid-driven rectangular cavity. (Scale not respected).

5.8 Effect of thermal Rayleigh number

The effects of thermal Rayleigh number Ra_T on quantities $|\psi_c|$, $\overline{Nu_h}$, and $\overline{Sh_h}$ are illustrated in Figure 5.11 for $Le = 10, N = 1$, and several Pe and n values. For the first interval of small values of Ra_T, no change is observed on the presented flow characteristics and the fluids power-law behavior index does not affect the results. These observations are similar to the ones made in the previous section where forced convection dominates fluid flow and heat and mass transfer and diminish the effect of non-Newtonian fluids behavior $\left(\frac{Ra_T}{Pe^{\gamma}} < \eta_f\right)$. Moreover, the results agree with the ones obtained for pure forced convection ($Ra_T = 0$) presented as dashed lines. The range of the interval characterized by forced convection dominance depends on the values of

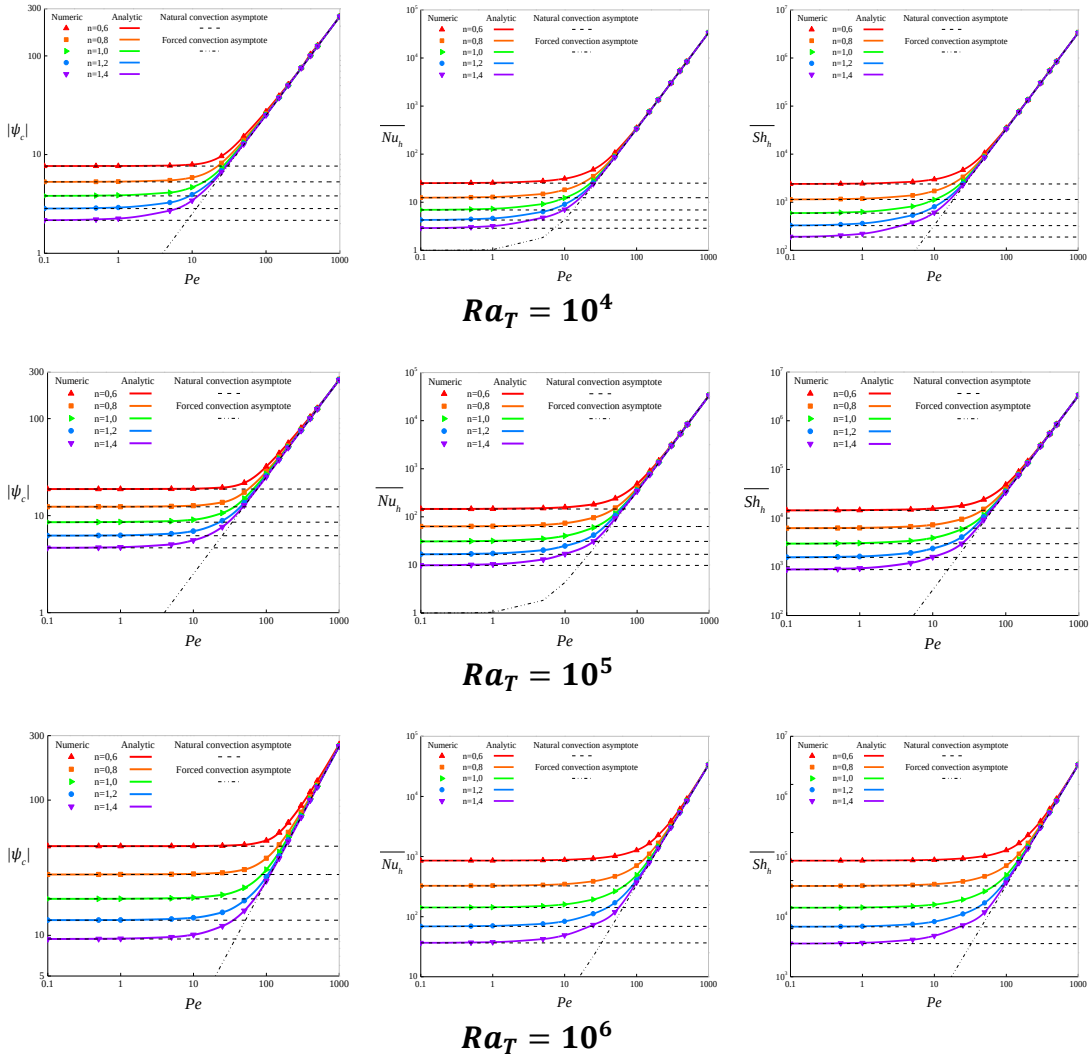

Figure 5.9. Evolutions of the stream function at the center of the cavity $(x = A/2,\ y = 1/2)$ (left), horizontal Nusselt number (middle), and horizontal Sherwood number (right) with Péclet number (Pe) for $Le = 10, N = 1$, and different values of Ra_T and n inside double lid-driven cavities.

both Péclet number and power-law index. Increasing Pe increases the range as it strengthens the shear force driving forced convection, while decreasing n does the opposite as it enhances natural convection flow characteristics which accelerates the transition. Next, the quantities start to rise slowly as Ra_T increases indicating a phase change, this time shifting from dominant forced regime to mixed convection regime as natural convection starts to contribute in overall convection resulting in a more active convection. Finally, $|\psi_c|$, $\overline{Nu_h}$, and $\overline{Sh_h}$ increase linearly with Ra_T and the effect of n becomes noticeable as shear-thinning fluids have higher heat and mass transfer rates

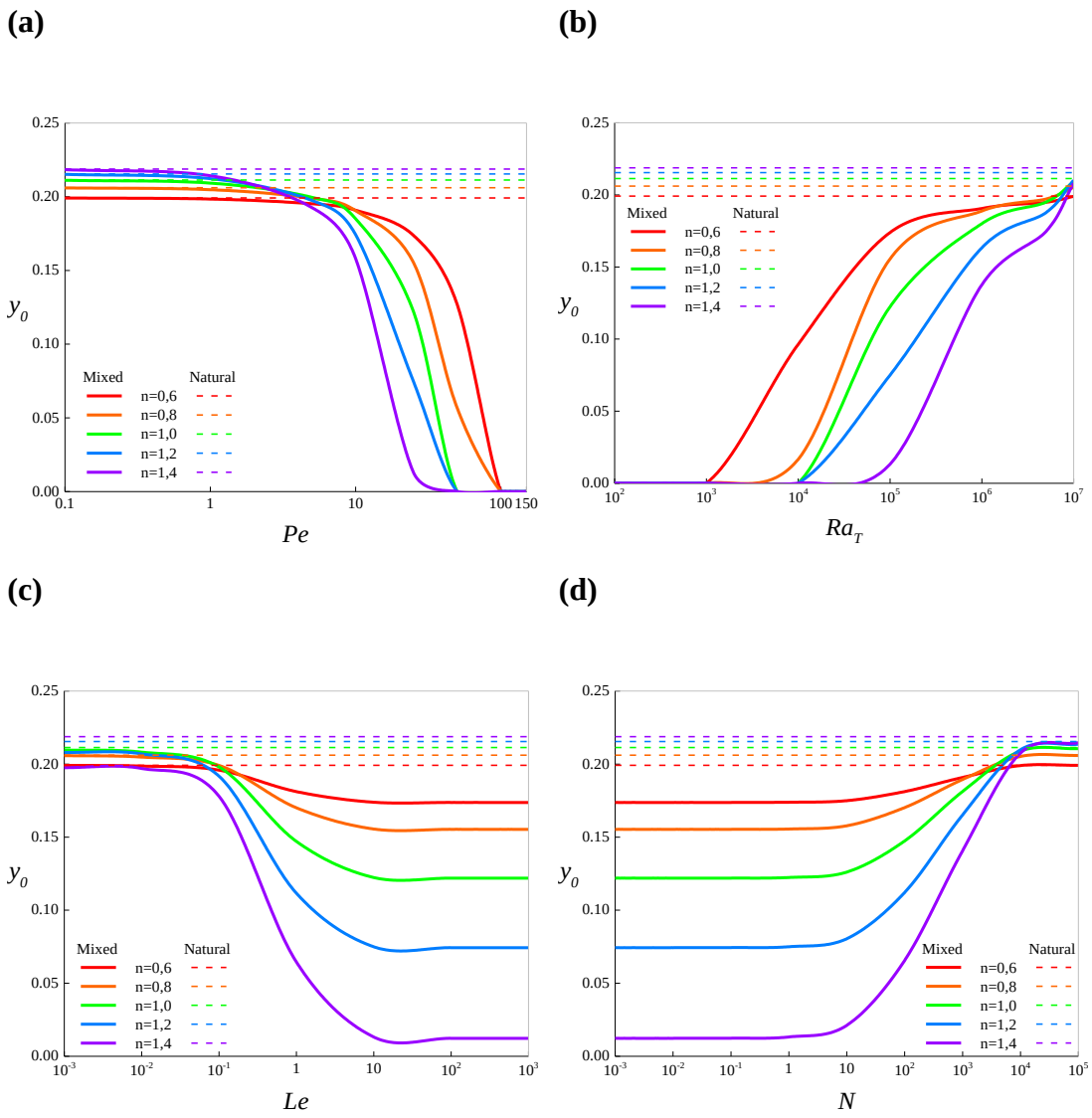

Figure 5.10. Effects of governing parameters on y_0 values (defining the vertical distance between the point with maximum velocity and the sliding wall): (a) effect of Pe $(Ra_T = 10^5, Le = 10, N = 1)$, (b) effect of Ra_T $(Pe = 25, Le = 10, N = 1)$, (c) effect of Le $(Pe = 25, Ra_T = 10^5, N = 1)$, and (d) effect of N $(Pe = 25, Ra_T = 10^5, Le = 10)$ all for different values of n.

with respect to Newtonian and shear-thickening fluids. The enhancing effect of decreasing n amplifies while increasing Ra_T showing that the convective regime is now governed by natural convection $\left(\frac{Ra_T}{Pe^{\gamma}} > \eta_n\right)$ where the results match the pure natural convection ones for all considered values of power-law index (dashed lines).

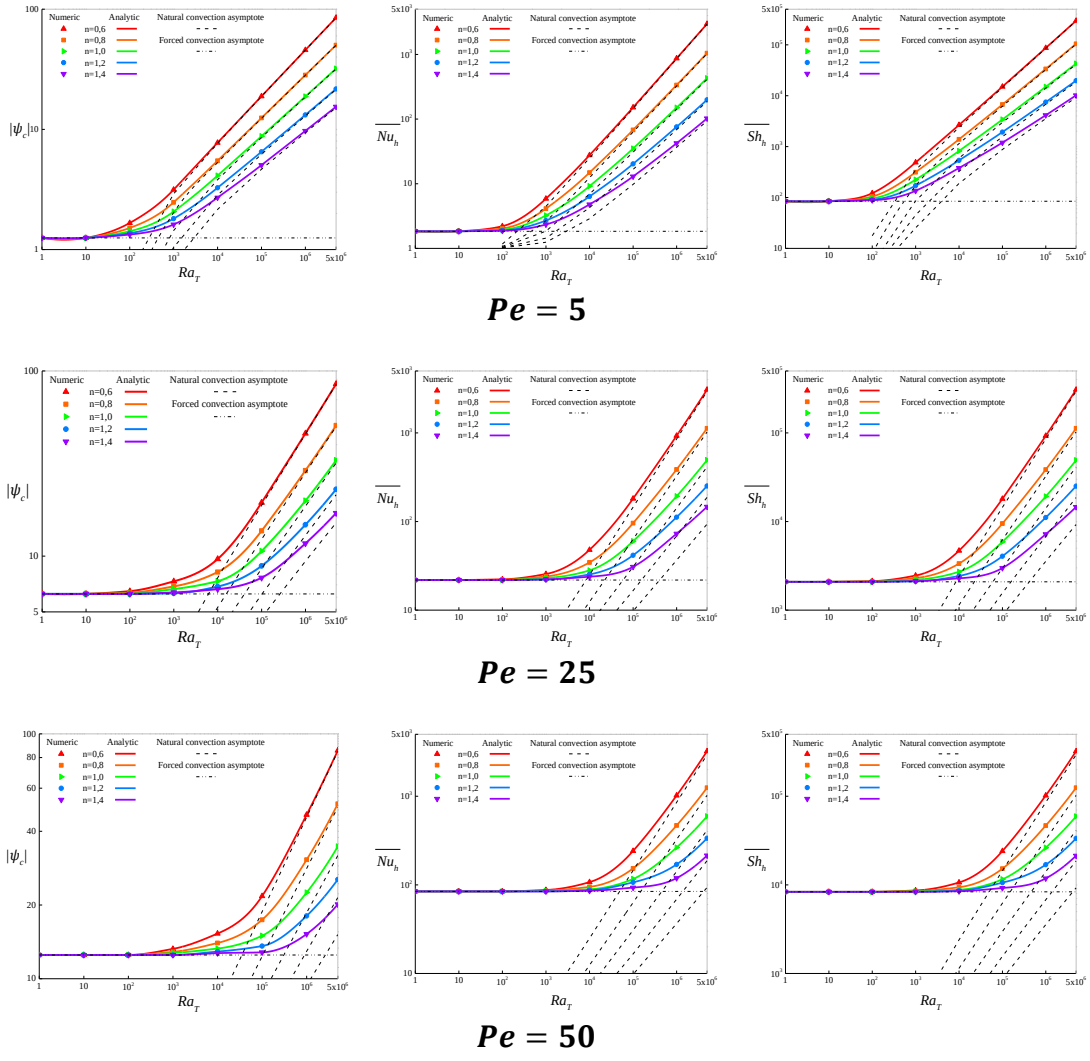

Figure 5.11. Evolutions of the stream function at the center of the cavity $(x = A/2,\ y = 1/2)$ (left), horizontal Nusselt number (middle), and horizontal Sherwood number (right) with thermal Rayleigh number (Ra_T) for $Le = 10, N = 1$, and different values of Pe and n inside double lid-driven cavities.

The previous conclusions are well confirmed by the variation of y_0 with Ra_T given in Fig. 10(b). The value of y_0 increases from zero to a value close to the one obtained in the case of pure natural convection as thermal Rayleigh number keeps increasing, indicating a shift from pure forced regime to pure natural one via the mixed regime.

5.9 Effect of Lewis number

The variations of $|\psi_c|$, $\overline{Nu_h}$, and $\overline{Sh_h}$ with Lewis number Le are presented in Figure 5.12 for $Ra_T = 10^5$, $N = 1$, and different values of Pe and n. Fluid flow intensity and

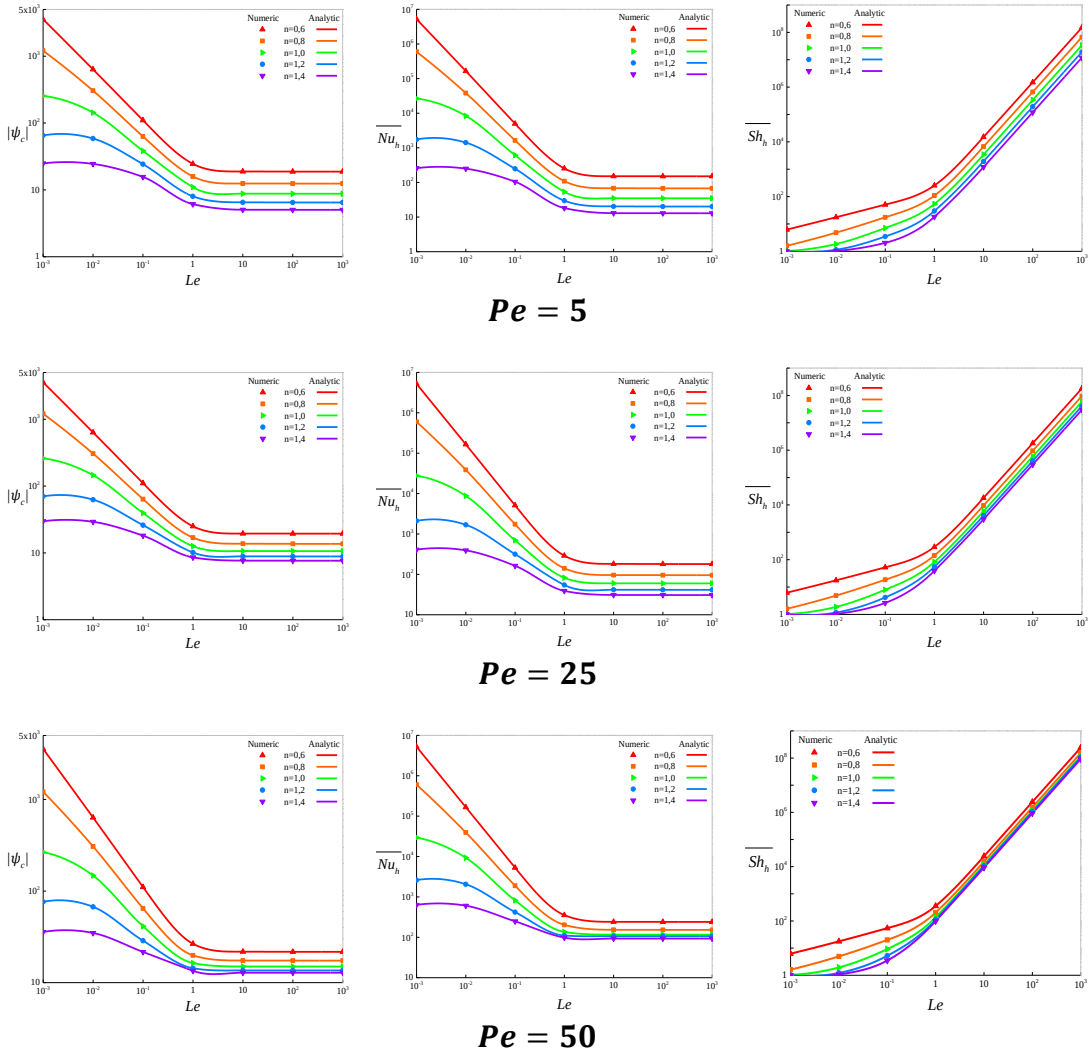

Figure 5.12. Evolutions of the stream function at the center of the cavity $(x = A/2,\ y = 1/2)$ (left), horizontal Nusselt number (middle), and horizontal Sherwood number (right) with Lewis number (Le) for $Ra_T = 10^5, N = 1$, and different values of Pe and n inside double lid-driven cavities.

Nusselt number display similar trends and we can discuss the influence of Lewis number on illustrated quantities separately for three zones. First, for low values of Le, higher plateaus for $|\psi_c|$ and $\overline{Nu_h}$ are observed while $\overline{Sh_h} \approx 1$ owing to the fact that heat transfer dominates mass transfer which is almost by diffusion given the high mass diffusivity related to small values of Lewis number. At this stage, the variation of Pe has no effect on all quantities and the values of y_0 are close to the ones obtained for pure natural regime (Fig. 10(c)) which indicates that the regime is governed by natural convection. Next, as Le keeps rising, a descent from the higher plateaus is observed for $|\psi_c|$ and $\overline{Nu_h}$ while $\overline{Sh_h}$ starts to rise slowly, signaling a change in the transport

mechanism as heat transfer hand it's leading role to mass transfer. Finally, for high values of Le, $|\psi_c|$ and $\overline{Nu_h}$ reach lower plateaus and remain unchanged owing to high thermal diffusivity related to high values of Le. In contrast, $\overline{Sh_h}$ rises in a monotonous way due to the well-established effect of Lewis number on strengthening mass transfer as the corresponding diffusivity reduces significantly.

As Le keeps increasing, the non-Newtonian fluids behavior is affected as the influence of n reduces especially for high values of Pe. The shear thickening fluids ($n > 1$) are the first to be influenced as illustrated in figure 5.12 and confirmed from Fig. 10(c). The y_0 values of shear thickening fluids are the fastest to reach zero meaning that forced convection starts to dominate the fluid flow and heat and mass transfer. The results reveal the interesting role of Le in promoting forced convection contribution in the overall convective regime.

5.10 Effect of buoyancy ratio

The effects of buoyancy ratio N on $|\psi_c|$, $\overline{Nu_h}$, and $\overline{Sh_h}$ are illustrated in Figure 5.13 for $Ra_T = 10^5$, $Le = 10$, and different values of Pe and n. The mass buoyancy force acts in the same direction as the thermal buoyancy one ($N > 0$). For small values of N ($N < 10$) where thermal buoyancy force dominates, $|\psi_c|$, $\overline{Nu_h}$, and $\overline{Sh_h}$ are invariant due to small participation of mass buoyancy force. It is also observed at this point that as Pe increases, the rheological behavior of non-Newtonian fluids is clearly affected especially for shear thickening fluids. Indicating that the moving walls shear force influences fluid flow and heat and mass transfer, which can be confirmed from Fig. 10(d) where the values of y_0 are closer to zero for small values of N as n increases. As the buoyancy ratio keeps rising, the quantities begin to increase slowly at first, owing to the fact that mass buoyancy force starts to take importance; before all quantities increase in a monotonous way as mass buoyancy force fully dominates both thermal one and shear effect of sliding walls. The enhancing role of decreasing n become more pronounced for large values of Pe and the values of y_0 are far from the moving walls (Fig. 10(d)); thus, confirm the increasing contribution of natural regime in overall convection.

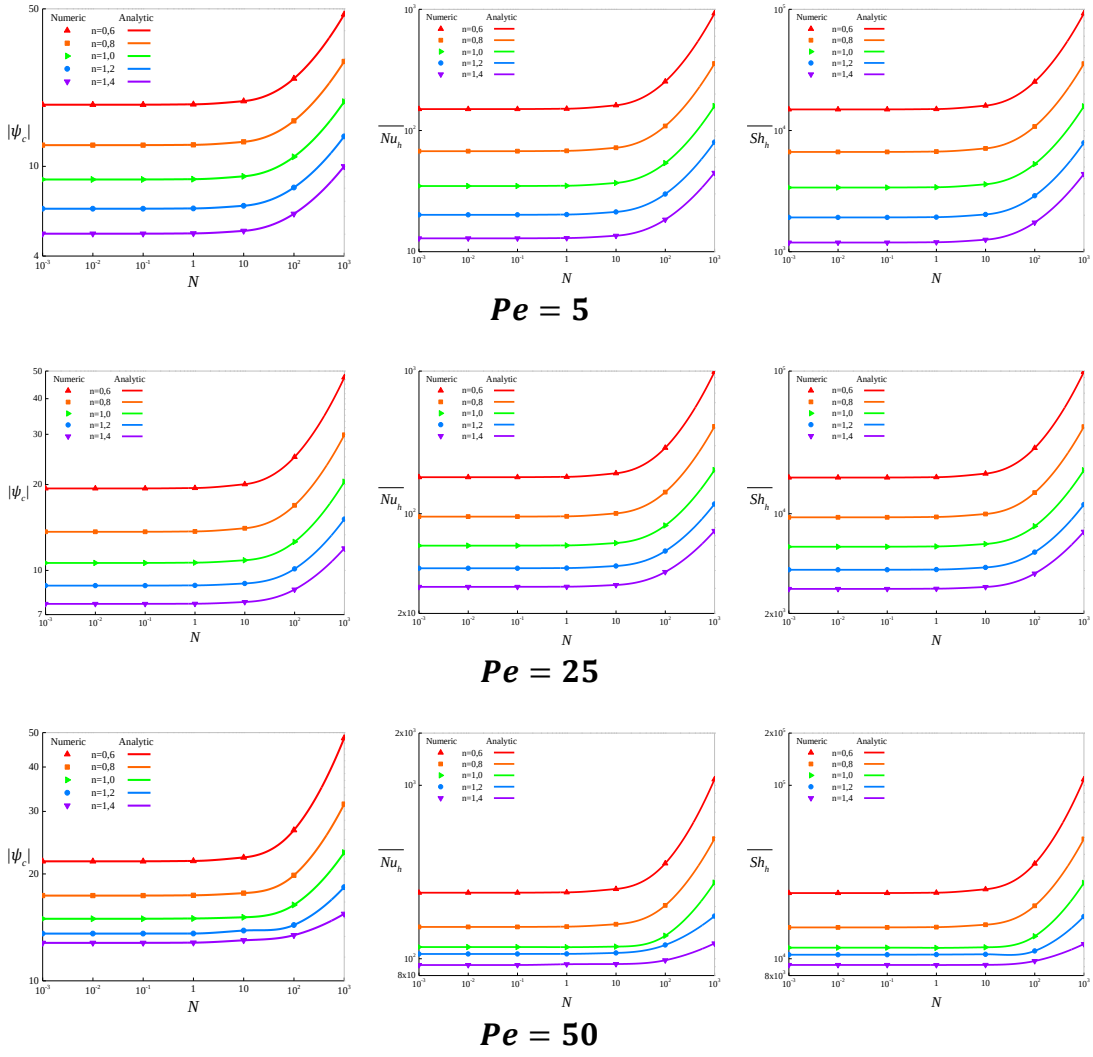

Figure 5.13. Evolutions of the stream function at the center of the cavity $(x = A/2,\ y = 1/2)$ (left), horizontal Nusselt number (middle), and horizontal Sherwood number (right) with buoyancy ratio (N) for $Ra_T = 10^5, Le = 10$, and different values of Pe and n inside double lid-driven cavities.

It's worth to note that mass transfer rate is more important than heat transfer rate because of the difference in diffusion rates as $Le = 10$.

5.11 Horizontal velocity, temperature, and concentration

The horizontal velocity (left), temperature (middle), and concentration (right) profiles, at mid-length of the cavity $\left(x = \frac{A}{2}\right)$, are shown in Figure 5.14 for $Pe = 25$, $Le = 10, N = 1$, and several characteristic values of Ra_T and n. A good agreement between analytical and numerical results is observed. All profiles are separated into symmetrical negative and positive zones due to the symmetry of applied boundary

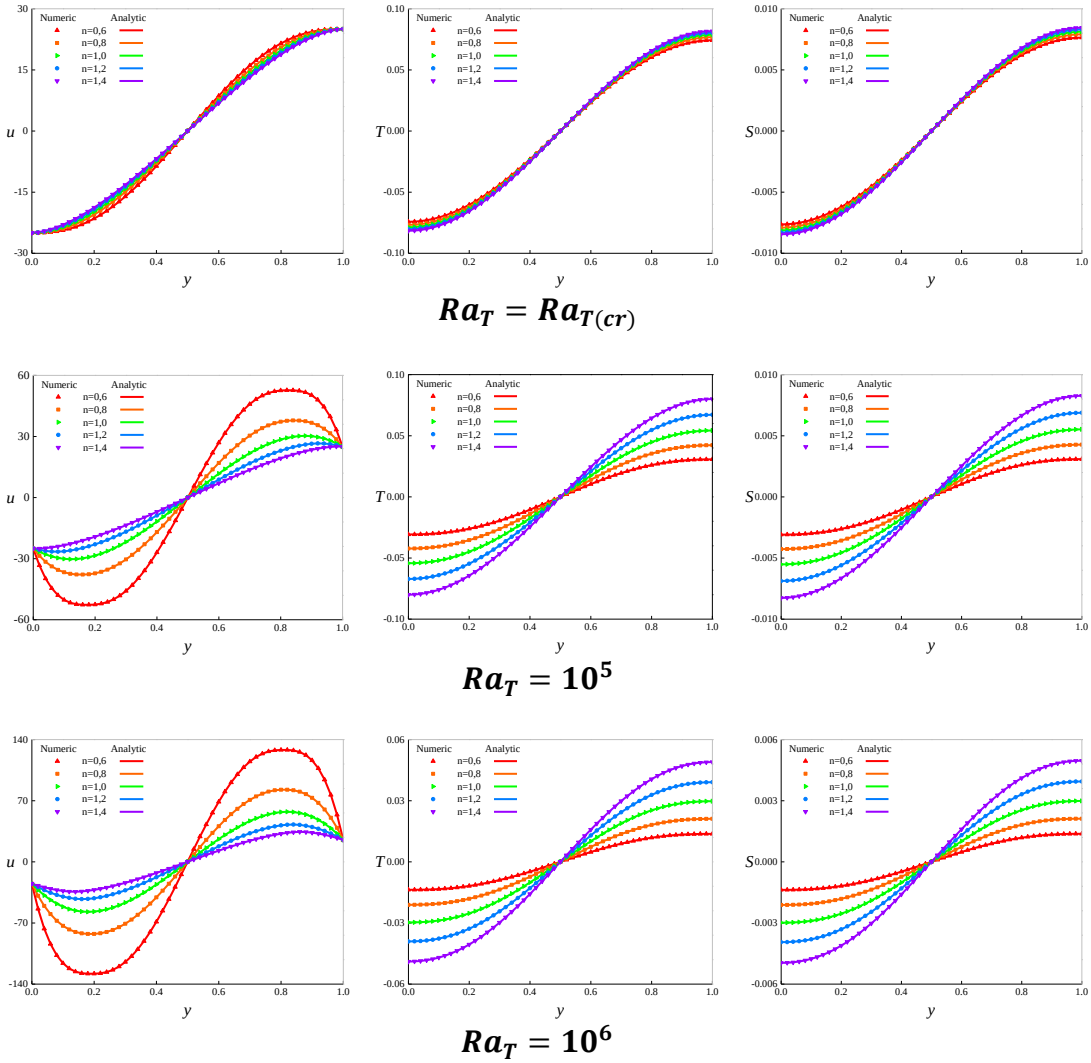

Figure 5.14. Horizontal velocity u (left), temperature T (middle), and concentration S (right) profiles at mid-length of the cavity $(x = A/2)$ along the vertical coordinate (y) for $Pe = 25, Le = 10, N = 1$, and various characteristic values of Ra_T and n inside double lid-driven cavities. $Ra_{T(cr)}$ signals the onset of buoyancy-driven flow.

conditions, which agrees with the monocellular clockwise flow generated by moving walls and buoyancy effect acting in the same direction (from left to right). For the purpose of identifying the contribution of each convective regime in flow inception, we introduced the value $Ra_{T(cr)}$. For this critical value of thermal Rayleigh number, the velocity minimum and maximum are at $y = 0$ and $y = 1$, respectively, which correspond to the moving horizontal walls' velocities. Thus, for $Ra_T \leq Ra_{T(cr)}$, forced convection dominates natural convection due to dominating shear effect, leading to a more intense flow circulation near the driven walls. Furthermore, the profiles of $u, T,$ and S confirm how the forced regime impacts non-Newtonian fluids rheological

behavior influence on flow characteristics as n effect becomes negligible. For higher values of Ra_T $\left(Ra_T > Ra_{T(cr)}\right)$, the two extremums of velocity (maximum and minimum) begin to shift away from the moving walls and become more amplified, which implies that the flow is stronger in that region. Plus, the effect of n becomes more noticeable indicating that the flow becomes buoyancy-driven as natural convection dominates forced convection. The values of $Ra_{T(cr)}$ signalling the shift from shear force-driven flow to buoyancy-driven flow are given in Table 5.6 for different values of n. The value increases with n; thus, delaying the transition to buoyancy-driven flow.

As for temperature profiles, they also show negative and positive zones, where the amplitude depends on Ra_T and n. The clockwise flow makes warm the top of the cavity by transferring heat from the left hot wall, while carrying the coldest fluxes to the bottom after discharging the heat along the right vertical wall. The mass exhibits similar transfer phenomenon to heat; hence, we get similar profiles for concentration.

5.12 Effect of power-law behavior index

Effects of non-Newtonian fluids rheological behavior on flow structure, temperature, and concentration can be inspected from the profiles in Figures 5.4, 5.5, and 5.6 illustrated for $Ra_T = 10^5,\ Le = 10,\ N = 1$, and various values of Pe and n. In the case where natural convection dominates $\left(\frac{Ra_T}{Pe^{\gamma}} > \eta_n\right)$, even though the streamlines do not show changes in the global structure where the flow is unicellular with a parallel aspect in the center of the cavity independently of the value of n, the flow intensifies as n decreases from 1.4 to 0.6 indicating a faster fluid circulation as confirmed by the

Table 5.6 – $Ra_{T(cr)}$ values signaling buoyancy-driven flow onset for $Pe = 25$, $Le = 10, N = 1$ and different values of n inside double lid-driven cavities.

$\boldsymbol{n}$	$\boldsymbol{Ra_{T(cr)}}$
0.6	4117.4967
0.8	8791.4151
1.0	18857.7351
1.2	40589.992
1.4	87595.275

velocity profiles in Figure 5.14 for $Ra_T = 10^5$ and $Ra_T = 10^6$. In contrast, the effects of the rheological behavior on the global structure of isotherms and iso-concentrations are more obvious, where they become less inclined with respect to the vertical direction as n increases. As for temperature and concentration profiles, the absolute values increase as n increases (see Figure 5.14) signaling that the flow loses intensity. Similar outcomes on heat and mass transfer rates are observed where $\overline{Nu_h}$ and $\overline{Sh_h}$ decrease as n increases. Consequently, in dominating natural convection regime, shear thinning behavior ($0 < n < 1$) enhances convection compared to Newtonian case ($n = 1$), while shear thickening behavior ($n > 1$) does the opposite. This can be explained from Eq. (3.25) where increasing n leads to increasing the apparent viscosity of the fluid; thus, the fluid becomes more resistant to motion.

As we begin shifting to mixed convection regime, the effect of n starts to diminish until it totally vanishes when forced convection takes the leading role $\left(\frac{Ra_T}{Pe^{\gamma}} < \eta_f\right)$. At this point, $|\psi_c|$, $\overline{Nu_h}$, and $\overline{Sh_h}$ are invariant as n goes from 0.6 to 1.4 (see Figures 5.9 and 5.11). The same can be confirmed from Figure 5.14 for $Ra_T = Ra_{T(cr)}$ where the velocity, temperature, and concentration profiles are practically identical for different values of n. Thus, for non-Newtonian fluids, the strength of shear force generated by the sliding walls significantly impacts fluids viscosity in a way that results in demolishing the effect of power-law behavior index on convection characteristics observed in natural regime.

5.13 Conclusions

The present chapter studied double-diffusive mixed convection both numerically and analytically in a double lid-driven rectangular cavity filled with non-Newtonian fluids, and subjected to uniform heat and mass fluxes along its vertical short sides while the horizontal moving walls are insulated and impermeable. For shallow enclosures, the flow intensity and heat and mass transfer rates are found to be insensitive to any change in the cavity aspect ratio when $A \geq 24$. Numerical tests also show that for $Pr \geq 10$, varying Prandtl has no effect on flow characteristics. Accordingly, non-Newtonian double-diffusive mixed convection in shallow lid-driven rectangular cavities is mainly controlled by: Péclet number Pe, thermal Rayleigh number Ra_T, Lewis number Le, buoyancy ratio N, and power-law behavior index n. A wide range of these controlling

parameters is examined ($Pe \leq 10^3, Ra_T \leq 5 \times 10^6, 10^{-3} \leq Le \leq 10^3,\ 10^{-3} \leq N \leq 10^3$ and $0.6 \leq n \leq 1.4$) . Numerical results obtained using finite volume and finite difference methods are found to agree perfectly. Both solutions, numerical and analytical, show good agreement within the explored ranges of governing parameters; thus, validating each of the numerical code and the analytical approach.

The dominance regions of each of the three convective regimes, namely natural, mixed, and forced convection are defined for more insight on the effects of governing parameters. The mixed convection parameter $\frac{Ra_T}{Pe^{\gamma}}$, strongly correlated to fluid power-law behavior index, is used to delineate the three regimes. The following bounds delimit the mixed convection regime for $Le = 1$ and $N = 1$, while natural and forced convection are found to be dominant outside these limits:

$$0.0259 < \frac{Ra_T}{Pe^{2.6}} < 452.21;\ 0.0299 < \frac{Ra_T}{Pe^{3.0}} < 7085;\ 0.0225 < \frac{Ra_T}{Pe^{3.4}} < 86710$$

for $n = 0.6, n = 1.0,$ and $n = 1.4,$ respectively. Accordingly, in natural convection predominance area, the behavior index affects strongly fluid flow and heat and mass transfer, as shear-thinning behavior enhances convection compared to Newtonian case, while shear-thickening behavior reduces it. In contrast, for forced convection dominance region, the strong shear force due to dominating effect of moving walls affects fluid viscosity, leading to eliminate the power-law behavior index effect on flow characteristics observed in natural regime. As for the outcome on flow characteristics, increasing Péclet number or thermal Rayleigh number increases fluid circulation and heat and mass transfer rates. The first promotes the contribution of forced convection (higher shear effect) while the second enhances natural convection input in overall convection (higher buoyancy force), resulting in both cases in a more active convection.

Increasing Lewis number strongly enhances mass transfer while no effect is noticed on flow intensity and heat transfer. Furthermore, increasing Le is found to promote the contribution of forced regime in overall convection, especially as the power-law index increases. Regarding buoyancy ratio effects, increasing it enhances fluid flow and heat and mass transfer as a beneficial result of dominant mass buoyancy force which improves natural convection contribution. In contrast, decreasing N leads to a more dominating forced regime due to small contribution of mass buoyancy force, which becomes more obvious for shear-thickening fluids.

CHAPTER 6 Rayleigh-Bénard Double-Diffusive Mixed Convection in Double Lid-Driven Rectangular Cavities Filled with Non-Newtonian Fluids

6.1 Introduction

Double-diffusive mixed convection in the famous Rayleigh-Bénard configuration is investigated in the present chapter. Rectangular cavities (Fig. 6.1) filled with non-Newtonian fluids are subjected to uniform heat and mass fluxes along the sliding horizontal walls, while the vertical ones are considered insulated and impermeable ($a = c = 1 \; and \; b = d = 0$). The horizontal walls continuously slide in opposite directions with the same uniform velocity u_0' ($e = 1$), while the vertical ones are motionless. Taking into account the singularity and complexity of Rayleigh-Bénard convection, this chapter results can lead to new findings regarding mixed non-Newtonian fluids flow and heat and mass transport given all the involved driving factors.

As before, Numerical trial-and-error tests show that for $Pr \geq 10$, mixed convection flow characteristics become independent of Prandtl number. As for the grid size, numerical results show that for $A = 28$ (value after which the results become independent of the cavity aspect ratio A), a uniform mesh size of 320×80 allows to accurately simulate the flow problem. The agreement between the analytical approach based on the parallel flow approximation and the numerical code can be gained from comparing numerical and analytical results for inclusive ranges of governing parameters in what follows. The effects of said parameters on fluid flow and heat and mass transfer characteristics are discussed in light of the dominant convective regime, namely natural, mixed, or forced convection.

6.2 Value of A satisfying the large aspect ratio approximation

Figure 6.2 illustrates the variations of $\overline{Nu_v}$ with A for $Ra_T = 10^4$, $Le = 10$, $N = 1$ and several values of Pe and n. $\overline{Nu_v}$ reaches an asymptotic state as the aspect ratio keeps increasing; we also notice, as in the previous chapter, the forced regime

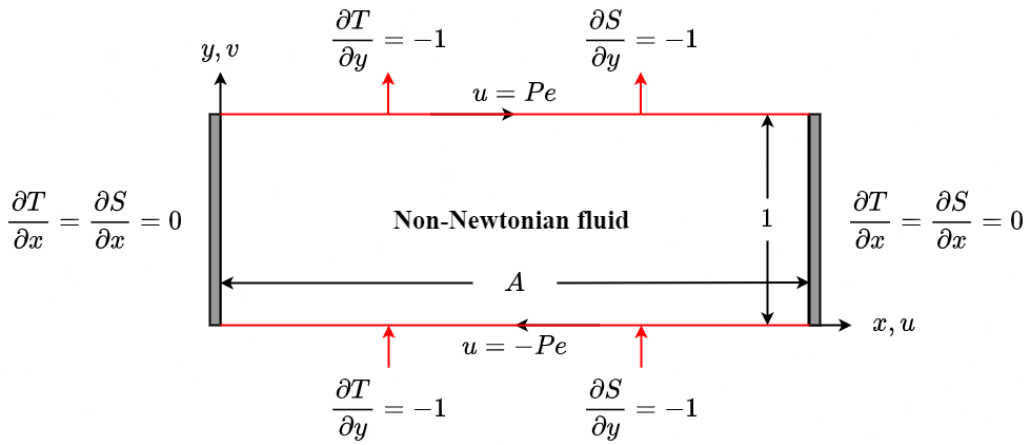

Figure 6.1. Physical model of the investigated configuration along with coordinate system and associated boundary conditions. The horizontal walls are subjected to uniform density of heat and mass fluxes and move in opposite directions with the same uniform velocity, while the vertical boundaries are motionless, insulated, and impermeable.

($Pe = 200$) retarding role as it delays the reach of such asymptotic state compared to natural and mixed regimes. The figure shows that $A = 28$ is the smallest value that leads to numerical results independent of the cavity aspect ratio and in good agreement with analytical results, and that for different values of governing parameters. This value reduces to $A = 24$ in the case of applied horizontal heat and mass fluxes as shown in chapter 5 signifying that Rayleigh-Bénard configuration delays reaching the asymptotic state which can be attributed to the nature of applied thermal and solutal boundary conditions.

Consequently, Rayleigh-Bénard double-diffusive mixed convection is mainly governed by: Péclet number Pe, thermal Rayleigh number Ra_T, Lewis number Le, buoyancy ratio N, and power-law behavior index n. The effects of said parameters on fluids flow and heat and mass transport phenomena are investigated in details for three separate convective regimes: natural, mixed, and forced convection.

6.3 Mixed convection parameter

The same numerical procedure discussed before is adopted to separate the dominance regions of natural, mixed, and forced convection regimes. The results are illustrated in Figure 6.3 where a good agreement can be seen between both solutions, numerical and

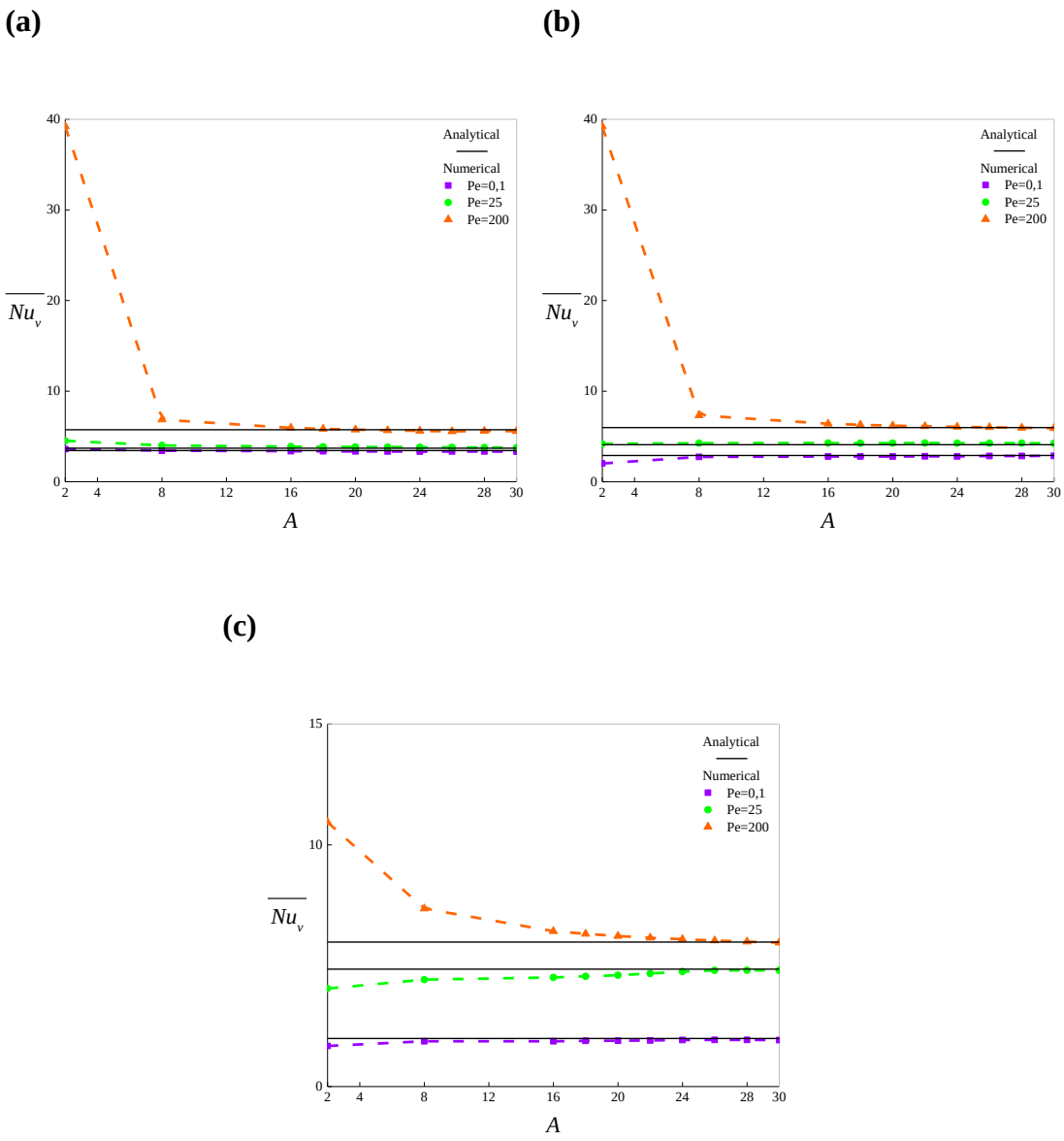

Figure 6.2. Variation of numerical vertical Nusselt number $(\overline{Nu_v})$ with the cavity aspect ratio $\left(A = \frac{L'}{H'}\right)$ while varying Péclet number (Pe) to account for the different convective regimes (natural, mixed, and forced convection) for: (a) pseudoplastic fluid $(n = 0.6)$, (b) Newtonian fluid $(n = 1.0)$, and (c) dilatant fluid $(n = 1.4)$ at $Ra_T = 10^4, Le = 10, \text{and } N = 1$ inside double lid-driven Rayleigh-Bénard configuration.

analytical. The separating limits can be written in the form of mixed convection parameter as follows:

- For $n = 0.6$:

$$\frac{Ra_T}{Pe^{1.57}} = \eta_n \text{ and } \frac{Ra_T}{Pe^{1.57}} = \eta_f \quad (6.1)$$

- For $n = 1.0$:

$$\frac{Ra_T}{Pe^{1.92}} = \eta_n \text{ and } \frac{Ra_T}{Pe^{1.92}} = \eta_f \tag{6.2}$$

- For $n = 1.4$:

$$\frac{Ra_T}{Pe^{2.27}} = \eta_n \text{ and } \frac{Ra_T}{Pe^{2.27}} = \eta_f \tag{6.3}$$

describing the limits for dominant natural and dominant forced regimes, respectively. Similar to chapter 5, it is obvious that the fluid rheological behavior plays a key role in characterizing the dominant convective regime as coefficient γ increases with the power-law behavior index. The ratios η_n and η_f are given in Table 6.1 and shown in Figure 6.3 with dashed lines for different values of n. Thus, for $Le = 1$ and $N = 1$, double-diffusive mixed convection regime within double-lid driven rectangular cavities subjected to uniform heat and mass fluxes along the horizontal walls and filled with non-Newtonian fluids is bounded as follows:

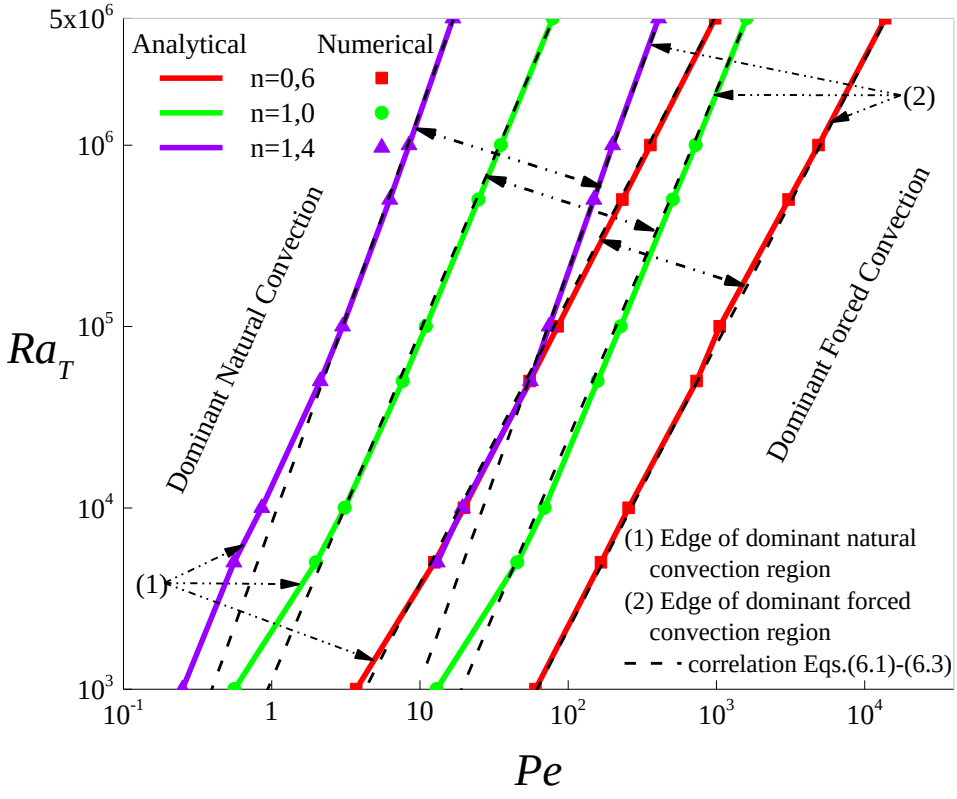

Figure 6.3. Natural, forced, and mixed convection dominance regions with pseudoplastic ($n = 0.6$), Newtonian ($n = 1.0$), and dilatant ($n = 1.4$) working fluids for $Le = 1$ and $N = 1$ inside double lid-driven Rayleigh-Bénard configuration.

Table 6.1 – Correlation coefficients η_n and η_f for characteristic values of n in Rayleigh-Bénard configuration.

Power-law behavior index n	Natural convection η_n	Forced convection η_f
0.6	102.19	1.54
1.0	1121.21	3.46
1.4	8203.57	5.80

$$1.54 < \frac{Ra_T}{Pe^{1.57}} < 102.19;\ 3.46 < \frac{Ra_T}{Pe^{1.92}} < 1121.21;\ 5.80 < \frac{Ra_T}{Pe^{2.27}} < 8203.57 \tag{6.4}$$

for $n = 0.6, n = 1.0,$ and $n = 1.4$, respectively.

The minor deviations of the separating limits from the straight correlating lines are observed for low values of Pe and Ra_T, especially for higher values of power-law index ($n = 1.4$) which corresponds to a feeble convection regime. Such deviations can be attributed to a change in the transport mechanism.

6.4 Dynamical, thermal, and solutal structures

Illustrative streamlines (top), isotherms (middle), and iso-concentrations (bottom) are presented in Figures 6.4, 6.5, and 6.6 for $Ra_T = 10^4, Le = 10, N = 1$, and different values of Pe and n. Here again, similar observations to the case of applied horizontal uniform heat and mass fluxes can be made. The flow is unicellular and clockwise, where except for regions near the cavity vertical boundaries at which the flow experiences a rotation of 180°, the streamlines display a parallel behavior within the enclosure. As for the isotherms and iso-concentrations, they show a linear stratification in the x-direction where they become more inclined with respect to the vertical direction as the fluid behavior shifts from dilatant to pseudoplastic or while increasing Péclet number, signaling that convection strengthens leading to enhance fluid flow and heat and mass transfer rates. It is worth to note that given the high diffusion rate of concentration compared to that of heat ($Le = 10$), mass transfer is more important than heat transfer explaining the iso-concentrations' higher inclination compared to isotherms.

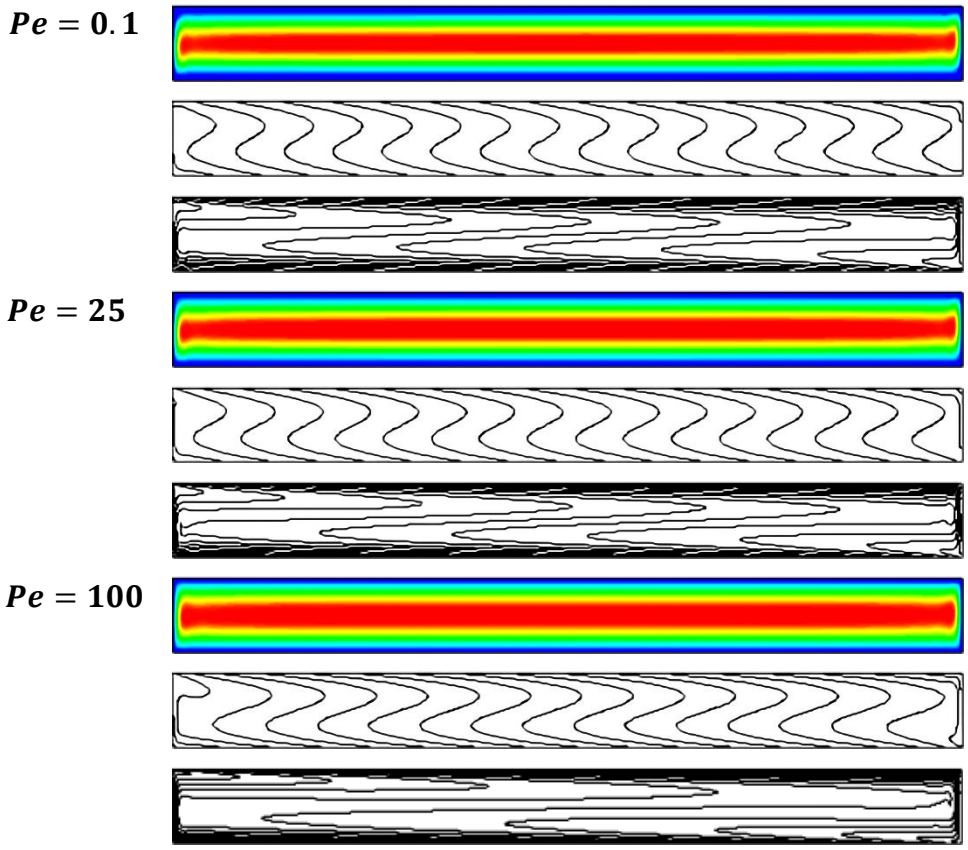

Figure 6.4. Streamlines (top), isotherms (middle), and iso-concentrations (bottom) while varying Péclet number (Pe) for a pseudoplastic fluid ($n = 0.6$) at $A = 28, Ra_T = 10^4$, $Le = 10$ and $N = 1$ inside double lid-driven Rayleigh-Bénard configuration. (Scale not respected).

The effects of shear force magnitude on the three profiles are also displayed in terms of Pe value. For low values of Péclet number, indicating feeble shear force, the contours are similar to the ones obtained for pure natural convection regime (see Figure 6.7). No fluid circulation is induced by the moving walls as the streamlines shift away from the horizontal boundaries indicating that fluid flow is buoyancy-driven with dominating natural regime $\left(\frac{Ra_T}{Pe^{\gamma}} > \eta_n\right)$. As Pe keeps increasing, the streamlines get more crowded near the sliding horizontal walls as the fluid circulation intensifies in that region, meaning that forced convection contributes to the overall convective regime. Such change occurs first for dilatant fluids, as increasing n weakens natural convection flow and heat and mass transfer characteristics; hence, accelerates the transition from natural to mixed regime. For higher values of Pe, the streamlines are packed near the horizontal

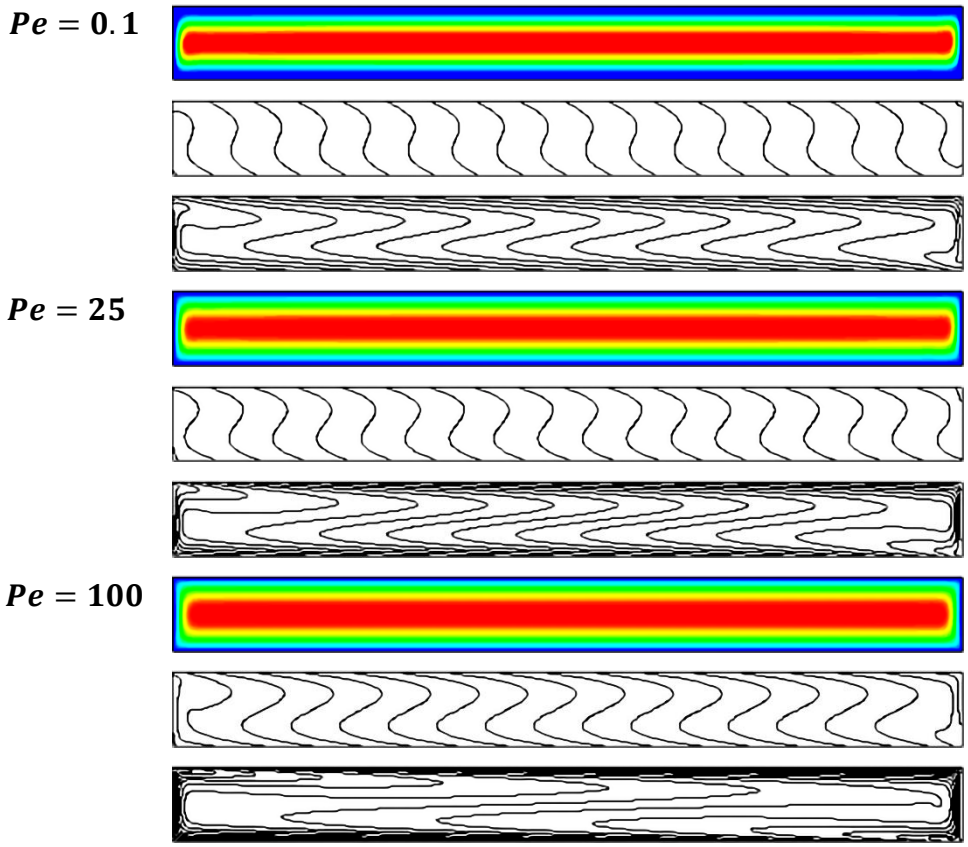

Figure 6.5. Streamlines (top), isotherms (middle), and iso-concentrations (bottom) while varying Péclet number (Pe) for a Newtonian fluid ($n = 1.0$) at $A = 28$, $Ra_T = 10^4$, $Le = 10$ and $N = 1$ inside double lid-driven Rayleigh-Bénard configuration. (Scale not respected).

boundaries indicating strong fluid circulation due to moving walls, while isotherms and iso-concentrations are practically linear within the cavity. These observations match the profiles found in pure forced convection regime as shear force dominates buoyancy force $\left(\frac{Ra_T}{Pe^Y} < \eta_f\right)$ (see Figure 6.8).

Finally, temperature and concentration fields show that as n decreases or Pe increases, boundary layers appear near the cavity walls with growing width indicating strong temperature and concentration gradients in that region. This is more noticeable in the case of iso-concentrations given the concentration higher diffusion rate ($Le > 1$).

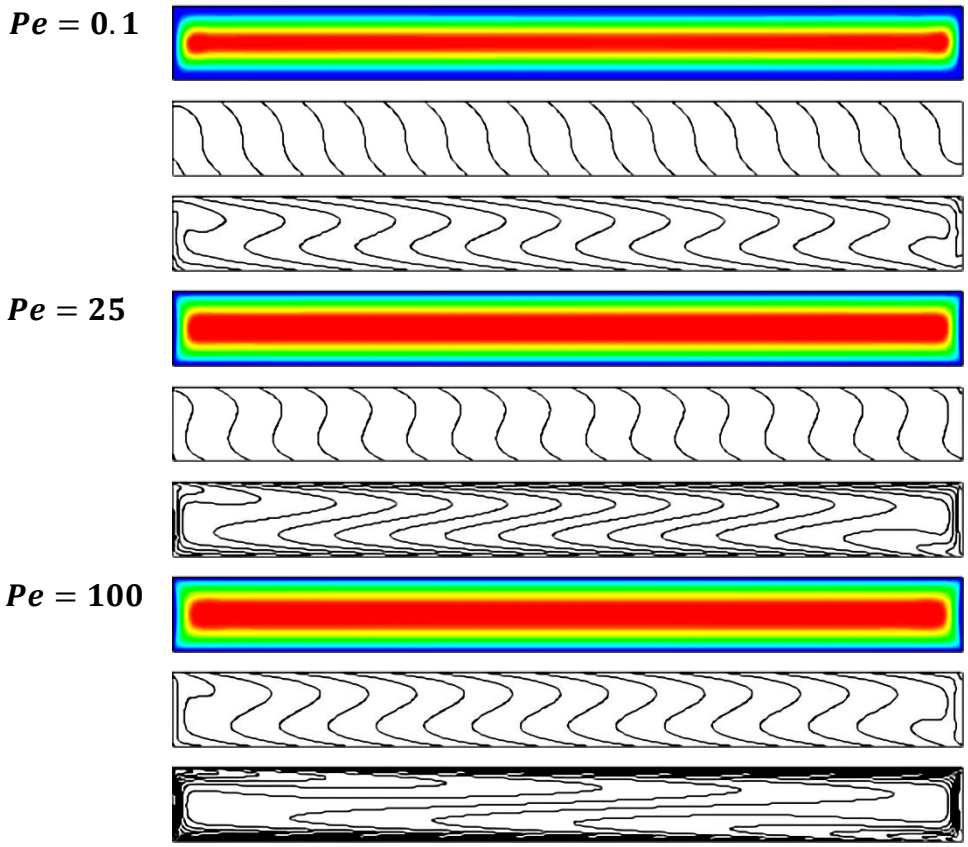

Figure 6.6. Streamlines (top), isotherms (middle), and iso-concentrations (bottom) while varying Péclet number (Pe) for a dilatant fluid ($n = 1.4$) at $A = 28, Ra_T = 10^4$, $Le = 10$ and $N = 1$ inside double lid-driven Rayleigh-Bénard configuration. (Scale not respected).

6.5 Effect of Péclet number

The variations of $|\psi_c|$, $\overline{Nu_v}$, and $\overline{Sh_v}$ with Péclet number Pe are shown in Figure 6.9 for $Le = 10$, $N = 1$, and different values of Ra_T and n. At first, increasing Péclet number does not affect flow characteristics as the shear force input is insignificant (low Pe values) when compared to the effect of buoyancy force. Such conclusion can be confirmed from the range of Pe values for which the flow characteristics are invariant, as it increases while strengthening the buoyancy force by increasing Ra_T or by decreasing the power-law index n given its well-established effect on intensifying natural convection flow characteristics. Furthermore, the results match the ones obtained in the case of pure natural convection portrayed with dashed lines. All these observations confirm that natural convection dominates the convective regime. After a

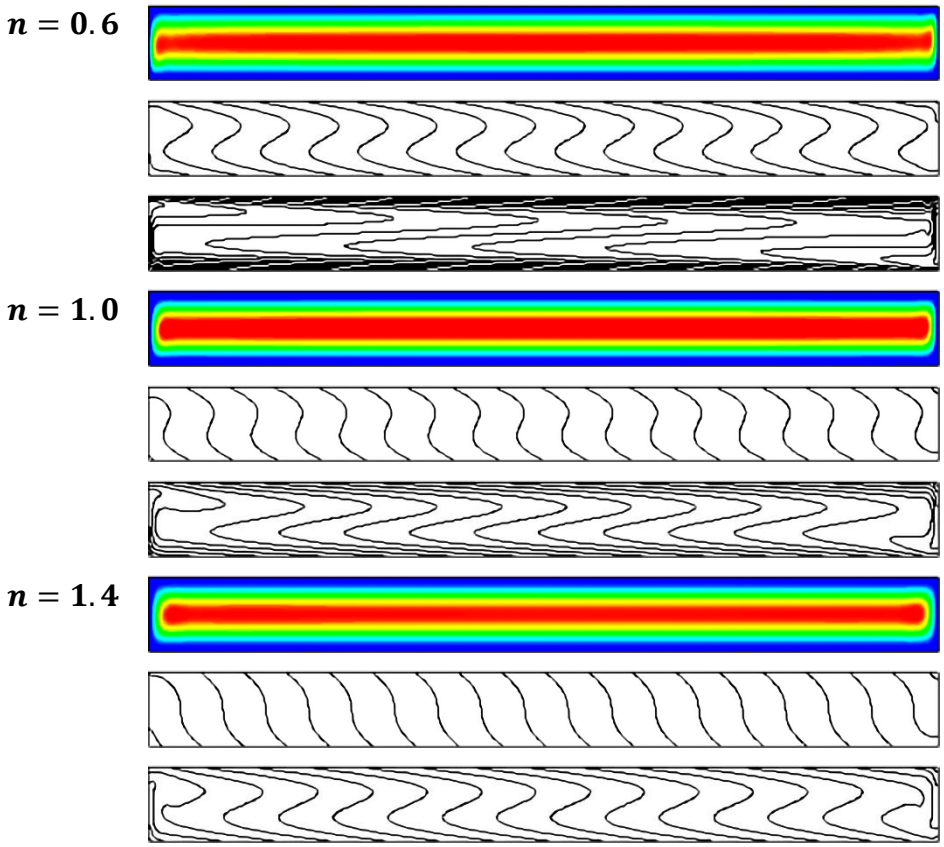

Figure 6.7. Streamlines (top), isotherms (middle), and iso-concentrations (bottom) for pure natural convection at $A = 28,\ Ra_T = 10^4, Le = 10,$ and $N = 1$. The results are illustrated for the three fluid behaviors: pseudoplastic ($n = 0.6$), Newtonian ($n = 1.0$), and dilatant ($n = 1.4$) inside double lid-driven Rayleigh-Bénard configuration. (Scale not respected).

given value of Pe, the flow characteristics start to rise slowly indicating that the regime shifts from dominant natural to mixed convection as the shear force, generated by the moving walls, starts to contribute to the overall convection. The Pe value initiating such transition can be defined by $\left(\frac{Ra_T}{\eta_n}\right)^{1/\gamma}$, confirming what we mentioned before as increasing Ra_T or decreasing n delays the transition where higher values of Pe (higher shear force) are needed to make the shift. As Pe keeps increasing, $\overline{Nu_v}$ and $\overline{Sh_v}$ display interesting results. Unlike the natural regime where pseudoplastic fluids ($0 < n < 1$) enhance convection compared to Newtonian fluid while dilatant fluids ($n > 1$) diminish it, opposite effects are observed as dilatant fluids enhance convection while pseudoplastic fluids reduce it, such effects become more pronounced while Ra_T

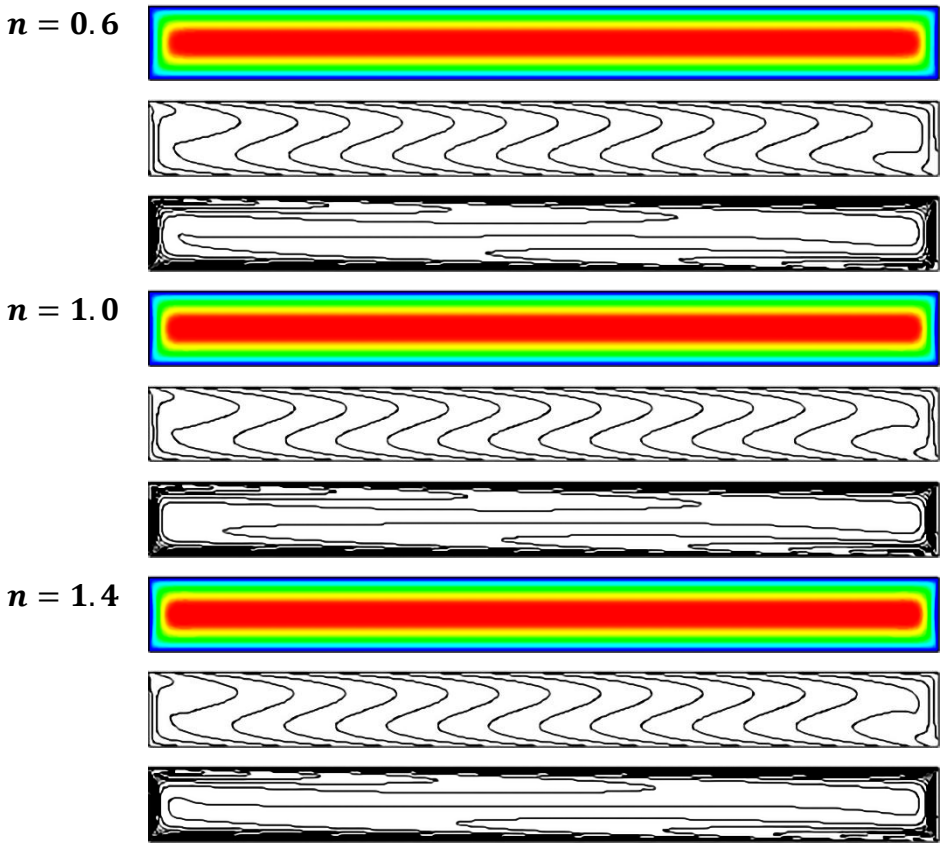

Figure 6.8. Streamlines (top), isotherms (middle), and iso-concentrations (bottom) for pure forced convection ($Ra_T = 0$) at $A = 28$, $Pe = 150, Le = 10,$ and $N = 1$. The results are illustrated for the three fluid behaviors: pseudoplastic ($n = 0.6$), Newtonian ($n = 1.0$), and dilatant ($n = 1.4$) inside double lid-driven Rayleigh-Bénard configuration. (Scale not respected).

increases. For high values of Pe, flow intensity increases in a monotonous way while $\overline{Nu_v}$ and $\overline{Sh_v}$ first increase rapidly before reaching a higher plateau where they become constant. The results match the ones obtained for pure forced convection, shown with dashed lines, given that shear force dominates buoyancy force leading to fluid flow and heat and mass transfer mainly ensured by forced convection.

Introducing shear force to the convective regime leads to some unforeseen consequences on the effect of non-Newtonian fluids behavior. As Pe increases, mixed convection regime dominates and the effect is reversed as shear thickening fluids strengthens convection compared to Newtonian fluid while the opposite is observed for shear thinning fluids. Such change can be attributed to the delaying role of decreasing

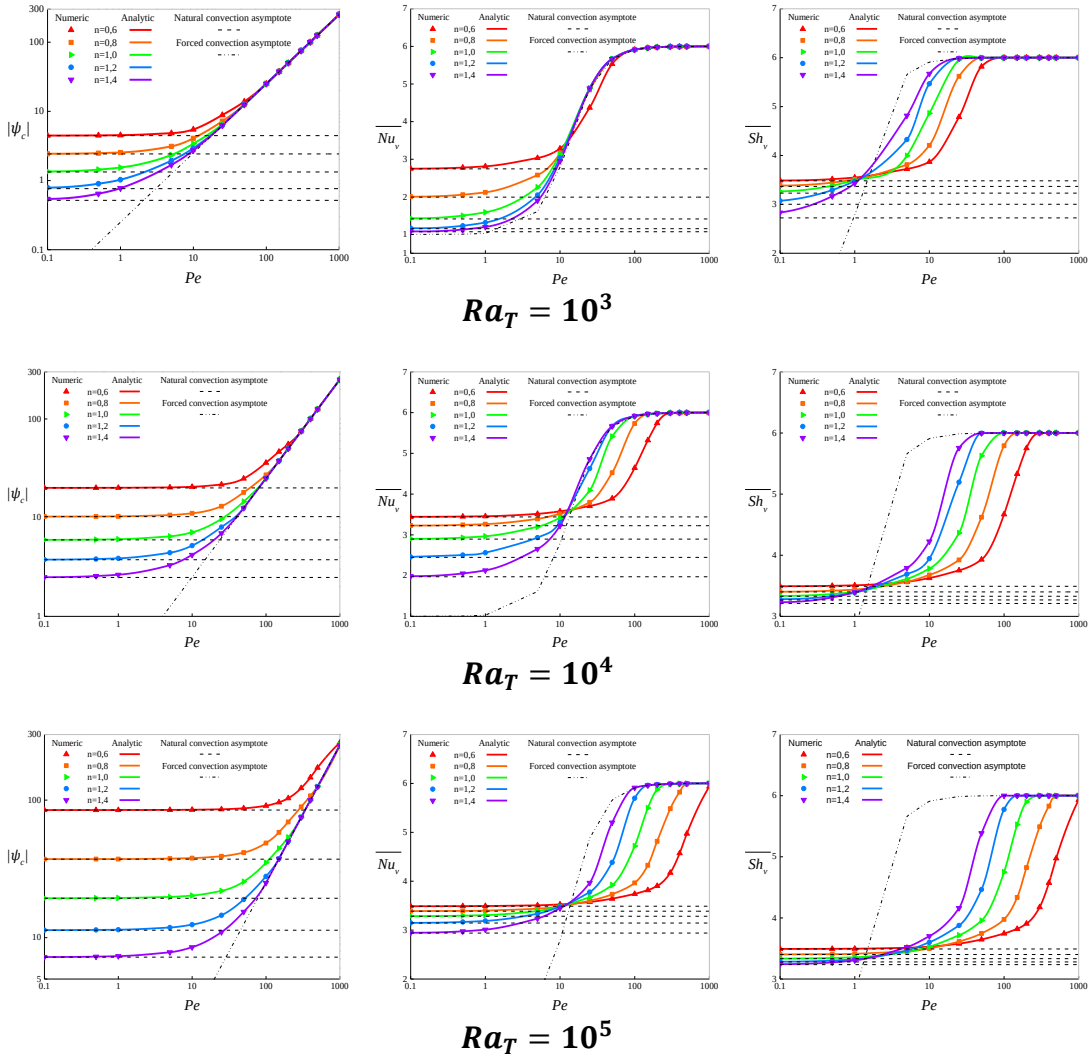

Figure 6.9. Variations of the stream function at the center of the cavity $(x = A/2,\ y = 1/2)$ (left), vertical Nusselt number (middle), and vertical Sherwood number (right) with Péclet number Pe for $Le = 10, N = 1$, and various values of Ra_T and n inside double lid-driven Rayleigh-Bénard configuration.

n on the transition from natural to mixed regime, as shear thickening fluids are the first to make the shift while shear thinning fluids transition is delayed owing to associated strong natural convection, especially as buoyancy force strengthens while increasing Ra_T. Hence, strengthening natural regime suppresses the enhancing role of moving walls where higher shear force (higher Pe values) is needed to influence flow characteristics (mixed regime), leading to the observed change in the effect of non-Newtonian fluids behavior. For high values of Pe, forced convection dominates $\left(\frac{Ra_T}{Pe^{\gamma}} < \eta_f\right)$ and the effect of power-law index keeps diminishing until it totally

vanishes denoting that the dominating convective regime changes how non-Newtonian fluids rheological behavior influences convection heat and mass transfer.

The previous conclusions regarding Pe effect can be further confirmed from Figure 6.10(a) showing that as Pe increases, the value of y_0 decreases until it reaches zero signaling that moving walls effect dominates the overall convection. The shear thickening fluids are more sensitive to small variations of Péclet number compared to shear thinning ones that necessitate higher Pe values to reach the forced regime as established by y_0 values and confirmed from Figure 6.3.

6.6 Effect of thermal Rayleigh number

The effects of thermal Rayleigh number Ra_T on flow characteristics $|\psi_c|$, $\overline{Nu_v}$, and $\overline{Sh_v}$ are shown in Figure 6.11 for $Le = 10, N = 1$, and different values of Pe and n. The figures can be separated into three regimes; first, increasing Ra_T or varying the fluid power-law index have no significant effects on the investigated quantities, especially as the intensity of shear force increases with Pe. Moreover, the results agree with the ones obtained in pure forced convection presented with dashed lines, which clearly indicates that forced regime dominates the overall convection. The extent of such dominance depends on Pe and n values, where it increases with Péclet number due to higher shear force and reduces with decreasing power-law index due to its role in intensifying natural convection characteristics resulting in pseudoplastic fluids being the first to leave the dominant forced regime. As Ra_T keeps increasing; on the one hand, $|\psi_c|$ increases slowly denoting a change in the convective regime as we shift from dominant forced convection to mixed one (the value of Ra_T signaling the shift can be correlated by $(\eta_f . Pe^{\gamma})$). The flow intensity finally increases in a monotonous way and joins the results obtained for pure natural convection (dashed lines) indicating that natural regime dominates. On the other hand, the effects of thermal Rayleigh number on $\overline{Nu_v}$ and $\overline{Sh_v}$ are more complicated. For low values of Pe ($Pe = 0.1$) indicating feeble shear force, the enhancing role of increasing Ra_T on Nusselt and Sherwood numbers is obvious as both quantities increase owing to the rising contribution of buoyancy force, before finally reaching a higher plateau where further intensifying the buoyancy force does not improve transfer rates. Here the fluid rheological behavior is not affected as decreasing n enhances flow characteristics. For higher values of

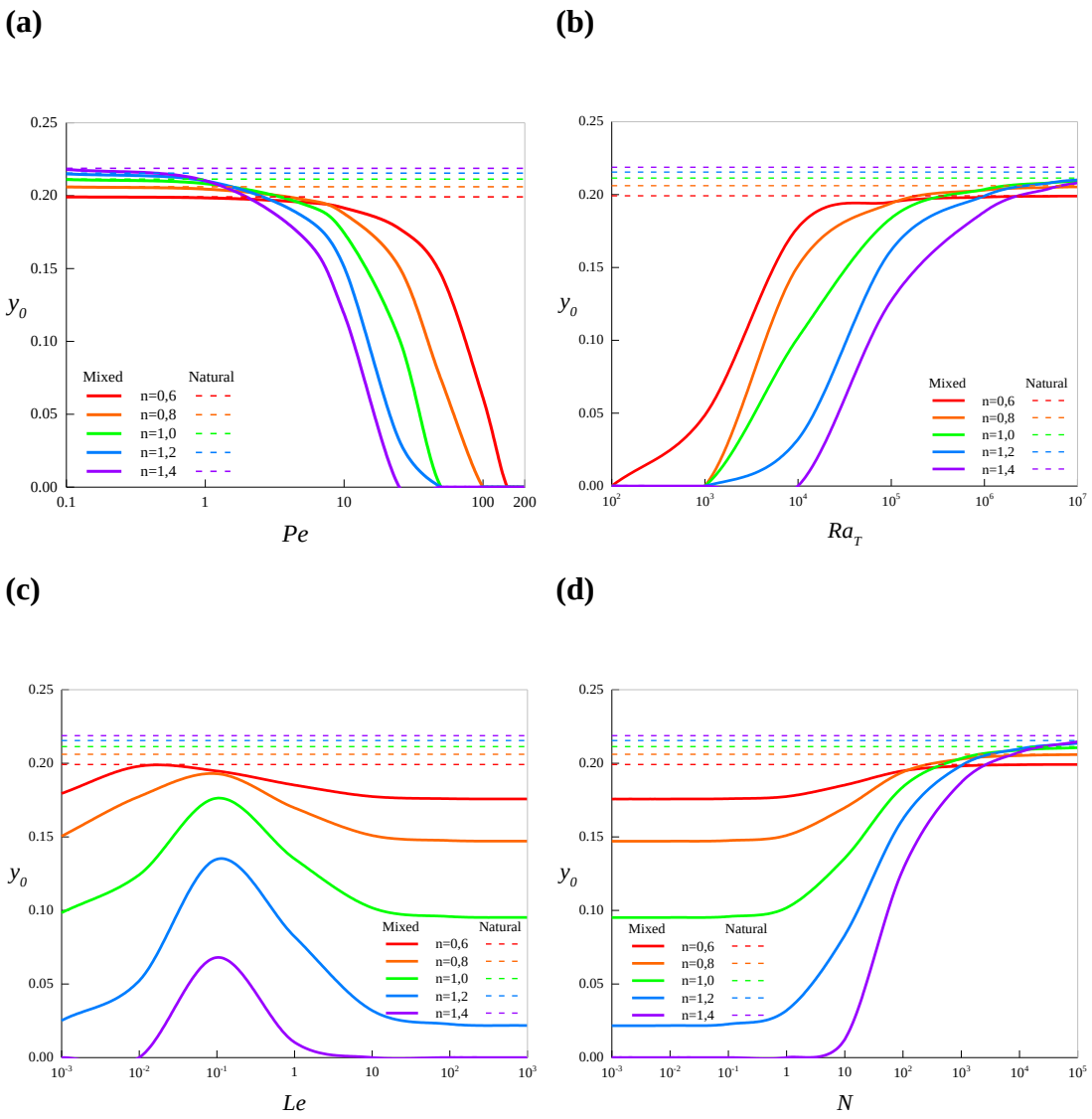

Figure 6.10. Effects of governing parameters on y_0 values (defining the vertical distance between the point with maximum velocity and the sliding wall) considering Rayleigh-Bénard configuration: (a) effect of Pe $(Ra_T = 10^4, Le = 10, N = 1)$, (b) effect of Ra_T $(Pe = 25, Le = 10, N = 1)$, (c) effect of Le $(Pe = 25, Ra_T = 10^4, N = 1)$, and (d) effect of N $(Pe = 25, Ra_T = 10^4, Le = 10)$ all for different values of n.

Pe ($Pe \geq 25$ for $\overline{Nu_v}$ and $Pe \geq 5$ for $\overline{Sh_v}$), the enhancing roles of increasing Ra_T and decreasing n are inverted. For low Ra_T values characterizing a dominant forced convection, $\overline{Nu_v}$ and $\overline{Sh_v}$ start from upper plateaus given the strength of shear force where the plateaus elevations increase with Pe while the effect of n vanishes along such plateaus. As Ra_T increases, Nusselt and Sherwood numbers start to decrease indicating

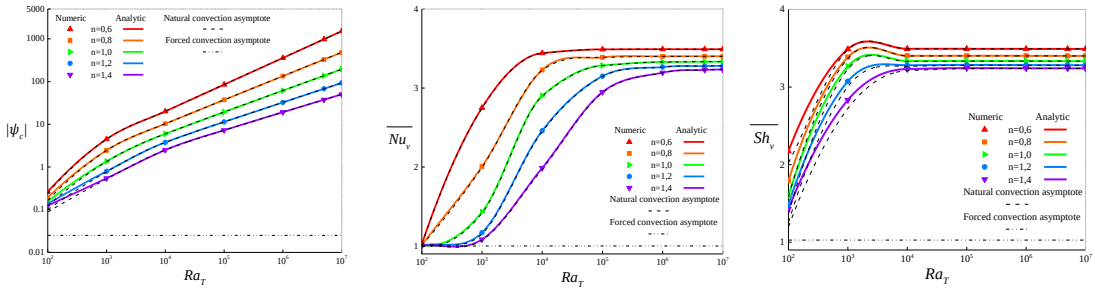

$\boldsymbol{Pe = 0.1}$

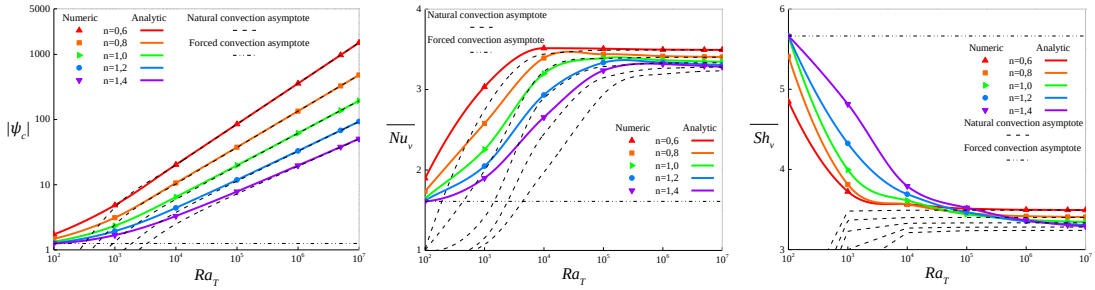

$\boldsymbol{Pe = 5}$

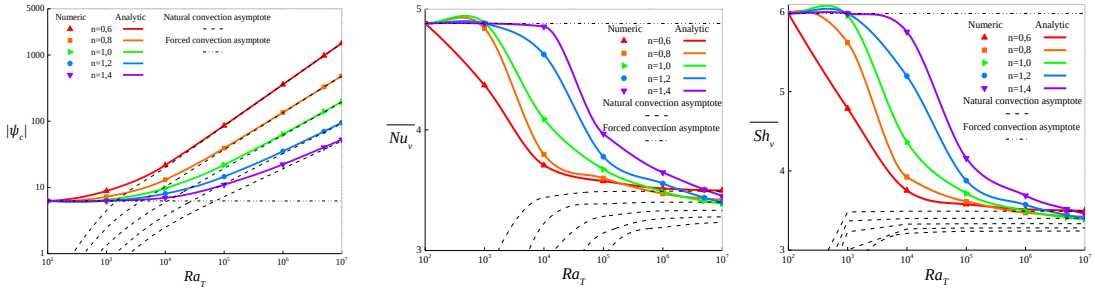

$\boldsymbol{Pe = 25}$

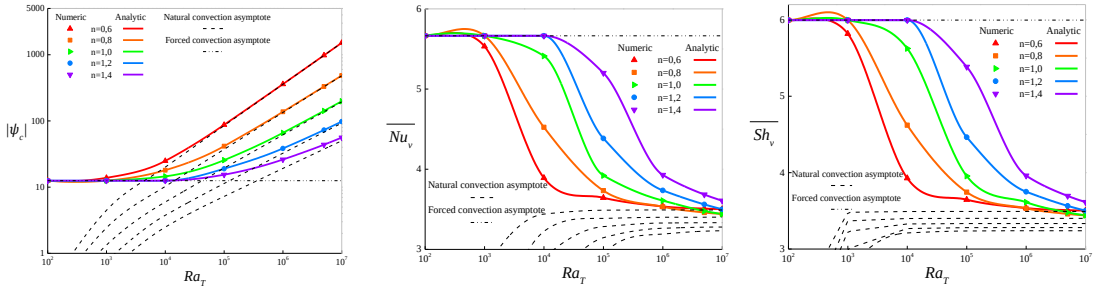

$\boldsymbol{Pe = 50}$

Figure 6.11. Variations of the stream function at the center of the cavity $(x = A/2,\ y = 1/2)$ (left), vertical Nusselt number (middle), and vertical Sherwood number (right) with thermal Rayleigh number Ra_T for $Le = 10, N = 1$, and various values of Pe and n inside double lid-driven Rayleigh-Bénard configuration.

that strengthening buoyancy force hurts heat and mass transport instead of enhancing them. The effect of n is similar to what we observed in the section before for the mixed regime, where dilatant fluids ($n > 1$) enhance convection compared to pseudoplastic ones ($0 < n < 1$). Finally, for high values of Ra_T, the natural convection regime dominates and heat and mass transfer rates become constant as the results reach a lower plateau and match the results obtained in the case of pure natural regime $\left(\frac{Ra_T}{Pe^{\gamma}} > \eta_n\right)$. Pseudoplastic fluids are the first to reach the dominant natural regime where the rheological behavior finds its classical role as decreasing n enhances convection characteristics. These observations confirm the conclusions made in the section above, as the dominating regime changes the way non-Newtonian fluids rheological behavior influences heat and mass transfer with a critical value of Péclet number Pe_{cr} after which the effect of decreasing n on enhancing transfer rates is reversed (which will be defined and discussed later). Plus, for $Pe > Pe_{cr}$, enhancing buoyancy force leads to the undesired effect of reducing heat and mass transfer. The value of Pe_{cr} is affected by the difference in diffusion rate between temperature and concentration gradients as Figure 6.11 shows ($\overline{Nu_v}$, and $\overline{Sh_v}$ profiles for $Pe = 5$).

The dominant convective regime changes are well confirmed by the variations of y_0 with Ra_T given in Figure 6.10(b). The y_0 value increases from zero to a value close to the one obtained in the case of pure natural convection while thermal Rayleigh number increases, indicating the shift from dominant forced to dominant natural regime via the mixed regime. The figure also confirms that shear thinning fluids are the first to leave the dominant forced regime and first to reach the dominant natural convective regime compared to shear thickening fluids.

6.7 Effect of Lewis number

The variations of quantities $|\psi_c|, \overline{Nu_v}$, and $\overline{Sh_v}$ with Lewis number Le are given in Figure 6.12, for $Ra_T = 10^4, N = 1$, and different values of Pe and n. For flow intensity, we can distinguish between three phases; first, a lower plateau is observed for small values of Le with the plateau elevation increasing as n decreases. Second, fluid circulation reaches a peak value with the position shifting right and the amplitude decreasing as fluid behavior changes from pseudoplastic to dilatant. Finally, a second lower plateau for high values of Lewis number with the same elevation as the first

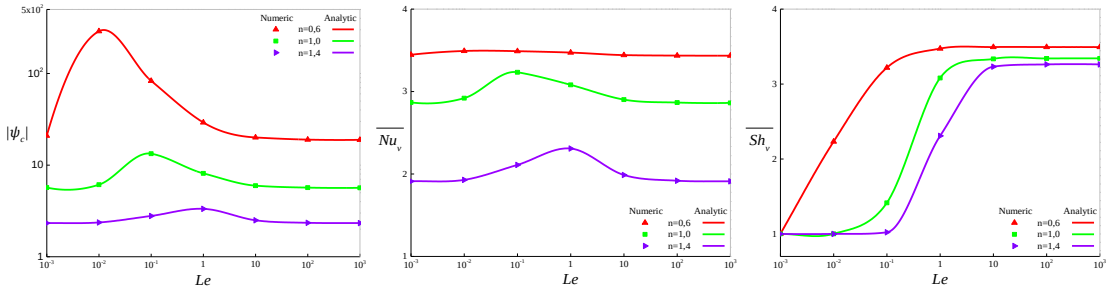

$\boldsymbol{Pe = 0.1}$

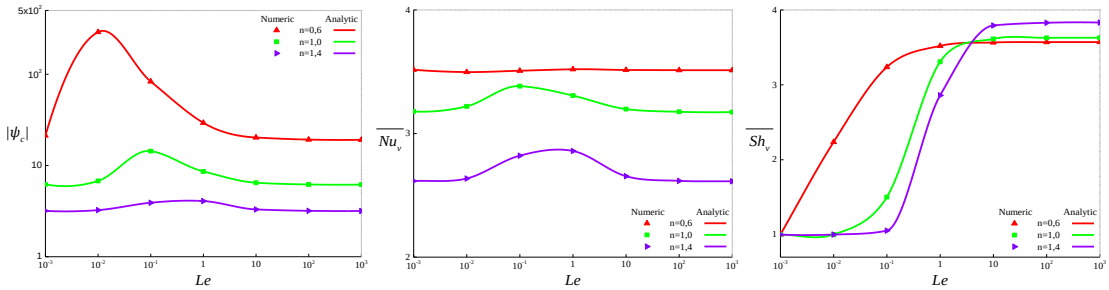

$\boldsymbol{Pe = 5}$

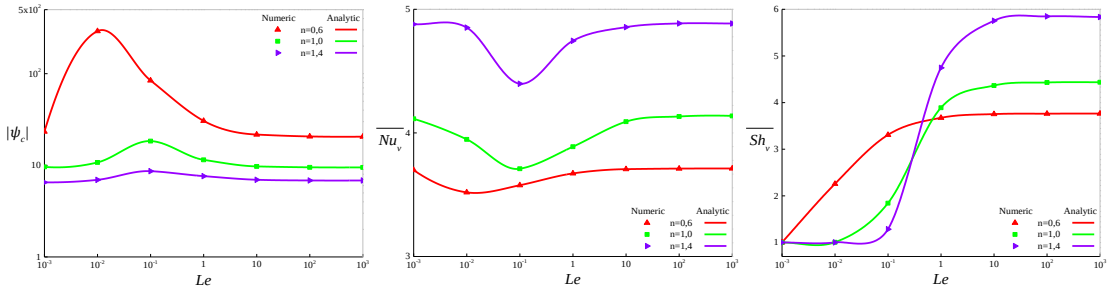

$\boldsymbol{Pe = 25}$

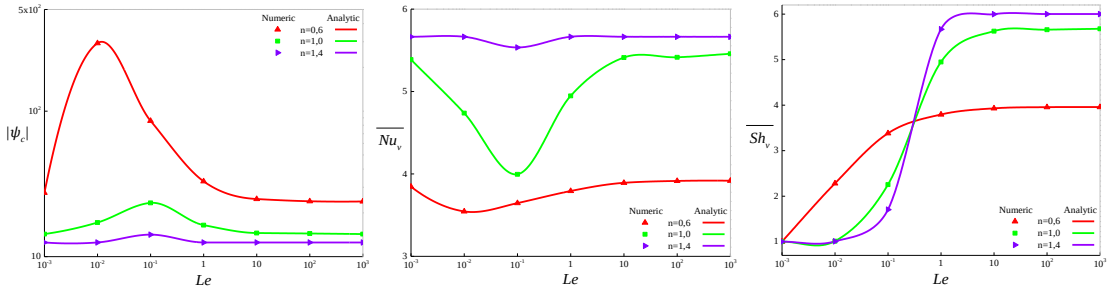

$\boldsymbol{Pe = 50}$

Figure 6.12. Variations of the stream function at the center of the cavity $(x = A/2,\ y = 1/2)$ (left), vertical Nusselt number (middle), and vertical Sherwood number (right) with Lewis number Le for $Ra_T = 10^4, N = 1$, and various values of Pe and n inside double lid-driven Rayleigh-Bénard configuration.

plateau. Further, as Pe increases the power-law index influence on $|\psi_c|$ weakens, confirming the forced convection abolishing effect on the rheological behavior influence. As for $\overline{Nu_v}$, when the shear force contribution is insignificant ($Pe = 0.1$ and 5), the evolution is similar to that of $|\psi_c|$ as the natural convection dominates the convective regime. However, as Péclet number increases and forced regime starts to influence the convective regime (mixed convection), $\overline{Nu_v}$ displays two higher plateaus for small and large values of Le while hitting a minimum value in-between which decreases and shifts left as n decreases. The effect of power law-index is also reversed compared to dominant natural convection regime, as now decreasing n reduces heat transfer confirming the previous similar conclusion. Such results can be explained while referring to Figure 6.10(c) showing the variation of y_0 with Le. Figure 6.12 shows that the value of Le for which $|\psi_c|$ and $\overline{Nu_v}$ hit extremum values between the two plateaus is the same for different n values, which corresponds in Figure 6.10(c) to a significant increase in y_0 value indicating that natural convection contribution enhances. For $|\psi_c|$, enhancing natural convection always promotes fluid circulation independent of shear force strength. As for Nusselt number, strengthening natural regime promotes heat transfer for low Pe values ($Pe = 0.1$ and 5), while after a critical Pe value the opposite happens as heat transfer reduces and the enhancing role of decreasing n is inverted, confirming what we mentioned about Pe_{cr}.

For $\overline{Sh_v}$, a lower plateau characterized by $\overline{Sh_v} \approx 1$ for small values of Lewis number, describing high mass diffusivity, indicates that mass transfer is entirely assured by diffusion. Fluids with lower power-law index are the first to leave the lower plateau given that increasing n weakens convection transport mechanism. As Le gradually increases, mass transfer increases monotonously given the well-established effect of Lewis number on enhancing convective mass transfer. For larger values of Le, mass transfer reaches a higher plateau where no further enhancement can be gained from increasing Le. As Pe rises, $\overline{Sh_v}$ reaches higher plateaus, more rapidly while increasing power-law index leading to reversing the rheological-behavior effect on enhancing convection mass transfer. Additionally, for the same value of Pe it is obvious that increasing Lewis number promotes forced regime, where for smaller values of Le the effect of n matches what we observed for dominant natural convection, while increasing Le leads to reverse such effect indicating a greater input of the forced regime.

The value of Le signaling this change decreases while increasing Pe . The same can be concluded from Figure 6.10(c), where y_0 decreases as Le rises. Finally, Figure 6.12 shows how Lewis number and shear force magnitude can be used to enhance flow intensity and heat and mass transfer rates given the non-Newtonian fluids behavior. For mass transfer case, when increasing Le doesn't produce any further enhancement, Pe enhances $\overline{Sh_v}$ only to a certain extent, where increasing it from 25 to 50 improves significantly mass transfer for $n = 1$ while the gain is negligeable for $n = 1.4$.

As for flow intensity and heat transfer, the effect of n on both characteristics reduces for smaller and larger values of Le, more noticeably as Pe increases. This can be confirmed from Figure 6.10(c), where y_0 value decreases for small and large Le, more rapidly for shear thickening fluids that reach lesser values ($y_0 = 0$) given the effect of increasing n on weakening natural convection characteristics; therefore, accelerating forced convection domination of fluid circulation and heat transfer. Altogether, the results show the effect of increasing Le on promoting forced convection contribution in the overall convective regime, while decreasing Le promotes such contribution only for fluid circulation and heat transfer as mass transfer process is entirely by diffusion.

6.8 Effect of buoyancy ratio

The effects of buoyancy ratio N on $|\psi_c|$, $\overline{Nu_v}$, and $\overline{Sh_v}$ variations are shown in Figure 6.13 for $Ra_T = 10^4$, $Le = 10$, and different values of Pe and n. For $|\psi_c|$, at first it remains constant due to dominant thermal buoyancy force and the weak contribution of solutale one. Next, the fluid circulation slowly intensifies as the mass buoyancy force input increases before fully dominating as the quantity rises exponentially. We note that as Pe increases, the effect of power-law index on $|\psi_c|$ reduces, demonstrating the influence of strengthening shear force on rheological-behavior effect. Further, as the shear force intensifies, the value of N signaling the onset of $|\psi_c|$ enhancement increases indicating that shear force magnitude delays the dominance of solutal buoyancy force which promotes the natural regime contribution in the overall convection. This competing nature manifests also as buoyancy ratio keeps increasing, where the diminishing influence of Pe on the power-law index effect on $|\psi_c|$ vanishes and the effect becomes more pronounced.

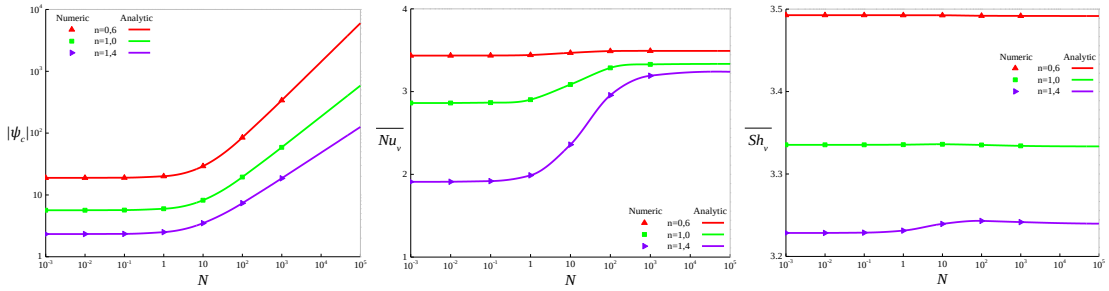

$\boldsymbol{Pe = 0.1}$

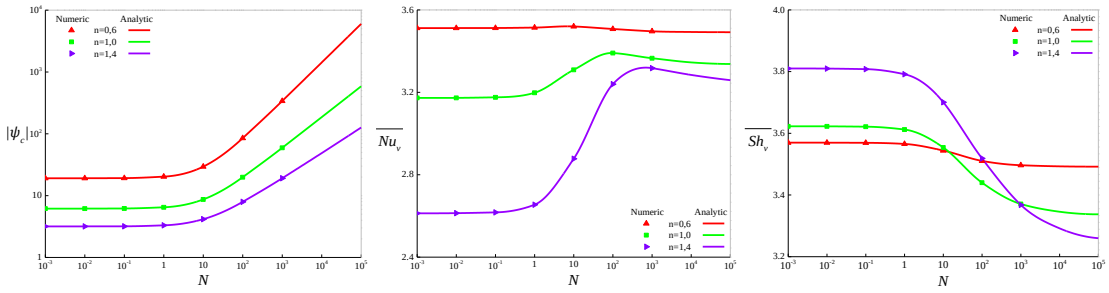

$\boldsymbol{Pe = 5}$

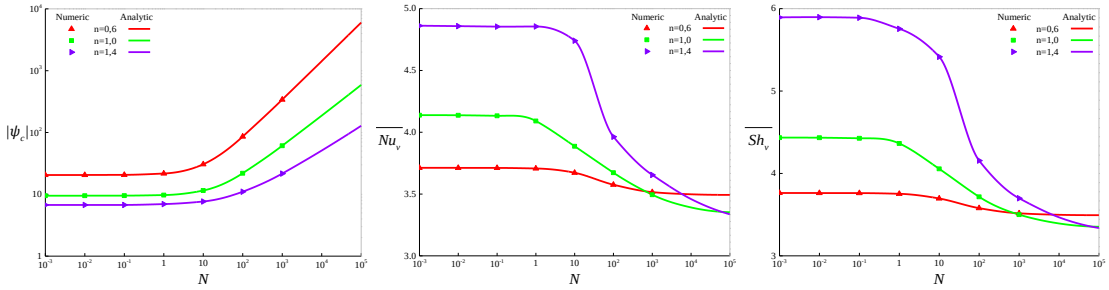

$\boldsymbol{Pe = 25}$

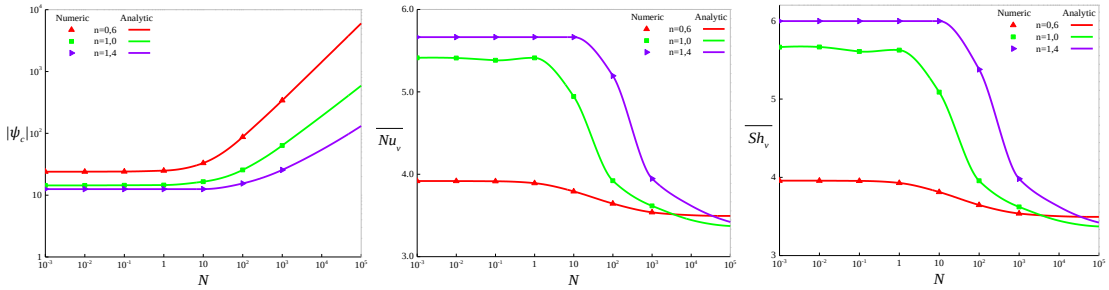

$\boldsymbol{Pe = 50}$

Figure 6.13. Variations of the stream function at the center of the cavity $(x = A/2,\ y = 1/2)$ (left), vertical Nusselt number (middle), and vertical Sherwood number (right) with buoyancy ratio N for $Ra_T = 10^4, Le = 10$, and various values of Pe and n inside double lid-driven Rayleigh-Bénard configuration.

For $\overline{Nu_v}$ and $\overline{Sh_v}$, we need to separate the cases based on the shear force strength. For $Pe = 0.1$, heat and mass transfer rates display lower and higher plateaus with an ascent in between. The lower level is characterized by a dominant thermal buoyancy force, the rise indicates the increasing contribution of solutal buoyancy force before fully dominating the transport phenomenon as we reach the upper level. Here, the moving-walls clearly do not influence the convective regime, as decreasing n intensifies heat and mass transfer as in natural convection regime. In contrast, for higher values of shear force ($Pe \geq 25$ for $\overline{Nu_v}$ and $Pe \geq 5$ for $\overline{Sh_v}$ given the influence of diffusion rate difference, $Le = 10$, on Pe_{cr} as mentioned before), the effect of n is reversed as $\overline{Nu_v}$ and $\overline{Sh_v}$ start with an upper plateau, whose extent increases with Péclet number, indicating the strong input of forced regime in the convection. As N increases, Nusselt and Sherwood numbers descend from the upper plateau as the strengthened solutal buoyancy force competes with shear force which results in reducing heat and mass transfer. Finally, for high buoyancy ratio values, the solutal buoyancy force dominates the shear effect generated by sliding walls given that the influence of power-law index begins to reverse as decreasing it enhances the transfer rates, aligning with the conclusion made from the evolution of $|\psi_c|$ where N plays a role in promoting natural convection regime. Such conclusion can be further confirmed while referring to Figure 6.10(d), where increasing N moves y_0 values far from the sliding walls and closer to the ones obtained for pure natural regime; hence, indicating the boosted role of natural regime in the overall convection.

6.9 Horizontal velocity, temperature, and concentration

The evolutions of horizontal velocity (left), temperature (middle), and concentration (right) at mid-length of the enclosure ($x = A/2$) are presented in Figure 6.14 for $Pe = 25, Le = 10, N = 1$, and several values of Ra_T and n. The profiles show a perfect agreement between analytical and numerical solutions. Furthermore, and given the symmetry of applied boundary conditions, the profiles display symmetrical negative and positive regions. The critical value of thermal Rayleigh number $Ra_{T(cr)}$ is defined in order to further highlight the effects of buoyancy force and shear force on inducing fluid flow and heat and mass transfer. For $Ra_{T(cr)}$, the velocity minimum and maximum

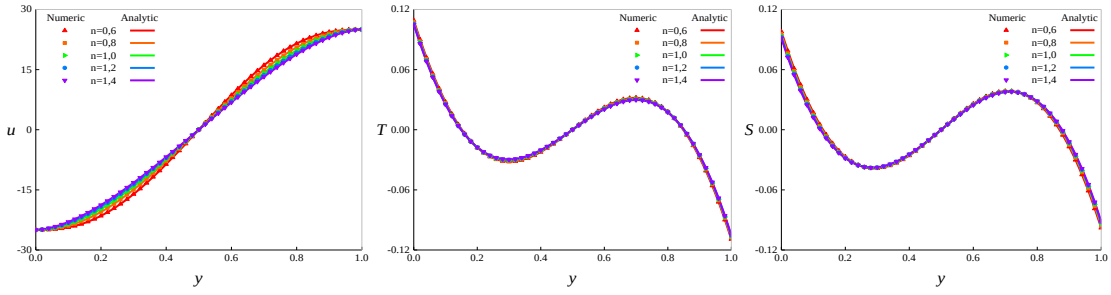

$$Ra_T = Ra_{T(cr)}$$

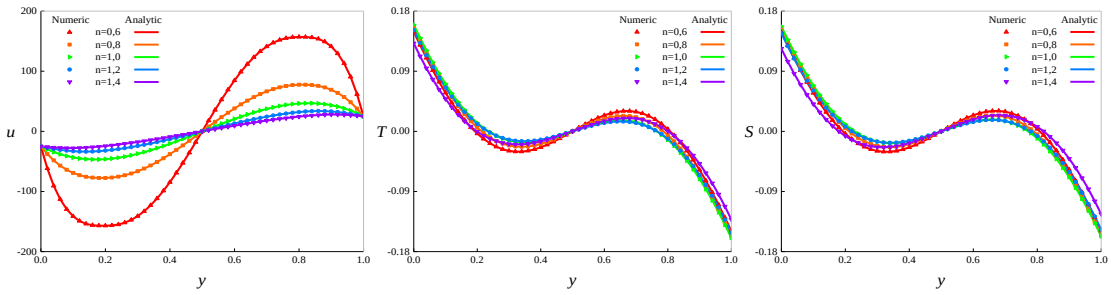

$$Ra_T = 5 \times 10^4$$

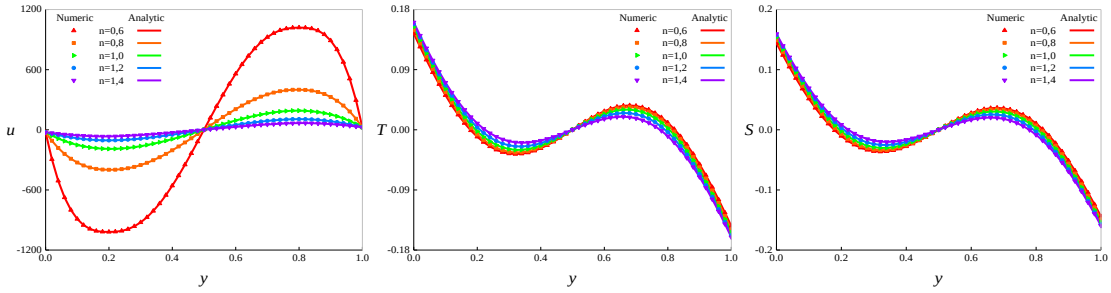

$$Ra_T = 10^6$$

Figure 6.14. Horizontal velocity u (left), temperature T (middle), and concentration S (right) profiles at mid-length of the cavity $(x = A/2)$ along the y-axis for $Pe = 25, Le = 10, N = 1$, and different characteristics values of Ra_T and n inside double lid-driven Rayleigh-Bénard configuration. $Ra_{T(cr)}$ signals the onset of buoyancy-driven flow.

overlap with the velocity of sliding horizontal walls at $y = 0$ and $y = 1$, respectively, and $u, T,$ and S profiles show no significant influence of power-law index n. These observations clearly testify of shear force leading role in overall convection and agree with what we observed previously in forced regime dominance area. Accordingly, for $Ra_T \leq Ra_{T(cr)}$, forced regime dominates natural convection. For higher values of Ra_T

$(Ra_T > Ra_{T(cr)})$, and as the buoyancy force starts to strengthen, the velocity two extremums (maximum and minimum) considerably amplify while moving away from the sliding walls, meaning that the flow is now stronger in that region. Meanwhile, the effect of n becomes more pronounced on the flow intensity as natural convection starts to dominate forced convection. The values of $Ra_{T(cr)}$ indicating the transition from shear force-based flow into buoyancy-driven flow are given in Table 6.2 for different values of n. The value to make the shift reduces as n goes down given the well-established role of decreasing power-law index on intensifying natural convection characteristics, leading to accelerate the transition towards buoyancy-driven flows.

The temperature profiles also show negative and positive regions with a warm part in the bottom of the cavity and a cooled upper region due to clockwise flow carrying coldest current to the top of the cavity after discharging the heat from the bottom region along the left vertical wall. As for the power-law index effect, which vanishes for $Ra_T = Ra_{T(cr)}$ as forced convection dominates, increasing Rayleigh number shows a decreasing temperature while increasing n, meaning that dilatant fluids enhance heat transfer compared to pseudoplastic ones, which confirms the mixed regime influence on non-Newtonian fluids rheological behavior. As Ra_T reaches higher values, it becomes clear that the effect of power-law index on temperature is now reversed as decreasing it reduces the temperature; hence, increases heat transfer confirming that natural convection regime dominates. The concentration experiences similar transport phenomenon to temperature resulting in similar profiles and conclusions.

Table 6.2 – Critical thermal Raleigh number values $Ra_{T(cr)}$ signaling buoyancy-driven flow onset for $Pe = 25, Le = 10, N = 1$, and different values of n inside double lid-driven Rayleigh-Bénard configuration.

$\boldsymbol{n}$	$\boldsymbol{Ra_{T(cr)}}$
$\mathbf{0.6}$	716.644
$\mathbf{0.8}$	1574.618
$\mathbf{1.0}$	3453.9647
$\mathbf{1.2}$	7569.0888
$\mathbf{1.4}$	16576.9055

6.10 Effect of power-law behavior index

Figures 6.9, 6.11, 6.12, 6.13, and 6.14 clearly show that the influence of non-Newtonian fluids rheological behavior on fluid flow and heat and mass transfer characteristics need to be discussed in light of the dominating convective regime. First, when natural convection dominates $\left(\frac{Ra_T}{Pe^{\gamma}} > \eta_n\right)$, although the streamlines given in Figures 6.4, 6.5, and 6.6 display no apparent difference in their global structure while varying n, as the flow is unicellular with a parallel aspect except for the end regions near the enclosure vertical walls, the flow strongly intensifies as n decreases from 1.4 to 0.6 which can be confirmed from the velocity profiles in Figure 6.14 for $Ra_T = 10^6$. In contrast, the isotherms and iso-concentrations global structures are more affected by the rheological behavior as they tend to be less inclined with regard to the vertical direction as n increases. The temperature and concentration absolute values also increase as power-law index increases (Figure 6.14 for $Ra_T = 10^6$), these observations confirm that the flow loses intensity. Nusselt and Sherwood numbers reveal similar trends for dominant natural convection as their values decrease as n increases. Accordingly, for dominant natural regime, shear thinning fluids ($0 < n < 1$) strengthens convection compared to Newtonian fluids ($n = 1$), while shear thickening fluids ($n > 1$) produce the opposite effect. Such result can be explained while referring to Eq. (3.25) where increasing power-law index n increases the apparent viscosity resulting in a fluid more resistant to motion.

Second, when buoyancy force and shear force are of comparable magnitudes and the convective regime is considered mixed, the effect of n on flow intensity is the same as in dominant natural regime, where decreasing power-law index enhances fluid circulation; however, the magnitude of the enhancement reduces as shear force contribution increases. In contrast, the effect of non-Newtonian behavior on heat and mass transfer rates reverses compared to natural regime as shear thickening behavior enhances transfer rates while shear thinning reduces them when compared to Newtonian behavior. Finally, when forced convection dominates the overall convective regime given the strong shear force $\left(\frac{Ra_T}{Pe^{\gamma}} < \eta_f\right)$, the power-law index variation ceases to influence the convection characteristics $|\psi_c|$, $\overline{Nu_v}$, and $\overline{Sh_v}$ (see Figures 6.9 and 6.11). Similar conclusion can be made from Figure 6.14 for $Ra_T = Ra_{T(cr)}$ as velocity,

temperature, and concentration profiles are nearly identical for different values of n. Thus, the shear force magnitude strongly affects the rheological behavior of non-Newtonian fluids; where in the mixed convection regime, the effect of n on convection enhancement is reversed compared to natural regime, while in dominant forced convection regime such effect totally vanishes.

6.11 Critical Péclet number

The values of critical Péclet number Pe_{cr} are given in Tables 6.3, 6.4, and 6.5 while varying Ra_T, Le, and N, respectively. The Pe_{cr} value signals the reversal in non-Newtonian fluids rheological behavior effect on heat and mass transfer rates compared to natural regime; plus, it defines the magnitude of shear force after which further strengthening buoyancy force reduces heat and mass transfer instead of enhancing them. The presented values compare the different fluid behaviors: pseudoplastic ($n = 0.6$), Newtonian ($n = 1.0$), and dilatant ($n = 1.4$) and that separately for $\overline{Nu_v}$ and $\overline{Sh_v}$, where the results confirm the effect of diffusion rate difference between temperature and concentration gradients on Pe_{cr}. Two cases need further clarification; first, in Table 6.3 and for $Ra_T = 10^2$, given the weak natural convection regime associated with low thermal Rayleigh numbers while increasing power-law index, the heat transfer rates for $n = 1.0$ and $n = 1.4$ reache the plateau associated with dominant forced regime without a reversal in the effect of n on enhancing $\overline{Nu_v}$. Second, in Table 6.4 and for $Le = 10^{-3}$, no change in the power-law index effect is observed given that mass transfer is ensured entirely by diffusion ($\overline{Sh_v} \approx 1$) as shown in Figure 6.12.

Table 6.3 – Effect of Ra_T on Pe_{cr} for $Le = 10, N = 1$, and different values of n.

		Ra_T					
		10^2	10^3	10^4	10^5	10^6	5×10^6
$\overline{Nu_v}$	$\overline{Nu_v}(1.4) > \overline{Nu_v}(1.0)$	-	26.2283	12.3531	11.8516	8.2465	11.2732
	$\overline{Nu_v}(1.4) > \overline{Nu_v}(0.6)$	15.0476	12.7804	13.1573	12.6053	14.7903	24.4173
	$\overline{Nu_v}(1.0) > \overline{Nu_v}(0.6)$	15.0476	11.1981	15.4799	13.8782	30.6503	64.2055
$\overline{Sh_v}$	$\overline{Sh_v}(1.4) > \overline{Sh_v}(1.0)$	1.0729	1.3099	1.0847	2.2876	5.3453	9.8694
	$\overline{Sh_v}(1.4) > \overline{Sh_v}(0.6)$	1.0875	1.634	1.9579	4.7396	11.9474	22.9971
	$\overline{Sh_v}(1.0) > \overline{Sh_v}(0.6)$	1.0942	1.4676	3.5034	10.0078	29.5165	63.6684

Table 6.4 – Effect of Le on Pe_{cr} for $Ra_T = 10^4, N = 1$, and different values of n.

		Le						
		$\mathbf{10^{-3}}$	$\mathbf{10^{-2}}$	$\mathbf{10^{-1}}$	**1**	**10**	$\mathbf{10^{2}}$	$\mathbf{10^{3}}$
$\overline{Nu_v}$	$\overline{Nu_v}(1.4) > \overline{Nu_v}(1.0)$	12.2465	12.49	13.133	13.1065	12.3532	12.2329	12.2206
	$\overline{Nu_v}(1.4) > \overline{Nu_v}(0.6)$	13.0625	12.3457	12.9409	13.9495	13.1573	13.0906	13.0835
	$\overline{Nu_v}(1.0) > \overline{Nu_v}(0.6)$	15.3206	11.9643	12.0972	14.8901	15.4799	15.4466	15.4415
$\overline{Sh_v}$	$\overline{Sh_v}(1.4) > \overline{Sh_v}(1.0)$	-	186.9763	248.2468	13.1065	1.0847	0.7803	0.7718
	$\overline{Sh_v}(1.4) > \overline{Sh_v}(0.6)$	-	1384.855	138.2416	13.9495	1.9579	1.6261	1.6128
	$\overline{Sh_v}(1.0) > \overline{Sh_v}(0.6)$	-	1384.855	123.4425	14.8901	3.5034	3.223	3.2067

Table 6.5 – Effect of N on Pe_{cr} for $Ra_T = 10^4, Le = 10$, and different values of n.

		N						
		$\mathbf{10^{-3}}$	$\mathbf{10^{-2}}$	$\mathbf{10^{-1}}$	**1**	**10**	$\mathbf{10^{2}}$	$\mathbf{10^{3}}$
$\overline{Nu_v}$	$\overline{Nu_v}(1.4) > \overline{Nu_v}(1.0)$	12.2194	12.2206	12.2331	12.3532	13.1327	11.8207	8.2127
	$\overline{Nu_v}(1.4) > \overline{Nu_v}(0.6)$	13.0829	13.0835	13.0906	13.1573	13.5226	12.6	14.5151
	$\overline{Nu_v}(1.0) > \overline{Nu_v}(0.6)$	15.4413	15.4415	15.4466	15.4799	14.8876	13.9076	29.5196
$\overline{Sh_v}$	$\overline{Sh_v}(1.4) > \overline{Sh_v}(1.0)$	1.0399	1.0406	1.0453	1.0847	1.3381	2.3297	5.187
	$\overline{Sh_v}(1.4) > \overline{Sh_v}(0.6)$	1.8698	1.8704	1.8793	1.9579	2.5081	4.8014	11.5685
	$\overline{Sh_v}(1.0) > \overline{Sh_v}(0.6)$	3.3436	3.3453	3.3622	3.5034	4.6168	10.0304	28.3763

6.12 Conclusions

The present chapter investigates Rayleigh–Bénard double-diffusive mixed convection inside rectangular cavities filled with non-Newtonian fluids. The sliding horizontal walls are subjected to uniform heat and mass fluxes, while the motionless vertical boundaries are considered insulated and impermeable. The investigation implements two separate approaches to solve the governing equations, a numerical solution based on the finite volume method and an analytical solution derived based on the parallel flow approximation. The results show that for an aspect ratio $A \geq 28$, the flow intensity

and heat and mass transfer rates become insensitive to aspect ratio variation. Further, providing that $Pr \geq 10$, numerical results show that flow characteristics become independent of Prandtl number. Thus, non-Newtonian Rayleigh–Bénard double-diffusive mixed convection in shallow rectangular cavities is mainly governed by: Péclet number Pe, thermal Rayleigh number Ra_T, Lewis number Le, buoyancy ratio N, and power-law behavior index n. The established solutions, numerical and analytical, agree perfectly for inclusive ranges of governing parameters validating both the numerical code, the analytical approach, and the choices made throughout the study. Furthermore, and unlike the case of applied horizontal heat and mass fluxes where finite volume and finite differences methods agree perfectly; for Rayleigh–Bénard configuration, finite difference method encounters convergence and stability issues in some cases compared to finite volume method that shows high accuracy.

The mixed convection parameter $\frac{Ra_T}{Pe^{\gamma}}$ is found to separate the dominance regions of the three convective regimes, namely natural, mixed, and forced convection. The following bounds delineates the mixed regime:

$$1.54 < \frac{Ra_T}{Pe^{1.57}} < 102.19;\ 3.46 < \frac{Ra_T}{Pe^{1.92}} < 1121.21;\ 5.80 < \frac{Ra_T}{Pe^{2.27}} < 8203.57$$

for $n = 0.6, n = 1.0$ and $n = 1.4$, respectively, for $Le = 1$ and $N = 1$, while natural and forced regimes are found to dominate outside these limits. Péclet number strengthens sliding walls' shear force leading to enhance flow intensity monotonously while heat and mass transfer enhance only until reaching a higher plateau associated with dominant forced convection regime. Thermal Rayleigh number effect on transfer rates depends on the shear force magnitude, where for a given range of Pe values heat and mass transfer enhance, while after a critical value $Pe > Pe_{cr}$, increasing Ra_T reduces transfer rates as buoyancy force and shear force compete (mixed regime). For high Ra_T values, natural regime dominates and heat and mass transfer hit a plateau where they become constant. As for Lewis number, and for a given range of its values correlated to n, the contribution of natural regime abruptly enhances leading to significantly strengthen flow intensity while the outcome on heat transfer is determined by Pe_{cr}. Outside this range, forced regime contribution augments. For mass transfer, increasing Le increases the input of forced regime, more so as n increases, causing the transfer rate to rapidly enhance until reaching a higher plateau. In contrast, increasing

buoyancy ratio N enhances natural convection input in overall convection causing fluid circulation to intensify exponentially; while the effect on heat and mass transfer depends on the shear force magnitude (Pe_{cr}).

Non-Newtonian fluids rheological behavior effect on flow characteristics produces some unforeseen results directly correlated with the dominant convective regime. First, for dominant natural regime, decreasing power-law index significantly enhances flow intensity and heat and mass transfer. Second, for mixed convection regime, the effect of n on heat and mass transfer is reversed, while the effect on flow intensity stays the same with the enhancement extent reducing as shear force strengthens. Finally, for dominant forced regime, the effect of power-law index on the three flow characteristics vanishes as shear force strongly affects fluid viscosity. The Critical Péclet number Pe_{cr} signaling the reversal in n effect on heat and mass transfer and after which further strengthening buoyancy force reduces the transfer rates is established as a function of the remaining governing parameters Ra_T, Le, N, n.

General Conclusions

The present thesis work investigates double-diffusive mixed convection within lid-driven rectangular cavities submitted to uniform heat and mass fluxes. Three configurations are considered, a single lid-driven rectangular cavity filled with Newtonian fluid and submitted to horizontal fluxes, double lid-driven rectangular cavities filled with non-Newtonian fluids and subjected to horizontal fluxes, and Rayleigh-Bénard configuration in double lid-driven rectangular cavities filled with non-Newtonian fluids. The investigation implements two separate approaches to solve the governing equations; first, numerically using the well-known finite difference method and finite volume method. Second, an analytical solution derived based on the parallel flow approximation. The effects of governing parameters: cavity aspect ratio A, Prandtl number Pr, Péclet number Pe, thermal Rayleigh number Ra_T, Lewis number Le, buoyancy ratio N, and power-law behavior index n on flow intensity and heat and mass transfer rates are illustrated and amply discussed for each configuration in terms of stream function, average Nusselt number, average Sherwood number, streamlines, isotherms, and iso-concentrations along with velocity, temperature, and concentration profiles. The key findings can be listed as follows:

- Providing that $Pr \geq 10$, numerical results show that flow characteristics become independent of Prandtl number.
- For an aspect ratio $A \geq 24$ or $A \geq 28$ (depending on the direction of heat and mass fluxes), the flow intensity and heat and mass transfer rates become insensitive to the cavity aspect ratio variation. Thus, double-diffusive mixed convection in lid-driven rectangular cavities filled with non-Newtonian fluids is mainly governed by: Péclet number Pe, thermal Rayleigh number Ra_T, Lewis number Le, buoyancy ratio N, and power-law behavior index n.
- For thermal and solutal boundary conditions of Neumann type (i.e., imposed uniform heat and mass fluxes), the flow is parallel to the horizontal boundaries in the core region of the enclosure and the isotherms and iso-concentrations show a linear stratification in the x-direction. Such observations confirm the existence of an analytical solution.

- The established solutions, numerical and analytical, agree perfectly for inclusive ranges of governing parameters validating both the numerical codes and the analytical approach.
- The mixed convection parameter $\frac{Ra_T}{Pe^{\gamma}}$, which depends strongly on the fluid power-law behavior index, is found to perfectly delineate the dominance regions of the three convective regimes, namely natural, mixed, and forced convection, and that for the three configurations considered.
- Increasing Péclet number intensifies forced regime input in overall convection as it strengthens sliding walls' shear force. Consequently, flow intensity enhances monotonously while the effect on heat and mass transfer depends on the direction of imposed fluxes. For imposed horizontal fluxes, transfer rates enhance continuously while for applied vertical fluxes (Rayleigh–Bénard configuration) they enhance only until reaching a higher plateau associated with dominant forced convection regime.
- Increasing thermal Rayleigh number augments the contribution of natural regime due to intensified buoyancy force, leading in the case of horizontal fluxes to enhance flow intensity and heat and mass transfer monotonically. However, in the case of applied vertical fluxes, the effect on transfer rates correlates to the shear force magnitude, where for a given range of Pe values, heat and mass transfer enhance, while after a critical value $Pe > Pe_{cr}$, increasing Ra_T reduces transfer rates as buoyancy force and shear force compete (mixed regime). For high Ra_T values, natural regime dominates and heat and mass transfer hit a plateau where they become constant.
- For cavities subjected to uniform heat and mass fluxes along the short vertical walls, increasing Lewis number strongly enhances mass transfer, while no effect is noticed on flow intensity and heat transfer. Furthermore, Le is found to play a role in promoting the contribution of forced regime in overall convection as it increases, especially as the power-law index increases. As for buoyancy ratio, increasing it enhances flow characteristics as a beneficial result of dominant mass buoyancy force which strengthens the natural convection contribution. While decreasing N leads to a more dominating forced regime due to small contribution of mass buoyancy force, which becomes more obvious for shear-thickening fluids.

- For cavities submitted to uniform heat and mass fluxes on the horizontal boundaries, and for a given range of Lewis number values correlated to n, the contribution of natural regime abruptly enhances leading to strongly strengthen flow intensity while the outcome on heat transfer is determined by Pe_{cr}. Outside this range, forced regime contribution augments. For mass transfer, increasing Le increases the input of forced regime, more so as n increases, causing the mass transfer rate to rapidly enhance until reaching a higher plateau. In contrast, increasing buoyancy ratio N enhances natural convection input in overall convection causing fluid circulation to intensify exponentially; while the effect on heat and mass transfer depends on the shear force magnitude (Pe_{cr}).
- Non-Newtonian fluids rheological behavior effect on flow characteristics leads to some unforeseen results directly correlated with the dominant convective regime. First, for dominant natural regime, decreasing power-law index significantly enhances flow intensity and heat and mass transfer. Second, for mixed convection regime, the effect differs depending on the direction of imposed fluxes. For horizontal fluxes, the effects of power-law behavior index on flow intensity and transfer rates diminish as Péclet number increases. While for vertical fluxes, the effect of n on heat and mass transfer is reversed compared to dominant natural regime, while the effect on flow intensity stays the same with the enhancement extent reducing as shear force strengthens. Finally, for dominant forced regime, the effect of power-law index on the three flow characteristics vanishes as shear force strongly affects fluid viscosity.
- In the case of the Rayleigh–Bénard configuration, the Critical Péclet number Pe_{cr} signaling the reversal in n effect on heat and mass transfer and after which further strengthening buoyancy force reduces the transfer rates is established as a function of the remaining governing parameters Ra_T, Le, N, n.

It is worth mentioning that the choice of governing parameters' ranges is made in order to serve the aim of the paper to provide useful insights into the complex non-Newtonian double-diffusive mixed convection flows for both scientific field and engineering applications. However, and despite the originality of the obtained results, this work remains academic in the absence of experimental results to confirm the conclusions of this study. It would therefore be beneficial to conduct experiments with non-Newtonian

fluids, whose rheological behavior can be represented by Ostwald-de Waele rheological model, and to compare the results with the ones obtained numerically and analytically.

In perspective, an investigation of double-diffusive mixed convection inside double lid-driven rectangular cavities filled with non-Newtonian fluids and subjected simultaneously to horizontal and vertical heat and mass fluxes will be conducted. The goal is to explore the effects of governing parameters and dominant convective regimes (natural, mixed, and forced) on fluid flow and heat and mass transfer in such configuration. Furthermore, the ongoing study of opposing flow double-diffusive mixed convection will be expanded to account for the rheological behavior of non-Newtonian fluids.

References

1. Nishimura T, Imoto T, Miyashita H. Occurrence and Development of Double-Diffusive Convection During Solidification of a Binary System. Int J Heat Mass Transfer 1994; 37:1455–64. doi:10.1016/0017-9310(94)90147-3
2. Ghenai C, Mudunuri A, Lin CX, Ebadian MA. Double-diffusive convection during solidification of a metal analog system (NH4Cl-H2O) in a differentially heated cavity. Exp Therm Fluid Sci 2003; 28:23–35. doi:10.1016/S0894-1777(03)00089-X
3. Ostrach S. Fluid Mechanics of Crystal Growth. The 1982 Freeman Scholar Lecture. ASME Journal of Fluids Engineering 1983; 105:5-20. doi:10.1115/1.3240942
4. Singh NB et al. Double diffusive convection during growth of lead Bromide crystals. Adv. Space Res. 1993; 13 (7):195-201. doi:10.1016/0273-1177(93)90372-I
5. Zhou H, Zebib A. Oscillatory double diffusive convection in crystal growth. Journal of Crystal Growth 1994; 135:587—593. doi:10.1016/0022-0248(94)90151-1
6. Rghif Y, Zeghmati B, Bahraoui F. Soret and Dufour effects on thermosolutal convection developed in a salt gradient solar pond. International Journal of Thermal Sciences 2021; 161. doi:10.1016/j.ijthermalsci.2020.106760
7. Saleem KB, Koufi L, Alshara AK, Kolsi L. Double-diffusive natural convection in a solar distiller with external fluid stream cooling. International Journal of Mechanical Sciences 2020; 181. doi:10.1016/j.ijmecsci.2020.105728
8. Serrano-Arellano J, Xamán J, Álvarez G. Optimum ventilation based on the ventilation effectiveness for temperature and CO_2 distribution in ventilated cavities. International Journal of Heat and Mass Transfer 2013; 62:9–21. doi:10.1016/j.ijheatmasstransfer.2013.02.051
9. Zhu Y, Wang P, Sun D, Qu Z, Yu B. Multiphase porous media model with thermo-hydro and mechanical bidirectional coupling for food convective drying. International Journal of Heat and Mass Transfer 2021; 175. doi:10.1016/j.ijheatmasstransfer.2021.121356

10. Zhou SQ, Lu YZ, Song XL, Fer I. New layer thickness parameterization of diffusive convection in the ocean. Dynamics of Atmospheres and Oceans 2016; 73:87–97. doi:10.1016/j.dynatmoce.2016.01.001
11. Schmid M, Lorke A, Dinkel C, Tanyilekeb G, Wuest A. Double-diffusive convection in Lake Nyos, Cameroon. Deep-Sea Research I 2004; 51:1097–1111. doi:10.1016/j.dsr.2004.02.010
12. Islam AW, Lashgari HR, Sephernoori K. Double diffusive natural convection of CO_2 in a brine saturated geothermal reservoir: Study of non-modal growth of perturbations and heterogeneity effects. Geothermics 2014; 51:325–336. doi:10.1016/j.geothermics.2014.03.001
13. Ostrach S. Natural Convection with Combined Driving Forces. PhysicoChem. Hydrodynam. 1980; 1:233–247.
14. Abbasian AAA, Kakoli E, Hajialigol N. Double-diffusive natural convection of Al_2O_3-water nanofluid in an enclosure with partially active side walls using variable properties Journal of Mechanical Science and Technology 2014; 28(11):4681–4691. doi:10.1007/s12206-014-1035-0
15. Aly AM, Raizah ZAS. Double-diffusive natural convection in an enclosure filled with nanofluid using ISPH method, Alexandria Eng. J 2016. doi:10.1016/j.aej.2016.06.036
16. Ranganathan P, Viskanta R. Natural Convection in a Square Cavity Due to Combined Driving Forces. Numer. Heat Transfer 1988; 14:35–59. doi:10.1080/10407788808913632
17. Trevisan OV, Bejan A. Combined Heat and Mass Transfer by Natural Convection in a Vertical Enclosure. J. Heat Transfer 1987; 109:104–112. doi:10.1115/1.3248027
18. Esfahani JA, Bordbar V. Double Diffusive Natural Convection Heat Transfer Enhancement in a Square Enclosure Using Nanofluids. Journal of Nanotechnology in Engineering and Medicine 2 2011. doi:10.1115/1.4003794
19. Hussain S, Oztop HF, Jamal M, Hamdeh NA. Double diffusive nanofluid flow in a duct with cavity heated from below, International Journal of Mechanical Sciences 2017. doi:10.1016/j.ijmecsci.2017.07.057

20. Darbhasayanam S, Barman D. The variable gravity field and viscous dissipation effects on the double diffusive and Soret driven convective instability in a porous layer with throughflow. International Communications in Heat and Mass Transfer 2020. doi:10.1016/j.icheatmasstransfer.2020.105050
21. Liang X, Peng B, Tian ZF. Complex transition of double-diffusive convection in a rectangular enclosure with height-to-length ratio equal to 4: Part II. International Journal of Heat and Mass Transfer 2019; 135:247–261. doi:10.1016/j.ijheatmasstransfer.2019.01.116
22. Hu JT, Mei SJ, Liu D, Zhao FY, Wang HQ. Hydromagnetic double diffusive moisture convection from an inclined enclosure inserted with multiple heat-generating electronic modules. International Journal of Thermal Sciences 2021; 159:106554. doi:10.1016/j.ijthermalsci.2020.106554
23. Zhang L, Li YR, Zhang H. Onset of double-diffusive Rayleigh-Bénard convection of a moderate Prandtl number binary mixture in cylindrical enclosures. International Journal of Heat and Mass Transfer 2017; 107:500–509. doi:10.1016/j.ijheatmasstransfer.2016.11.054
24. Rana GC, Chand R. On the Onset of Double-diffusive Convection in a Couple Stress Nanofluid in a Porous Medium. Periodica Polytechnica Mechanical Engineering 2018.
25. Li YR, Zhang H, Zhang L, Wu CM. Three-dimensional numerical simulation of double-diffusive Rayleigh–Bénard convection in a cylindrical enclosure of aspect ratio 2. International Journal of Heat and Mass Transfer 2016; 98:472–483. doi:10.1016/j.ijheatmasstransfer.2016.03.026
26. Malashetty MS, Kollur P, Sidram W. Effect of rotation on the onset of double diffusive convection in a Darcy porous medium saturated with a couple stress fluid. Applied Mathematical Modelling 2013; 37:172–186. doi:10.1016/j.apm.2012.02.024
27. Krishnan S, Aravamudan K. Simulation of non-Newtonian fluid-food particle heat transfer in the holding tube used in aseptic processing operations. In: food and bioproducts processing, 91; 2013; 129–48. doi:10.1016/j.fbp.2012.08.008
28. Khani F, Darvishi MT, Gorla RSR. Analytical investigation for cooling turbine disks with a non-Newtonian viscoelastic fluid. Comput Mathematics with Appl 2011; 61:1728–38. doi:10.1016/j.camwa.2011.01.040

29. Sriram K, Intaglietta M, Tartakovsky DM. Non-Newtonian Flow of Blood in Arterioles: Consequences for Wall Shear Stress Measurements. Microcirculation 2014. doi:10.1111/micc.12141
30. Foong LK, Shirani N, Toghraie D, Zarringhalam M, Afrand M. Numerical simulation of blood flow inside an artery under applying constant heat flux using Newtonian and non-Newtonian approaches for biomedical engineering. Comput Methods Programs Biomed 2020; 190:105375. doi:10.1016/j.cmpb.2020.105375
31. Akçay M, Yükselen M. Drag reduction of a nonnewtonian fluid by fluid injection on a moving wall. Arch Appl Mechanics 1999; 69:215–25. doi:10.1007/s004190050215
32. Kuhlmann HC, Romanò F. The Lid-Driven Cavity. In: Gelfgat, A. (eds) Computational Modelling of Bifurcations and Instabilities in Fluid Dynamics. Computational Methods in Applied Sciences 2019; 50:233–309. doi:10.1007/978-3-319-91494-7_8
33. Zienkiewicz OC, Taylor RL, Nithiarasu P. Chapter 4 - Incompressible Newtonian Laminar Flows, The finite element method for fluid dynamics. Elsevier 2014 7th edition: 127–161. Elsevier (2006). doi:10.1016/B978-1-85617-635-4.00004-2
34. Saha S, Hasan MN, Khan IA. Double diffusive mixed convection heat transfer inside a vente square cavity. Chemical Engineering Research Bulletin 2009; 13:17–24. doi:10.3329/cerb.v13i1.2512
35. Garoosi F, Rohani B, Rashidi MM. Two-phase mixture modeling of mixed convection of nanofluids in a square cavity with internal and external heating. Powder Technology 2015; 275:304–321. doi:10.1016/j.powtec.2015.02.015
36. Waheed MA. Mixed convective heat transfer in rectangular enclosures driven by a continuously moving horizontal plate. Int J Heat Mass Transfer 2009; 52:5055–63. doi:10.1016/j.ijheatmasstransfer.2009.05.011
37. Iwatsu R, Hyun JM, Kuwahara K. Mixed convection in a driven cavity with a stable vertical temperature gradient. Int J Heat Mass Transfer 1993; 36:1601–8. doi:10.1016/S0017-9310(05)80069-9

38. Khanafer K, Chamkha AJ. Mixed convection flow in a lid-driven enclosure filled with a fluid-saturated porous medium. Int J Heat Mass Transfer 1999; 42:2465–81. doi:10.1016/S0017-9310(98)00227-0
39. Sharif MAR. Laminar mixed convection in shallow inclined driven cavities with hot moving lid on top and cooled from bottom. Appl Therm Eng 2007; 27:1036–42. doi:10.1016/j.applthermaleng.2006.07.035
40. Tiwari RK, Das MK. Heat transfer augmentation in a two-sided lid-driven differentially heated square cavity utilizing nanofluids. Int J Heat Mass Transfer 2007; 50:2002–18. doi:10.1016/j.ijheatmasstransfer.2006.09.034
41. Abdelkhalek MM. Mixed convection in a square cavity by a perturbation technique. Comput Mater Sci. 2008; 42:212–9. doi:10.1016/j.commatsci.2007.07.004
42. Khanafer KM, Al-Amiri AM, Pop I. Numerical simulation of unsteady mixed convection in a driven cavity, using an externally excited sliding lid. Eur J Mech B: Fluids 2007; 26:669–87. doi:10.1016/j.euromechflu.2006.06.006
43. Munshi MJH, Alim MA, Ali M, Alam MS. A Numerical Study of Mixed Convection in Square Lid-Driven with Internal Elliptic Body and Constant Flux Heat Source on the Bottom Wall. J. Sci. Res. 2017; 9(2):145–158. doi:10.3329/jsr.v9i2.29644
44. Aydm O. Aiding and opposing mechanisms of mixed convection in a shear- and buoyancy-driven cavity. Int. Comm. Heat Mass Transfer 1999; 26(7):1019–1028. doi:10.1016/S0735-1933(99)00091-3
45. Lamarti H, Mahdaoui M, Bennacer R, Chahboun A. Numerical simulation of mixed convection heat transfer of fluid in a cavity driven by an oscillating lid using lattice Boltzmann method. International Journal of Heat and Mass Transfer 2019; 137:615–629. doi:10.1016/j.ijheatmasstransfer.2019.03.057
46. Cheng TS. Characteristics of mixed convection heat transfer in a lid-driven square cavity with various Richardson and Prandtl numbers. International Journal of Thermal Sciences 2011; 50:197–205. doi:10.1016/j.ijthermalsci.2010.09.012
47. Gangawane KM, Manikandan B. Mixed convection characteristics in lid-driven cavity containing heated triangular block. Chinese Journal of Chemical Engineering 2017. doi:10.1016/j.cjche.2017.03.009

48. Oztop HF, Al-Salem K, Pop I. MHD mixed convection in a lid-driven cavity with corner heater. International Journal of Heat and Mass Transfer 2011; 54:3494–3504. doi:10.1016/j.ijheatmasstransfer.2011.03.036
49. Nosonov II, Sheremet MA. Conjugate mixed convection in a rectangular cavity with a local heater. International Journal of Mechanical Sciences 2018; 136:243–251. doi:10.1016/j.ijmecsci.2017.12.049
50. Bozorg MV, Siavashi M. Two-phase mixed convection heat transfer and entropy generation analysis of a non-Newtonian nanofluid inside a cavity with internal rotating heater and cooler. International Journal of Mechanical Sciences 2019; 151:842–857. doi:10.1016/j.ijmecsci.2018.12.036
51. Gangawane KM, Oztop HF. Mixed convection in the semi-circular lid-driven cavity with heated curved wall subjugated to constant heat flux for non-Newtonian power-law fluids. International Communications in Heat and Mass Transfer 2020; 114:104563. doi:10.1016/j.icheatmasstransfer.2020.104563
52. Siddiqui MA, Riaz A, Khan I, Nisar KS. Augmentation of mixed convection heat transfer in a lid-assisted square enclosure utilizing micropolar fluid under magnetic environment: A numerical approach. Results in Physics 2020; 18:103245. doi:10.1016/j.rinp.2020.103245
53. Zhou W, Yan Y, Liu X, Chen H, Liu B. Lattice Boltzmann simulation of mixed convection of nanofluid with different heat sources in a double lid-driven cavity. International Communications in Heat and Mass Transfer 2018; 97:39–46. doi:10.1016/j.icheatmasstransfer.2018.07.008
54. Gangawane KM, Gupta S. Mixed convection characteristics in rectangular enclosure containing heated elliptical block: Effect of direction of moving wall. International Journal of Thermal Sciences 2018; 100–115. doi:10.1016/j.ijthermalsci.2018.04.010
55. Mukherjee S, Biswal P, Chakraborty S, DasGupta S. Effects of viscous dissipation during forced convection of power-law fluids in microchannels. International Communications in Heat and Mass Transfer 2017; 89:83–90. doi:10.1016/j.icheatmasstransfer.2017.09.018

56. Manchanda M, Gangawane KM. Mixed convection in a two- sided lid-driven cavity containing heated triangular block for non-Newtonian power-law fluids. International Journal of Mechanical Sciences 2018. doi:10.1016/j.ijmecsci.2018.06.005
57. Arani AAA, Ababaei A, Sheikhzadeh GA, Aghaei A. Numerical simulation of double-diffusive mixed convection in an enclosure filled with nanofluid using Bejan's heatlines and masslines. Alexandria Eng J 2017. doi:10.1016/j.aej.2017.03.034.
58. Nithyadevi N, Rajarathinam M. Non-Darcy double diffusive mixed convection for nanofluid with Soret and Dufour effects in a lid-driven cavity. Int J Nanoparticles 2015; 8(3/4):218–40. doi:10.1504/IJNP.2015.073724
59. Nath R, Krishnan M. Numerical study of double diffusive mixed convection in a backward facing step channel filled with Cu-water nanofluid. Int J Mech Sci 2019; 153–154:48–63. doi:10.1016/j.ijmecsci.2019.01.035
60. Sivasankaran S, Ananthan SS, Bhuvaneswari M, Abdul Hakeem AK. Double diffusive mixed convection in a lid-driven cavity with non- uniform heating on sidewalls. Sādhanā 2017; 42:1929–41. doi:10.1007/s12046-017-0735-4
61. Sheremet MA, Pop I. Mixed convection in a lid driven square cavity filled by a nanofluid: Buongiorno's mathematical model. Appl Math Comput 2015; 266:792– 808. doi:10.1016/j.amc.2015.05.145
62. Ababaei A, Abbaszadeh M, Arefmanesh A, Chamkha AJ. Numerical simulation of double-diffusive mixed convection and entropy generation in a lid-driven trapezoidal enclosure with a heat source. Numerical Heat Transfer, Part A: Applications 2018; 702–20. doi:10.1080/10407782.2018.1459139
63. Al-Amiri AM, Khanafer KM, Pop I. Numerical simulation of combined thermal and mass transport in a square lid-driven cavity. Int J Therm Sci 2007; 46:662–71. doi:10.1016/j.ijthermalsci.2006.10.003
64. Senthil Kumar D, Murugesan K, Thomas HR. Numerical Simulation of Double Diffusive Mixed Convection in a Lid-Driven Square Cavity Using Velocity-Vorticity Formulation. Numerical Heat Transfer, Part A: Applications: An Int J Comput Methodol 2008; 54(9):837–65. doi:10.1080/10407780802424213

65. Hussain S, Mehmood K, Sagheer M, Yamin M. Numerical simulation of double diffusive mixed convective nanofluid flow and entropy generation in a square porous enclosure. Int J Heat Mass Transfer 2018; 122:1283–97. doi:10.1016/j.ijheatmasstransfer.2018.02.082
66. Yapicia K, Karasozenb B, Uludag Y. Finite volume simulation of viscoelastic laminar flow in a lid-driven cavity. J. Non-Newton. Fluid Mech. 2009; 164:51–65. doi:10.1016/j.jnnfm.2009.08.004
67. Kefayati GHR. Mesoscopic simulation of magnetic field effect on double-diffusive mixed convection of shear-thinning fluids in a two-sided lid-driven cavity. J Mol Liq 2014. doi:10.1016/j.molliq.2014.07.024
68. Hajesfandiari A, Dargush GF, Hadjesfandiari AR. Size-dependent fluid dynamics with application to lid-driven cavity flow. J Non-Newton Fluid Mech 2015; 223:98–115. doi:10.1016/j.jnnfm.2015.05.008
69. Kefayati GHR. Mesoscopic simulation of double-diffusive mixed convection of Pseudoplastic Fluids in an enclosure with sinusoidal boundary conditions. Comput Fluids 2014; 97:94–109. doi:10.1016/j.compfluid.2014.04.007
70. Nayak AK, Haque A, Banerjee A. Thermosolutal mixed convection of a shear thinning fluid due to partially active mixed zones within a lid-driven cavity. Int J Heat Mass Transfer 2017; 106:686–707. doi:10.1016/j.ijheatmasstransfer.2016.09.057
71. Kefayati GHR. Double-diffusive mixed convection of pseudoplastic fluids in a two sided lid-driven cavity using FDLBM. J Taiwan Inst Chem Eng 2014; 45(5):2122–39. doi:10.1016/j.jtice.2014.05.026
72. El Alami M, Najam M, Semma EA, Oubarra A, Penot F. Electronic components cooling by natural convection in horizontal channel with slots. Energy conversion and Management 2005; 46:2762–72. doi:10.1016/j.enconman.2005.01.005
73. Herman C, Kang E. Experimental visualization of temperature fields and study of heat transfer enhancement in oscillatory flow in a grooved channel. Heat and Mass Transfer 2001; 37(1):87–99. doi:10.1007/s002310000101
74. Bettaibi S et al. Hybrid LBM-MRT model coupled with finite difference method for double-diffusive mixed convection in rectangular enclosure with insulated moving lid. Physica 2015. doi:10.1016/j.physa.2015.10.029

75. Teamah MA, El-Maghlany WM. Numerical simulation of double-diffusive mixed convective flow in rectangular enclosure with insulated moving lid. Int J Therm Sci 2010; 49:1625–38. doi:10.1016/j.ijthermalsci.2010.04.023
76. Gurtin, ME. An Introduction to Continuum Mechanics. Academic Press, San Diego, 1981.
77. Ostwald W. Ueber die Geschwindigkeitsfunktion der Viskosität disperser Systeme. I. Kolloid-Zeitschrift 1925; 36:99–117. doi:10.1007/BF01431449
78. de Waele A, Viscometry and plastometry. J. Oil Color Chem. Assoc. 1923; 6:33–88.
79. Thangamani V, Kok FN. Energy harvesting from cavity flow oscillations. Journal of Intelligent Material Systems and Structures. 2022; 33(3):400–418. doi:10.1177/1045389X211014949
80. Tadmor Z, Gogos G. Principles of Polymer Processing, 2nd ed.; John Wiley & Sons: Hoboken, NJ, USA, 2006.
81. Squires TM, Quake SR. Microfluidics: Fluid physics at the nanoliter scale. Rev. Mod. Phys. 2005; 77:977–1026.
82. Fodor PS, Itomlenskis M, Kaufman M. Assessment of mixing in passive microchannels with fractal surface patterning. European Phys. J.: Appl. Phys. 2009; 47:31301.
83. Lienhard IV JH, Lienhard V JH. A Heat Transfer Textbook: Fifth Edition. Cambridge, MA: Phlogiston Press 2020.
84. Gray DD, Giorgini A. The validity of the Boussinesq approximation for liquids and gases. Int J Heat Mass Transfer 1976; 19:545–51. doi:10.1016/0017-9310(76)90168-X
85. Siginer DA, Valenzuela-Rendon A. On the laminar free convection and instability of grade fluids in enclosures. Int J Heat Mass Transfer 2000; 43: 3391–405. doi:10.1016/S0017-9310(99)00357-9
86. Lamsaadi M, Naimi M, Hasnaoui M. Natural convection heat transfer in shallow horizontal rectangular enclosures uniformly heated from the side and filled with non-Newtonian power law fluids. Energy Convers. Manage. 2006; 47:2535–2551. doi:10.1016/j.enconman.2005.10.028

87. Kaddiri M. Etude numérique des écoulements et des transferts de chaleur par convection naturelle dans les fluides non-Newtoniens thermo-dépendants confinés. PhD thesis, University Sultan Moulay Slimane, Beni Mellal, 2013.
88. Woods L. A Note on the Numerical Solution of Fourth Order Differential Equations. Aeronautical Quarterly 1954; 5(4): 176-184. doi:10.1017/S0001925900001177
89. Patankar SV. Numerical Heat Transfer and Fluid Flow. Hemisphere Publishing Corporation, Washington, DC, 1980.
90. Patankar SV, Spalding DB. A calculation procedure for heat mass and momentum transfer in three dimensional parabolic flows. Int. J. Heat Mass Transfer 1972; 15:1787.
91. Bejan A. The boundary layer regime in a porous layer with uniform heat flux from the side. Int. J. Heat Mass Transfer 1983; 26:1339–46. doi:10.1016/S0017-9310(83)80065-9
92. Ozoe H, Churchill SW. Hydrodynamic Stability and Natural Convection in Ostwald-de Waele and Ellis Fluids: The Development of a Numerical Solution. AlChE Journal 1972; 18(6). doi:10.1002/aic.690180617
93. Naimi M, Hasnaoui M, Platten JK. Marangoni convection of non-Newtonian power law fluids in a shallow rectangular cavity. Engineering Computations 2000; 17(6):638–668. doi:10.1108/02644400010340570
94. Lamsaadi M, Naimi M, Hasnaoui M. Natural convection heat transfer in shallow horizontal rectangular enclosures uniformly heated from the side and filled with non-Newtonian power law fluids. Energy Convers Manage 2006; 47:2535–51. doi:10.1016/j.enconman.2005.10.028
95. Mamou M, Vasseur P, Bilgen E. Analytical and numerical study of double diffusive convection in a vertical enclosure. Heat Mass Transfer 1996; 32:115–25. doi:10.1007/s002310050100
96. Khezzar L, Siginer D, Vinogradov I. Natural convection of power law fluids in inclined cavities. Int J Therm Sci 2012; 53:8–17. doi:10.1016/j.ijthermalsci.2011.10.020
97. Kim GB, Hyun JM, Kwak HS. Transient buoyant convection of a power-law non-Newtonian fluid in an enclosure. Int J Heat Mass Transf 2003; 46:3605–17. doi:10.1016/S0017-9310(03)00149-2